On explicit exponential integrators in the solution of elastic wave propagation equations

Sobre integradores exponenciais explícitos na solução das equações elásticas de propagação das ondas

Fernando Valdés Ravelo

Thesis presented to the
Institute of Mathematics and Statistics
of the University of São Paulo
in partial fulfillment
of the requirements
for the degree of
Doctor of Science

Program: Applied Mathematics
Advisor: Prof. Dr. Pedro da Silva Peixoto
Coadvisor: Prof. Dr. Martin Schreiber

Esta pesquisa recebeu financiamento do R&D registrado como ANP20714-2 STMI - Software Technologies for Modelling and Inversion, com aplicações em imageamento sísmico (USP/Shell Brasil/ANP) · Coordenação de Aperfeiçoamento de Pessoal de Nível Superior - Brasil (CAPES) - Código de Financiamento 001 · Conselho Nacional de Desenvolvimento Científico e Tecnológico (CNPq) - Brasil.

São Paulo
November, 2023

On explicit exponential integrators in the solution of elastic wave propagation equations

Sobre integradores exponenciais explícitos na solução das equações elásticas de propagação das ondas

Fernando Valdés Ravelo

This is the original version of
the thesis prepared by candidate
Fernando Valdés Ravelo, as submitted
to the Examining Committee.

Para Santi, por ser,
para mamá y papá, por amar,
para o meu mozão, porque sim.

Agradecimentos

A veces, al final, la meta es diferente de lo que pensábamos.
Lo importante es, al llegar, reconocer que era lo que queríamos.

— Pensamientos propios

Quero começar agradecendo ao meu orientador, Pedro. Ele não é só um ótimo pesquisador, mas também um tremendo professor. Não importa o monte de projetos em que ele estava envolvido, sempre tinha tempo para mim cada vez que eu precisava. Seus comentários e sugestões ajudaram muito na conformação da Tese (assim que, se não ficou boa, a culpa é dele). Também é uma ótima pessoa, e sua preocupação pelos orientandos vai até além do término da relação aluno-professor pela instituição (quer dizer, não nos deixa viver em paz). Por isso, Pedro, para você que está lendo minha Tese por última vez (espero), boa sorte se livrando de mim. Mas falando sério (embora o anterior também era), foi um prazer ser seu orientando.

Also, I must thank Martin, my co-advisor. Just like Pedro, he conducted extremely quick reviews of my writings, and his suggestions were unerringly accurate. I owe to him the improvement I made during my Ph.D. in organizing ideas in scientific writing.

Quiero agradecer también a mis amigos, que no solo están presentes para compartir la vida y ayudar en lo que pueden. Como también esta es la única página de la Tesis que les interesa y por eso devo mencionarlos. A Alia, Javier, Jose, Ernesto, Marco, y otros muchos más que amo, pero que no recibirán cópia de la Tesis.

Por último, e igual de importante que los otros, estoy feliz, y no agradezco porque no preciso, de tener a mi familia. A mi hermano Santi, mi mejor amigo, que quiero en cantidades transfinitas. A mamá y papá, por su amor y apoyo incondicional, que perdonan qualquier cosa y lo aman todo. Agradezco a mi abuela, que vino desde Goiânia solo para ver mi defensa. Também, fico por ter Igor, que tem me dado muitas razões para estar feliz.

Também preciso agradecer às agências que financiaram este projeto e meus estudos de doutorado. Durante o desenvolvimento deste trabalho, recebi auxílio financeiro da associação com o projeto em andamento de R&D registrado como ANP20714-2 STMI - Software Technologies for Modelling and Inversion, com aplicações em imageamento sísmico (USP/Shell Brasil/ANP). Tive financiamento em parte pela Coordenação de Aperfeiçoamento de Pessoal de Nível Superior - Brasil (CAPES) - Código de Financiamento 001. Também recebi financiamento pelo Conselho Nacional de Desenvolvimento Científico e Tecnológico (CNPq) - Brasil.

Resumo

Fernando Valdés Ravelo. **Sobre integradores exponenciais explícitos na solução das equações elásticas de propagação das ondas**. Tese (Doutorado). Instituto de Matemática e Estatística, Universidade de São Paulo, São Paulo, 2023.

Os integradores exponenciais, uma classe de métodos numéricos usados para solucionar equações diferenciais, são o objeto de estudo deste trabalho. Especificamente, concentramo-nos em integradores exponenciais explícitos usados para resolver as equações diferenciais que descrevem a propagação de ondas acústicas e elásticas, com condições de fronteira absorvente, encontradas em aplicações de imageamento sísmico. Dentre os vários métodos de integradores exponenciais, analisamos detalhadamente o método baseado em polinômios de Faber, uma generalização do conhecido integrador exponencial que utiliza polinômios de Chebyshev. A partir do estado da arte da aproximação de polinômios de Faber, discutimos as principais limitações do método e propomos soluções para elas.

Entre os resultados teóricos da aproximação de Faber, apresentamos uma estimativa mais precisa, em comparação com a literatura existente, do erro de aproximação do método para matrizes normais. Destacamos a importância de estimativas precisas do espectro do operador para garantir uma convergência rápida do método. Também, fundamentado por vários experimentos numéricos, delineamos um esquema para obter as estimativas dos autovalores usando apenas operadores de baixa dimensão.

Entre os resultados numéricos, observamos que ao aumentar o grau dos polinômios de Faber, o tamanho máximo do passo de tempo na integração temporal também aumenta. Além disso, ao analisar a eficiência computacional, constatamos que o uso de graus mais altos de polinômios de Faber reduz a quantidade de operações matriz-por-vetor realizadas. A robustez de nossos resultados numéricos é assegurada por meio da implementação de vários testes com diferentes níveis de complexidade.

Também, realizamos comparações entre o método dos polinômios de Faber e outros integradores exponenciais explícitos, como o método dos subespaços de Krylov e os Runge-Kuttas de alta ordem, junto com métodos clássicos de baixa ordem. As comparações foram feitas em cenários experimentais que simulam situações reais encontradas em aplicações de imageamento sísmico. Logo, avaliamos a estabilidade, dispersão, convergência numérica e eficiência computacional desses métodos. Em nossa análise, dentre os integradores exponenciais de alta ordem, o método baseado nos subespaços de Krylov apresentou os melhores resultados de convergência em comparação com todos os métodos de integração exponencial. Permitindo passos de tempo mais longos para um mesmo grau de aproximação em relação aos demais métodos. Notoriamente, ao compararmos os métodos quanto à eficiência computacional, observamos que os métodos numéricos de alta ordem conseguem atingir uma eficiência comparável aos métodos de baixa ordem, ao mesmo tempo em que permitem passos de tempo significativamente maiores.

Com o intuito de destacar outras aplicações que demandam a eficiente solução da equação da onda, apresentamos uma nova aplicação na área de modelagem matemática para o tratamento do câncer. Como uma proposta inovadora, desenvolvemos um modelo fundamentado na mecânica de meios contínuos para simular o efeito da Terapia Mecânica de Ondas de Choque de Alta Intensidade (TMOC) no crescimento de um tumor avascular. Neste modelo, demonstramos que, ao ajustar diferentes parâmetros da TMOC, conseguimos reproduzir qualitativamente diversos padrões de crescimento do tumor, conforme relatado na literatura.

Adicionalmente, realizamos uma análise de sensibilidade do modelo em relação aos vários parâmetros da terapia, identificando os elementos mais influentes no crescimento do tumor.

Palavras-chave: Integradores exponencias. Equação da onda. Polinômios de Faber. Elasticidade linear. Modelação matemática. Mecânica do contínuo. Câncer. Ondas de Choque de Alta Intensidade.

Abstract

Fernando Valdés Ravelo. **On explicit exponential integrators in the solution of elastic wave propagation equations**. Thesis (Doctorate). Institute of Mathematics and Statistics, University of São Paulo, São Paulo, 2023.

The exponential integrators, a class of numerical methods used to solve differential equations, are the subject of this work. Specifically, we focus on explicit exponential integrators used to solve the differential equations describing the propagation of acoustic and elastic waves, with absorbing boundary conditions, encountered in seismic imaging applications. Among the various methods of exponential integrators, we analyze in detail the Faber polynomial-based method, a generalization of the well-known Chebyshev exponential integrator. Considering the state of the art of the Faber polynomial approximation, we discuss the main limitations of the method and propose solutions for them.

Among the theoretical results of the Faber polynomial approximation, we present a more accurate estimate of the approximation error of the method for normal matrices, than the one reported in the literature. We also show the importance of accurate estimates of the operator spectrum to ensure fast convergence of the method. Moreover, based on various numerical experiments, we outline a scheme to obtain eigenvalue estimates using only low-dimensional operators.

Among the numerical results, we observe that increasing the degree of Faber polynomials also increases the maximum time step size in temporal integration. Furthermore, in analyzing computational efficiency, we find that using higher degrees of Faber polynomials reduces the number of matrix-vector operations performed. The robustness of our numerical results is ensured by implementing various tests with different levels of complexity.

Additionally, we compare the Faber polynomial method with other explicit exponential integrators, such as the Krylov subspace method and high-order Runge-Kutta methods, along with classical low-order methods. Comparisons were made in experimental scenarios simulating real situations encountered in seismic imaging applications. Subsequently, we evaluate the stability, dispersion, numerical convergence, and computational efficiency of these methods. In our analysis, among high-order exponential integrators, the Krylov subspace-based method showed the best convergence results compared to all exponential integration methods. Allowing longer time steps for the same degree of approximation compared to other methods. Notably, when comparing methods for computational efficiency, we observed that high-order numerical methods can achieve efficiency comparable to low-order methods while allowing significantly larger time steps.

To highlight other applications that require an efficient solution to the wave equation, we present a new application in the field of mathematical modeling of cancer. As an innovative proposal, we developed a model based on continuum mechanics to simulate the effect of High-Energy Shock Wave (HESW) therapy on the growth of an avascular tumor. In this model, we demonstrate that by adjusting different parameters of the HESW therapy, we can qualitatively reproduce various tumor growth patterns, as reported in the literature. Additionally, we conduct a sensitivity analysis of the model to the various therapy parameters,

identifying the most influential elements in tumor growth.

Keywords: Exponential integrators. Wave equation. Faber polynomials. Linear elasticity. Mathematical modeling. Continuum mechanic. Cancer. High-Energy Shock Waves.

Contents

Chapter 1

Introduction

The propagation of waves is a physical phenomenon present in various aspects of our lives. Two of the main senses we use to perceive the world, sight and hearing, rely on specialized receptors evolved to perceive a limited range of wave frequencies (Radi and Rasmussen, 2013). Our pulsing heart, moving the circulatory system (Yomosa, 1987), and the electrical pulses of our brain (Graimann *et al.*, 2010), are also sources of waves. Beyond ourselves, the natural world is also full of propagating waves, manifesting in earthquakes, sea waves, pressure waves, gravity waves, and more. Virtually any object in motion generates waves, setting off a series of particle displacements until the energy is dissipated (Hendry, 2007).

Waves are not merely natural occurrences beyond our control; they also find applications that make use of their physical properties. One particularly intriguing application is subsurface imaging (Virieux *et al.*, 2017). The waves we perceive as light cannot penetrate opaque solid objects, but various other types of waves can. Consequently, we could use the information these waves bring back to understand the internal structure of objects. Subsurface imaging is actively researched in various domains, including mapping Earth's structure (Lowrie and Fichtner, 2020), monitoring the subsurface for CO_2 storage (Eiken, 2019), and exploring fossil fuels (Ikelle and Amundsen, 2018). It also extends its application to the extraction of geothermal energy (Huenges *et al.*, 2013), archaeological studies (Woelz and Rabbel, 2005), civil engineering (Niederleithinger *et al.*, 2016), and medical imaging (Theis and Bonomi, 2023) for visualizing internal body parts.

Our primary interest lies in the subsurface imaging bellow the sea floor, employing elastic waves with the objective of fossil fuel exploration. This technique is commonly used in the industry for the exploration and extraction of fossil fuels (Ikelle and Amundsen, 2018). The procedure involves acquiring data on the propagating waves at the specific regions of interest and developing a computer simulation of the subsurface such that the simulated waves match with the measured data. Figure 1.1 illustrates one of the typical data acquisition processes.

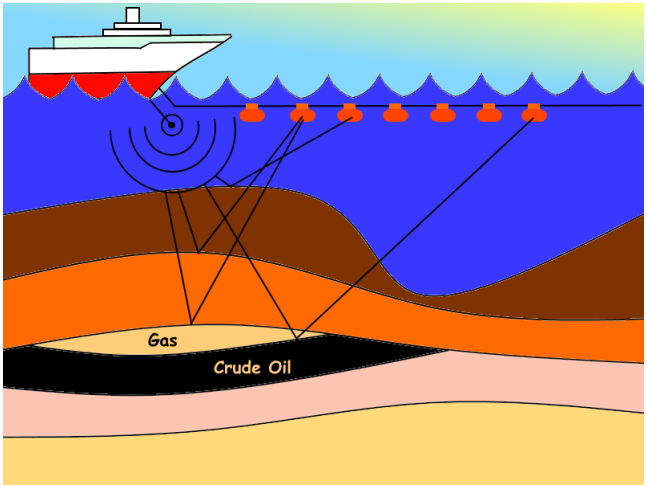

Figure 1.1: *The wave generated by the source travels through the water until it reaches the seafloor. Then, depending on the encountered material and its frequency, a portion of the wave will be reflected. The receptors at the surface register the time passed until the waves reach them and the amount of energy of the wave.*

At the initial time, a device creates an air explosion, generating acoustic waves that propagate through the water. Depending on their frequency and energy, a portion of these waves is reflected back to the surface and recorded by the receptors. Then, using the time taken to reach the receptor, along with the energy of the waves, it is possible to map the velocity field of the seafloor. This process is termed the inverse problem, and its resolution can be employed by other mathematical models to estimate the petrochemical parameters of the various materials constituting the ocean floor. Due to the complexity of the inverse problem, numerical methods established for seismic mapping take too long to calculate the solutions to the problem, difficulting their practical application. To solve the inverse problem, we have to solve several times the direct problem, consisting of the simulation of propagating waves.

Furthermore, in order to obtain more accurate representations of the subsurface, high-order numerical methods to solve the wave equations are required (Jing *et al.*, 2019; Wilcox *et al.*, 2010). Hence, the amount of computations and memory usage greatly escalates with the necessity of solving the inverse problem iteratively. This challenge creates an active area in numerical analysis, where ongoing research focuses on developing new algorithms to enhance the solutions accuracy, or to reduce computational time, sometimes through the utilization of parallel environments (Martinez *et al.*, 2009; Pranab J Deka *et al.*, 2023).

In this research, we aim to tackle the numerical solution of wave propagation equations, focusing on its application in seismic imaging. A distinctive aspect of this application lies in the necessity to solve wave equations across an extensive numerical domain, so vast that it is almost impossible to simulate in its entirety. Consequently, due to the impracticality of considering the complete region, only the specific area of interest is simulated, while implementing absorbing boundary conditions (ABC) at its limits. This approach allows us to replicate an infinite domain, and avoid wave reflections at the boundaries of the reduced domain.

The incorporation of ABC into the wave propagation equations transforms what is originally a purely hyperbolic problem into one that is nearly hyperbolic. This transformation holds significant implications for the numerical method under investigation in our work—a generalization of the explicit exponential integrator based on Chebyshev polynomials.

Over the past few decades, exponential integrators, a category of numerical algorithms, have emerged as powerful tools with successful applications in diverse fields. Their effectiveness has been demonstrated in the numerical solving of equations of mathematical physics (Pototschnig *et al.*, 2009; Peixoto and Schreiber, 2019; Loffeld and Tokman, 2013), often outperforming traditional schemes. Some advantages of exponential integrators lie in their ability to maintain favorable dispersion properties while permitting the use of larger time steps (Schreiber *et al.*, 2019).

Despite their success in these areas, the application of exponential integrators in the solution of the linear wave propagation equations is not completely understood. There have been published a few studies in this direction (Tal-Ezer *et al.*, 1987; Tessmer, 2011; Kosloff *et al.*, 1989; Kole, 2003; Zhang *et al.*, 2014), but most of them deal with simplified versions of the wave equations that are not well-suited for seismic imaging applications. In the work by Kole (2003), an explicit exponential integrator, utilizing Chebyshev polynomials of arbitrary order in time, is applied to elastic wave equations. However, it cannot solve the wave equations with absorbing boundary conditions, rendering it impractical for its usage in seismic imaging. Studies such as Tal-Ezer *et al.*, 1987; Tessmer, 2011; Kosloff *et al.*, 1989 also employ Chebyshev expansions in conjunction with ABCs. Nonetheless, the numerical results are primarily validated using simplistic ABCs, and there is a lack of a proof demonstrating convergence for these boundary conditions. In contrast, Zhang *et al.* (2014) presents an implicit exponential integrator of low order in time for solving the wave equation with absorbing boundary conditions. Nevertheless, while implicit schemes offer good stability properties allowing for larger time steps, they come with a significant computational cost, and there is no assurance of good numerical accuracy.

Explicit exponential integrators using Chebyshev polynomials have been consistently acknowledged by several authors as an efficient scheme with rapid convergence and straightforward implementation (Bergamaschi and Vianello, 2000; Hochbruck and Ostermann, 2010; Kole, 2003). This method has demonstrated success in solving wave equations (Kole, 2003), achieving high accuracy and the capability to compute solutions using remarkably large time steps. Nonetheless, the Chebyshev exponential was originally designed for use when the discrete system defines a symmetric or antisymmetric operator. However, in seismic wave propagation, the inclusion of ABC in the wave propagation equations breaks the antisymmetry of the usual wave operator, restricting the applicability of Chebyshev exponential integration for seismic problems.

To address this limitation, a generalization to non-symmetric (or non-antisymmetric) operators has been proposed in Bergamaschi, Caliari, *et al.* (2003) using Faber polynomials. They demonstrated that Faber polynomials, obtained by stretched and displaced Chebyshev polynomials, serve as a generalization capable of handling systems with non-symmetric matrices.

As the first contribution of this thesis, we formulate the exponential integrators based

on Faber polynomials for the resolution of acoustic and elastic wave equations, incorporating the widely employed Perfectly Matching Layers (PML) absorbing boundary condition (Assi and Cobbold, 2017). Then, considering the use of the scaling and squaring optimization technique for Faber polynomials, we establish an error bound for the numerical approximation of the Faber exponential integrator, specifically for operators represented by normal matrices. Notably, our error estimation demonstrates improvement over a prior bound reported by Bergamaschi and Vianello (2000). Moreover, since the construction of Faber polynomials requires the usage of the operator spectrum, we conduct an in-depth analysis of the eigenvalue distribution of both discrete and continuous operators associated with wave equations. This comprehensive analysis considers various formulations of wave equations, equation parameters, and spatial dimensions, leading to the proposal of precise estimates for the operator spectrum boundaries. Additionally, we analyze the performance of Faber approximations by studying stability, dispersion, convergence, and computational efficiency. To achieve this, we implement the method in solving the wave equation across a range of numerical examples with diverse complexities, ensuring the reliability and robustness of our results.

Next, to assess the relevance of Faber polynomials in the solution of the wave propagation equations, we conduct a comparative analysis of the Faber polynomials method with other exponential integrators based on Faber polynomials and several low-order methods. Specifically, we consider exponential integrators based on Krylov subspace projections, and high-order Runge-Kutta approximation, alongside classical low-order methods such as Leap-frog, fourth-order and four-stage Runge-Kutta (RK4-4), second-order and three-stage Runge-Kutta (RK3-2), and seventh-order and nine-stage Runge-Kutta (RK9-7). For this analysis, we consider various critical aspects, such as dispersion, dissipation, convergence, and computational cost. We examine numerical dispersion and convergence in a homogeneous medium with a single propagating signal, decomposing its frequencies through the Fourier transform. On another hand, the numerical convergence is studied using practical examples designed to replicate conditions encountered in real-field scenarios in seismic imaging applications.

In addition to seismic imaging, there exist other fields where efficient computation of the wave propagation equations is required. As an innovative proposal, we have developed a mathematical model based on continuum mechanics to simulate the impact of a therapy consisting of the generation of elastic for cancer treatment.

High-Energy Shock Wave (HESW) therapy, or Shock Wave Lithotripsy (SWL) (López-Marin *et al.*, 2018), is a medical technique commonly employed for procedures like disintegrating kidney stones and treating fractured bones in humans (Shrivastava and Kailash, 2005). In the latter part of the previous century, studies conducted *in vitro* and in pre-clinical settings demonstrated the potential of this methodology for treating growing tumors (Russo *et al.*, 1986; Hoshi *et al.*, 1991; Maruyama *et al.*, 1995). Experimental findings indicated a delay in tumor growth with HESW therapy, and when combined with chemotherapy, a more substantial delay and even tumor regression has been observed (Gamarra *et al.*, 1993; Oosterhof *et al.*, 1990). However, the precise mechanisms underlying this therapy remain not fully understood, and there is a scarcity of mathematical studies intending to simulate its effects on tumors.

Essentially, HESW therapy induces pressure changes on tissue. Therefore, it is crucial to investigate the impact of these changes on volumetric stresses within tumors and their effects on growth. Addressing this requires a mathematical model of a tumor grounded in continuum mechanics capable of simulating the mechanical therapy involving shock waves. To our knowledge, there is a lack of published research on this specific subject. Consequently, we simulate the application of High-Energy Shock Wave therapy on tumors. The tumor, considered as a linear elastic material with the ability to alter its volume, displaces the external medium during anisotropic growth, connected to it by its boundary under a perfect contact condition. The external medium is modeled as a homogeneous and linear elastic isotropic material, following Hooke's law in three dimensions. As a result, our model is grounded in the linear elasticity theory of continuum mechanics.

A major challenge in these mathematical models lies in acquiring experimental data for the model parameters, especially in the realm of mechanical models in biology, where elasticity constants of tissues are needed. To support this, we also provide a concise summary of published data regarding the parameters necessary for a continuum mechanics-based tumor model, with standardized physical magnitudes, and the main experimental layouts outlined in relevant references concerning HESW therapy in both *in vitro* and *in vivo* experiments.

Primary objective

Investigation of the numerical features of explicit exponential integrators when solving the linear elastic wave propagation equations with ABC.

Specific objectives

1. Adapt the Faber polynomial approximation to efficiently solve the wave propagation equations with ABC, while evaluating its numerical properties and computational cost.
2. Determine the practical applicability of the Faber polynomials in solving the wave propagation equations by comparing them with other explicit exponential integrators and commonly used low-order schemes in the field of seismic imaging.
3. Propose a novel application of the wave propagation equations where an efficient computation of their solutions is crucial.

Thesis structure

This thesis comprises three main chapters, each corresponding to an article either submitted for publication in a specialized journal or in the final stages of submission. These articles enclose the primary findings of the research, starting with the adaptation of an explicit exponential integrator method to solve the wave equations coupled with PML

absorbing boundary conditions. Subsequently, a comprehensive comparison is conducted between exponential integrators and various time integration methods in real-world seismic imaging scenarios. Additionally, a novel application of wave propagation with ABC is proposed in the modelling of tumor therapy.

In Chapter 2 it is investigated the application of an exponential integrator, utilizing Faber polynomials, to quasi-hyperbolic problems such as wave propagation equations with ABC. The focus lies on improving the method's efficiency by closely examining its characteristics and the system of equations to solve. This chapter thoroughly analyzes the numerical aspects of Faber polynomials, including stability, dispersion, accuracy, and computational efficiency across a wide range of approximation orders and time steps, illustrated through diverse numerical examples.

Building upon the insights gained from Faber approximation, Chapter 3 complements the previous findings by conducting a comparative study between the proposed method and other explicit exponential integrators, as well as commonly used time integration methods. For the analysis we use velocity fields resembling real-world data of seismic imaging application, and compare the methods acording to various numerical features such as dispersion, dissipation, accuracy, computational efficiency, and memory usage.

Ackgnowleding that the necessity for efficient calculation of wave propagation equations with ABC extends beyond seismic imaging, Chapter 4 presents a novel mathematical model for HESW therapy applied to growing tumors. This therapy involves the propagation of elastic shock waves in a 3D heterogeneous medium with an average application time of approximately four seconds. Consequently, it is required a fast solver of the wave equations given the amount of large time interval to compute the solution and the dimensionality of the problem.

Lastly, Chapter 5 encapsulates the primary conclusions drawn from this research, synthesizing the key findings derived from the three papers.

Scientific production

Publications in specialized journals

1. Fernando V. Ravelo, Pedro S. Peixoto, and Martin Schreiber. *An explicit exponential integrator based on Faber polynomials and its application to seismic wave modeling*. Journal of Scientific Computing. (Status: Accepted)

2. Fernando V. Ravelo, and Martin Schreiber, Pedro S. Peixoto. *High-order exponential integration for seismic wave modeling*. (Status: Finished, and ready to be submitted to the journal of Computational Geosciences.)

3. Fernando V. Ravelo, Reinaldo R. Ramos, and Pedro S. Peixoto. *Incorporating High-Energy Shock Waves therapy into a continuum model of a tumor growth*. (Status: In the final stages for submission.)

Presentations at events

1. European-Latin-American Conference of Theoretical and Applied Mechanics. *Effect of shock waves in the interplay between stress and anisotropic growth of an avascular tumor model*. 2019. (Congress)
2. 32 Coloquio Brasileiro de Matemática. *A mathematical model of the High-Energy Shock Wave therapy in a growing avascular tumor in the framework of continuum mechanics*. 2019. (Congress)
3. Energy Transition Research & Innovation. *Solving the wave equation with exponential integrators*. 2019. (Congress)
4. Latin American Congress on Industrial and Applied Mathematics. *The application of a time exponential integrator to the wave equations, oriented to seismic imaging*. 2023. (Congress, obtaining a best poster award).

Intership

During my six-month internship at the Jean Kuntzmann Laboratory, Université Grenoble Alpes, Grenoble, France, I collaborated closely with co-advisor Martin Schreiber. I attended to a course on High Performance Computing (HPC), participated in the "SEISCOPE" workshop, and presented the research to the laboratory's researchers, including specialists in seismic imaging.

Chapter 2

An explicit exponential integrator based on Faber polynomials and its application to seismic wave modeling

As an initial exploration of the application of explicit exponential integrators to the wave equations, we have chosen one of the most well-known and straightforward schemes - a generalisation of the Chebyshev polynomial approximation. The intention is to study this method in detail, disussing the state of the art of the method and suggesting possible extensions or directions for improvement, aiming at its most efficient implementation. Subsequently, we study the numerical capabilities of the Faber polynomials when applied to the solution of linear wave equations with ABC. Among the various possible choices of ABC, we opted for the PML. Not only is PML one of the most widely used in seismic imaging problems, but it is also one of the most complex to implement and computationally expensive. This complexity makes it an ideal choice for studying the Faber method in one of the more challenging scenarios.

One of the fundamental results of Faber approximation is the estimation of the convex envelope of the operator spectrum without the need to compute its eigenvalues directly. This estimation enables the construction of an optimal ellipse in practical applications, which significantly improves the convergence rate of the Faber polynomials. As demonstrated in Section 2.2.1, the maximum error of the Faber polynomial approximation occurs at the boundary of this ellipse, which is circumscribed around the convex hull of the spectrum. Thus, this ellipse serves as an optimal set for defining the Faber polynomials, since the error does not exceed that of the convex hull.

This chapter consists of the accepted publication of Ravelo F (2023) in the Journal of Scientific Computing, co-authored with my advisor Pedro Peixoto and co-advisor Martin Schreiber. It represents a first approach to understand the application of explicit exponential integrators, in particular the Faber polynomial approximation, within the domain of seismic imaging. Not only do we describe its numerical properties, such as stability, dispersion,

convergence and computational efficiency. But by illustrating the existing challenges, we also contribute to the development of a more efficient application.

Noname manuscript No.
(will be inserted by the editor)

An explicit exponential integrator based on Faber polynomials and its application to seismic wave modeling

Fernando V. Ravelo · Pedro S. Peixoto · Martin Schreiber

Received: date / Accepted: date

Abstract Exponential integrators have been applied successfully in several physics-related differential equations. However, their application in hyperbolic systems with absorbing boundaries, like the ones arising in seismic imaging, still lacks theoretical and experimental investigations.

The present work conducts an in-depth study of exponential integration using Faber polynomials, consisting of a generalization of a well-known exponential method that uses Chebyshev polynomials. This allows solving non-symmetric operators that emerge from classic seismic wave propagation problems with absorbing boundaries.

Theoretical as well as numerical results are presented for Faber approximations. One of the theoretical contributions is the proposal of a sharp bound for the approximation error of the exponential of a normal matrix. We also show the practical importance of determining an optimal ellipse encompassing the full spectrum of the discrete operator to ensure and enhance the convergence of the Faber exponential series. Furthermore, based on estimates of the spectrum of the discrete operator of the wave equations with a widely used absorbing boundary method, we numerically investigate the stability, dispersion, convergence, and computational efficiency of the Faber exponential scheme.

Overall, we conclude that the method is suitable for seismic wave problems and can provide accurate results with large time step sizes, with computational efficiency increasing with the increase of the approximation degree.

Fernando V. Ravelo (ORCID: 0000-0003-1867-2123) E-mail: fernanvr@ime.usp.br · Pedro S. Peixoto (ORCID: 0000-0003-2358-3221) E-mail: ppeixoto@usp.br
Instituto de Matemática e Estatística, Universidade de São Paulo, Brazil

Martin Schreiber (ORCID: 0000-0002-4430-6779) E-mail: martin.schreiber@univ-grenoble-alpes.fr
Université Grenoble Alpes / Laboratoire Jean Kuntzmann, France
Technical University of Munich, Germany

Exponential integrator · Faber polynomial · Wave equation · Absorbing boundaries · Eigenvalue distribution

MSC: 65N22

1 Introduction

Producing images from the subsurface using elastic waves is an important and challenging problem in geophysics [22]. From a mathematical perspective, this process is divided into two sub-problems: the direct problem, consisting of solving the wave propagation equations, and the adjoint/reverse problem, which is part of the optimization problem that generally uses the adjoint method. Both tasks rely on the numerical solution of the propagating waves in the medium of interest. Given the requirement of repeatedly solving the wave equations in the inverse problem, the overall computational cost and memory requirements tend to be very large. Additionally, this problem usually requires high-order numerical methods for accurate representations of wave dispersion to ensure adequate assessment of subsurface media interfaces [24, 43]. Naturally, better algorithms are desired to obtain more accurate representations of the subsurface, posing a relevant challenge for numerical method development.

A particular class of methods, known as exponential integrators, have been shown to outperform classical schemes in several partial differential equations (PDEs) models from several applied areas in terms of accuracy and computational performance (e.g., [9, 14, 28, 34, 36, 44]). For the specific case of linear differential equations, there have been developed specialized exponential integrators. Among these approaches, one of the pioneering works on exponential integrators is based on Krylov subspace projections, and several algorithms have been proposed based on this method [18, 33, 37]. Other well-known schemes rely on Chebyshev and Faber polynomials, characterized by their straightforward implementation and super-linear convergence properties [7, 25]. Nonetheless, a notable requirement of these methods is the need for knowledge of the spectrum of the linear operator of the equation. In this sense, they are related to another algorithm based on interpolating polynomials at the Leja points [10, 16], which also needs the operator spectral distribution. These are just some . Other methods examples of exponential integrators can be found in the comprehensive reviews of Hochbruck and Ostermann [20], and Moler and Van Loan [29].

However, the study of such schemes for solving the wave equations is not yet well established for seismic applications. Only a few studies have been conducted in this direction [25, 44]. In Kole [25], an explicit exponential integrator of arbitrary order in time using Chebyshev polynomials is applied to the elastic wave equations, but without the possibility to consider absorbing boundary conditions, hence rendering them inadequate for practical scenarios. In Zhang et al. [44], an implicit exponential integrator of low order in time is developed to solve the wave equation with absorbing boundary conditions. Nonetheless,

although implicit schemes have good stability properties, allowing larger time steps, they are very costly, and the numerical error is not granted to be small.

Some authors have recurrently mentioned explicit exponential integrators based on Chebyshev polynomials as an efficient scheme of rapid convergence and easy implementation [6, 20, 35], with further hardware-aware possible optimizations (c.f. Huber et al. [21] for exploiting caches). They have been used to solve the wave equations [25], obtaining high accuracy in the approximations and being able to compute the solution using remarkably large time steps. However, no analysis of the computational efficiency of the approximation was performed. Also, the proposed Chebyshev exponential was designed to be used only when the discrete system defines a symmetric or an antisymmetric operator. Nonetheless, in seismic wave propagation, an infinite domain is imitated using a limited area domain alongside absorbing boundary conditions to avoid spurious reflections. Such non-reflective boundary conditions usually break the anti-symmetry of the usual wave operator, therefore making Chebyshev exponential integration of very limited applicability for seismic problems. Based on Faber polynomials, a generalization to non-symmetric (or non-anti-symmetric) operators has been proposed in Bergamaschi et al. [7]. They showed that Faber polynomials are a generalization of Chebyshev polynomials obtained by stretching and displacing Chebyshev polynomials, which are able to handle systems with non-symmetric matrices. Moreover, the method was compared with a Krylov subspace algorithm, resulting in comparable accuracy and computational efficiency. Withal, the proposed method is designed for and used to solve advection-diffusion equations but not wave equations. Alongside, as in Kole [25], there was no analysis of the optimal polynomial degree looking towards computational efficiency and competitiveness with respect to traditional methods. Therefore, this work focuses on investigating the theoretical and numerical properties of Faber exponential methods and their application to seismic wave propagation problems. The objective is to provide a foundational step for future research comparing Faber polynomials with other exponential integrators and classical schemes in this particular setting.

First, we develop the exponential integrators based on Faber polynomials to solve acoustic and elastic wave equations with a commonly used absorbing boundary condition, the Perfectly Matching Layers (PML) [4]. Then, considering the optimization technique of scaling and squaring, we establish an error bound of the numerical approximation of the Faber exponential for operators given by a normal matrix. Notably, our error estimation demonstrates improvement over a prior bound reported by Bergamaschi and Vianello [6]. Furthermore, as a strategy to optimize the convergence of the Faber exponential series, we analyze the eigenvalues' distribution of the discrete and the continuous operators of the wave equations. This analysis encompasses different formulations of the wave equations, equation parameters, and spatial dimensions, ultimately leading us to propose sharps estimates of spectrum boundaries. A thorough numerical investigation of the stability and dispersion properties is also performed, calculating the Courant-Friedrichs-Lewy (CFL) number and

the dispersion error for several polynomial degrees, while searching for optimal polynomials. We also study the performance of Faber approximations in practice by solving the wave equation within several numerical examples with different levels of complexity. To ensure robustness in our results, we investigate stability, dispersion, convergence, and computational efficiency by varying the model parameters in the continuum and the discrete models. Overall, this work contributes to be the first description and investigation of the viability of Faber exponential integration for classic seismic wave propagation problems with absorbing layers. Our findings highlight the competitiveness of the scheme in terms of accuracy and computational cost.

This paper is organized as follows. In the next section, we introduce the basic formulations used to solve a general problem using exponential integrators, with subsequent focus on using Faber polynomials on the exponential approximations. We also include an analysis of error bound estimates for the system of normal matrices. In Section 3, we present the wave equations with PML absorbing boundaries condition, with their variations, the numerical considerations, and the experiments we use throughout the work. The study of the spectrum of the discrete spatial operators of the wave equations is in Section 4, where we also derived formulas for the convex hull of the respective problem's eigenvalues. Section 5 contains the theoretical stability and dispersion error analysis, together with an estimate of the method efficiency according to these criteria. Further, we conduct several numerical experiments in Section 6 to compare the accuracy and efficiency for different degrees of approximation across the seven numerical experiments designed in Section 3. Section 7 concludes the work and summarizes the principal results.

2 Exponential integrators and Faber polynomials

This section briefly presents the theory of exponential integrators, followed by a description of Faber polynomials. We also discuss some aspects of Faber polynomials, such as the error bounds of the approximation and the dependence of the convergence on the region where the polynomials are defined.

2.1 Exponential integrator perspective

As described in Hochbruck and Ostermann [20], and Al-Mohy and Higham [2], exponential integrators are a class of time integrating methods used to solve ordinary differential equations of first order in time,

$$\frac{d\boldsymbol{u}(t)}{dt} = \boldsymbol{H}\boldsymbol{u}(t) + \boldsymbol{f}(t, \boldsymbol{u}(t)), \quad \boldsymbol{u}(t_0) = \boldsymbol{u}_0, \tag{1}$$

where $\boldsymbol{u}(t)$ and $\boldsymbol{u}_0$ are functions in $\mathbb{C}^n$, $\boldsymbol{H} \in \mathbb{C}^{n\times n}$ is usually a discretization of a continuous operator (originating from a partial differential equation, for instance), and $\boldsymbol{f}$ may be a non-linear function, with $\boldsymbol{f} : \mathbb{R} \times \mathbb{C}^n \to \mathbb{C}^n$.

Then, an exponential integrator is defined as an approximation of the semi-analytic solution of the constants variation formula,

$$\boldsymbol{u}(t) = e^{(t-t_0)\boldsymbol{H}}\boldsymbol{u}_0 + \int_{t_0}^{t} e^{(t-\tau)\boldsymbol{H}}\boldsymbol{f}(\tau, \boldsymbol{u}(\tau))d\tau. \tag{2}$$

Depending on how the integral term in (2) is approximated, different types of exponential integrators are defined (see Hochbruck and Ostermann [20] for a review). For our particular application to seismic imaging, $\boldsymbol{f}$ represents the source term, which we will utilize later in its Taylor expanded form. In such case, Higham [19] shows that (2) can be transformed into the calculation of the exponential of a slightly larger matrix,

$$\tilde{\boldsymbol{H}} = \begin{pmatrix} \boldsymbol{H} & \boldsymbol{W} \\ \boldsymbol{0} & \boldsymbol{J}_{p-1} \end{pmatrix},$$

where the columns of the matrix $\boldsymbol{W}$ are formed by the values of the function $\boldsymbol{f}$, and the approximations of the first $p-1$ derivatives of $\boldsymbol{f}$ at t_0,

$$\boldsymbol{W} = \left[\frac{d^{p-1}}{dt^{p-1}}\boldsymbol{f}(t_0, \boldsymbol{u}_0) \middle| \frac{d^{p-2}}{dt^{p-2}}\boldsymbol{f}(t_0, \boldsymbol{u}_0) \middle| \cdots \middle| \frac{d}{dt}\boldsymbol{f}(t_0, \boldsymbol{u}_0) \right],$$

and $\boldsymbol{J}_{p-1}$ is a square matrix of dimensions $p \times p$ with value one in the upper diagonal and all the other elements zero,

$$\boldsymbol{J}_{p-1} = \begin{pmatrix} \boldsymbol{0} & \boldsymbol{I}_{(p-1)\times(p-1)} \\ 0 & \boldsymbol{0} \end{pmatrix},$$

where $\boldsymbol{I}_{(p-1)\times p-1}$ is the identity matrix of dimension $p-1$.

Consequently, the information about the source term is contained in the matrix $\boldsymbol{W}$, and the solution of the system can be written as

$$\boldsymbol{u}(t) = \begin{bmatrix} \boldsymbol{I}_{n\times n} & \boldsymbol{0} \end{bmatrix} e^{(t-t_0)\tilde{\boldsymbol{H}}} \begin{bmatrix} \boldsymbol{u}_0 \\ \boldsymbol{e}_p \end{bmatrix}, \tag{3}$$

where $\boldsymbol{e}_p \in \mathbb{R}^p$ is a vector with zero in its firsts $p-1$ elements and one in its last element, and $\boldsymbol{I}_{n\times n}$ is the identity matrix of dimension n. This approach is a generalization of the result in the previous work of [37], where the function $\varphi_1(\boldsymbol{H})\boldsymbol{c} = \frac{e^{\boldsymbol{H}} - \boldsymbol{I}_{n\times n}}{\boldsymbol{H}}\boldsymbol{c}$ is computed.

As with classical methods, we define a time-step size Δt and calculate the solution at $t_k = t_{k-1} + \Delta t$ as

$$\boldsymbol{u}(t_k) = \begin{bmatrix} \boldsymbol{I}_{n\times n} & 0 \end{bmatrix} e^{\Delta t\tilde{\boldsymbol{H}}} \begin{bmatrix} \boldsymbol{u}(t_{k-1}) \\ \boldsymbol{e}_p \end{bmatrix},$$

and the sub-matrix $\boldsymbol{W}$ of $\tilde{\boldsymbol{H}}$ now relates to an evaluation of $\boldsymbol{f}$ and its derivatives at time t_{k-1}.

The calculation of the matrix exponential is one of the core steps of exponential integrators and several families of methods to approximate the application of the exponential of a matrix $\boldsymbol{H}$ onto a vector $\boldsymbol{u}_0$ have been proposed (see Moler and Van Loan [29]). We continue by investigating such operations with the help of Faber's polynomials. From this point onward, we will represent the amplified matrix $\tilde{\boldsymbol{H}}$ as $\boldsymbol{H}$ for the sake of notation simplicity, wherever a source term is considered in the equation.

This research will use a Taylor expansion of the term $\boldsymbol{f}$ of the same order as the matrix exponential approximation. This ensures that the effective order of the temporal scheme is in agreement between matrix exponential (in Eq. (3)) and source part (in Eq. (2)), without much added computational cost. This is because the order of the expansion (p) is typically several orders of magnitude smaller than the dimension of the discrete operator $\boldsymbol{H}$. Moreover, considering that $\boldsymbol{f}$ is usually a known function, the partial derivatives of the Taylor expansion will be calculated symbolically.

2.2 Faber polynomials

Given a degree j, and a square matrix $\boldsymbol{H}$, Faber's polynomials are defined as $\boldsymbol{F}_j(\boldsymbol{H})$, with

$$\boldsymbol{F}_0(\boldsymbol{H}) = \boldsymbol{I}_{n\times n}, \quad \boldsymbol{F}_1(\boldsymbol{H}) = \boldsymbol{H}/\gamma - c_0\boldsymbol{I}_{n\times n}, \tag{4}$$

$$\boldsymbol{F}_2(\boldsymbol{H}) = \boldsymbol{F}_1(\boldsymbol{H})\boldsymbol{F}_1(\boldsymbol{H}) - 2c_1\boldsymbol{I}_{n\times n}, \tag{5}$$

$$\boldsymbol{F}_j(\boldsymbol{H}) = \boldsymbol{F}_1(\boldsymbol{H})\boldsymbol{F}_{j-1}(\boldsymbol{H}) - c_1\boldsymbol{F}_{j-2}(\boldsymbol{H}), \quad j \geq 3, \tag{6}$$

with

$$\gamma = \frac{a+b}{2}, \quad c_0 = \frac{d}{\gamma}, \quad c_1 = \frac{c_f^2}{4\gamma^2}, \quad b = \sqrt{a^2 - c_f^2}, \tag{7}$$

where the parameters a, c_f, and d, are set according to the spectrum of the operator $\boldsymbol{H}$. Faber's polynomials are considered a generalization of Chebyshev's polynomials because they are stretched and translated into Chebyshev's polynomials [38].

In Bergamaschi and Vianello [6], it is shown that given an ellipse $\mathcal{E}(d, c_f, a)$, symmetric with respect to the real axis (with center d, focuses $d \pm c_f$, and semi-major axis length a), if the spectrum $\sigma(\boldsymbol{H})$ of the matrix $\boldsymbol{H}$ is contained in the ellipse $\mathcal{E}(d, c_f, a)$, the Faber partial sums

$$S_m(\boldsymbol{H}) = \sum_{j=0}^{m} a_j \boldsymbol{F}_j(\boldsymbol{H}) \tag{8}$$

are maximally convergent to $e^{\boldsymbol{H}}$ in $\mathcal{E}(d, c_f, a)$, i.e.,

$$\lim_{m\to\infty} \sup \|e^{\boldsymbol{H}} - \boldsymbol{S}_m(\boldsymbol{H})\|^{1/m}_{\mathcal{E}(d,c_f,a)} = \lim_{m\to\infty} \sup \|e^{\boldsymbol{H}} - \boldsymbol{p}^*_m(\boldsymbol{H})\|^{1/m}_{\mathcal{E}(d,c_f,a)}, \tag{9}$$

where $\boldsymbol{p}^*_m$ is the polynomial of degree m that optimally approximates $e^{\boldsymbol{H}}$ in the infinite norm $\|\cdot\|_{\mathcal{E}(d,c_f,a)}$,

$$\|\boldsymbol{h}(.)\|_{\mathcal{E}} = \max_{x \in \mathcal{E}} |\boldsymbol{h}(x)|. \tag{10}$$

In such a case, the polynomial coefficients a_j are obtained from

$$a_j = \int_0^1 exp\left(\left(\gamma + \frac{c_f^2}{4\gamma}\right)\cos(2\pi\theta) + d + i\left(\gamma - \frac{c_f^2}{4\gamma}\right)\sin 2\pi\theta\right) e^{-ij2\pi\theta} d\theta. \tag{11}$$

As pointed out in Bergamaschi et al. [7], if the ellipse where the polynomials are defined is large, it can be difficult to compute the coefficients (11) accurately. When the ellipse capacity γ increases, the magnitude of the term inside the integral (11) grows several orders of magnitude, introducing significant numerical errors. Therefore, calculating the coefficients can require higher arithmetic precision in their calculations. Here, we used double precision in all calculations, which was enough to ensure an adequate representation.

Optimization of exponential integrator methods to reduce computational cost can be achieved using the scaling and squaring technique for large matrices [19, 29]. It is based on the parameters $s \geq 1$, and $z \in \mathbb{N}$, such that the error of the truncated Faber series

$$e^{\boldsymbol{H}} = \left(e^{s^{-1}\boldsymbol{H}}\right)^s \approx \left(\sum_{j=0}^{m} a_j \boldsymbol{F}_j(s^{-1}\boldsymbol{H})\right)^s \tag{12}$$

remains under a fixed threshold, while the amount of matrix-vector operations (MVOs) is minimized. The number of MVOs required by Eq. (12) is $s \times m$, where m is the degree of the polynomial used in the approximation of $e^{s^{-1}\boldsymbol{H}}$. This approach was successfully implemented for Padé approximations of the exponential in the works of Higham [19], and Al-Mohy and Higham [1], connecting it later to exponential integrators in Al-Mohy and Higham [2]. However, reliable error bounds are necessary to estimate the optimal s and m without evaluating the series and comparing them with the exact solution. This point has been discussed in the works of Higham [19] and Al-Mohy and Higham [1], where sharp bounds for the Padé approximation were required. For Faber polynomials, this is still an open problem. Nonetheless, the next subsection aims to provide further insights in this direction.

2.2.1 Faber exponential error bounds

A general expression for the error (on the usual Euclidean norm for $\mathbb{C}^n$, $\|.\|_2$) is stated in Bergamaschi and Vianello [6],

$$\|e^{\boldsymbol{H}} - \boldsymbol{S}_m(\boldsymbol{H})\|_2 \leq \mathrm{cond}_2(\boldsymbol{P})\|\exp(.) - \boldsymbol{S}_m(.)\|_{\mathcal{E}}, \tag{13}$$

where $\boldsymbol{S}_m$ is the partial sum of the first $m+1$ terms of the series in the recurrence (5)-(6), $\boldsymbol{P}$ is the diagonalization matrix of $\boldsymbol{H}$ (i.e., $\boldsymbol{P}^{-1}\boldsymbol{H}\boldsymbol{P}$ is a

diagonal matrix), $\text{cond}_2(\boldsymbol{P}) = \|\boldsymbol{P}\|_2\|\boldsymbol{P}^{-1}\|_2$, and $\|.\|_{\mathcal{E}}$ is the infinite norm over the ellipse $\mathcal{E}$ (see (10)), enclosing the spectrum of $\boldsymbol{H}$.

Expression (13) has the complication that determining $\text{cond}_2(\boldsymbol{P})$ is a difficult challenge for large matrices, as the ones resulting after discretizing spatial derivatives in partial differential equations. In addition, to the authors' best knowledge, a general bound for the term $\|\exp(.) - \boldsymbol{S}_m(.)\|_{\mathcal{E}}$ has not been reported in the literature, yet.

In Bergamaschi and Vianello [6], they present a bound for the second term on the right of (13),

$$\|\exp(.) - \boldsymbol{S}_m(.)\|_{\mathcal{E}} \leq \begin{cases} \frac{8\gamma}{m}\exp\left(\frac{4\gamma^2}{4\gamma-m} + d - \frac{m^2}{4\gamma} + \frac{c^2(4\gamma-m)}{16\gamma^2}\right), & m \leq 2\gamma, \\ 4\exp\left(d + \frac{c^2}{4m}\right)\left(\frac{e\gamma}{m}\right)^m, & m > 2\gamma, \end{cases} \tag{14}$$

where γ is the mean of the semi-axis of the ellipse $\mathcal{E}$, d is its center, c is the eccentricity, e is the base of the natural logarithm, and m is the polynomial degree used. The second part of (14), when $m > 2\gamma$, represents an asymptotic super-linear convergence. But when $m \leq 2\gamma$, the expression in (14) is very pessimistic and is not appropriate for practical applications (see Bergamaschi and Vianello [6]). Furthermore, although it was not stated in their research, the inequality (14) is only guaranteed if the ellipse is strictly contained in the right half plane (see Moret and Novati [30]). However, for many problems of interest, including the wave problems to be discussed in this work, there are eigenvalues with negative real parts; therefore, expression (14) is not fulfilled.

Here, we propose an error bound that improves (14) when the ellipses are in the positive half plane and is also valid for any ellipse. Let $m_{\epsilon/2}$ be the polynomial degree such that the Faber approximation error is at most $\epsilon/2$. Then, for all $m < m_{\epsilon/2}$ we have,

$$\begin{aligned} \|\exp(.) - \boldsymbol{S}_m(.)\|_{\mathcal{E}} &\leq \|S_{m_{\epsilon/2}}(.) - \boldsymbol{S}_m(.)\|_{\mathcal{E}} + \|\exp(.) - \boldsymbol{S}_{m_{\epsilon/2}}(.)\|_{\mathcal{E}} \\ &= \left\| \sum_{j=m+1}^{m_{\epsilon/2}} a_j \boldsymbol{F}_j(.) \right\|_{\mathcal{E}} + \|\exp(.) - \boldsymbol{S}_{m_{\epsilon/2}}(.)\|_{\mathcal{E}}. \\ &\leq \sum_{j=m+1}^{m_{\epsilon/2}} |a_j| \|\boldsymbol{F}_j(.)\|_{\mathcal{E}} + \|\exp(.) - \boldsymbol{S}_{m_{\epsilon/2}}(.)\|_{\mathcal{E}} \\ &\leq \sum_{j=m+1}^{m_{\epsilon/2}} |a_j| \|\boldsymbol{F}_j(.)\|_{\mathcal{E}} + \frac{\epsilon}{2}. \end{aligned} \tag{15}$$

The polynomial coefficients a_j can be calculated by explicit formulas using (11). Thus, the unknowns in (15) are the norm over the ellipse $\mathcal{E}$ of the polynomials $\boldsymbol{F}_j$, and $m_{\epsilon/2}$ discussed next.

From Section 2, we know that $\boldsymbol{F}_j$ are stretched and translated Chebyshev polynomials, then, all its roots are located at the points

$$r_k = d + c_f \cos\left(\frac{1+2k}{2j}\pi\right), \quad k = 0, ..., j-1.$$

Therefore, as stated in Munch [31], the extreme values of the polynomials are attained at the points over the ellipse $\mathcal{E}$. Consequently, one of those points is where the ellipse cuts the line passing by its foci. Hence, we can compute $\|\boldsymbol{F}_j(.)\|_{\mathcal{E}}$ in a straightforward way by evaluating the polynomial at these two points.

To estimate $m_{\epsilon/2}$, we may calculate the series in (15) until the new terms are smaller than $\epsilon/2$. In practice, due to the extremely fast convergence to zero of Faber coefficients a_j, the rest of the series $\|\exp(.) - \boldsymbol{S}_{m_{\epsilon/2}}(.)\|_{\mathcal{E}}$ will be negligible when compared with the terms already computed.

We compare bounds (14) and (15), by means of numerical experiments, using arbitrary diagonalizable matrices $\boldsymbol{H} = \boldsymbol{P}\boldsymbol{D}\boldsymbol{P}^{-1}$. To ensure that the condition number of the diagonalization matrix $\boldsymbol{P}$ is 1, we take real normal matrices $\boldsymbol{H}$, since in this case $\boldsymbol{P}$ is unitary. Therefore, the condition number of $\boldsymbol{P}$ in the Euclidean norm is 1, i.e., $\text{cond}_2(\boldsymbol{P}) = 1$.

In the following illustrative examples, we set $\boldsymbol{P}$ as a random orthonormal matrix (therefore unitary)[1] with dimensions 60×60. Then, we define the eigenvalues of the diagonal matrices $\boldsymbol{D}$ as the composition of 10 randomly generated real numbers and 50 randomly sampled complex eigenvalues, symmetric with respect to the real axis. We present the results of two experiments, for which the ranges of the randomly generated eigenvalues are given by:

1. Experiment 1 (Figures 1a and 1b): real numbers between $[2.8,\ 10.8]$ and complex values in the domain $[2.8,\ 10.8] \times i[-3,\ 3]$.
2. Experiment 2 (Figures 1c and 1d): real numbers between $[-8,\ 2]$ and complex values in the domain $[-8,\ 2] \times i[-11,\ 11]$.

The spectrum and the comparison between the errors bound are shown in Figure 1.

From Figure 1, we can observe that the error bound in Eq. (15) is sharper than in Eq. (14). In fact, it can even be used as an estimator of the error of high polynomial degrees. This behavior is also observed in several other simulations for normal matrices generated using a random number of eigenvalues with a uniform distribution. Moreover, for ellipses not contained in the right half plane, the error bound (14) is not particularly reliable (see Fig. 1d).

These findings provide valuable theoretical insight into Faber polynomials for normal matrices. However, the matrix operator is not necessarily normal in wave propagation cases with absorbing boundary conditions, which will be investigated later on. As a result, the bound (13) cannot be directly applied in such cases.

2.2.2 Faber's polynomials in conics

The performance of Faber polynomials depends on the conics they are defined on. This dependence is very strong, in the sense that different ellipses can lead to an enhancement or deterioration of the error in several orders of magnitude.

[1] We used the python function `ortho_group.rvs` from the `Python`'s package `scipy`

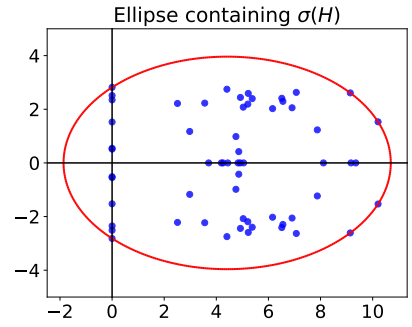

(a) Ellipse of minimum γ containing the $n = 60$ eigenvalues of H.

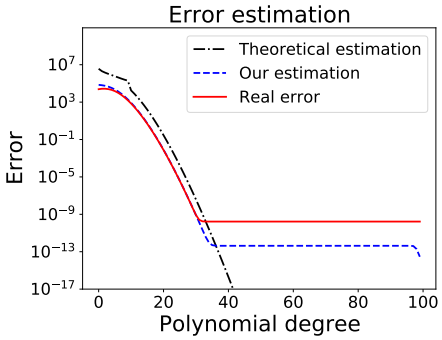

(b) Error bounds for the exponential of matrix H.

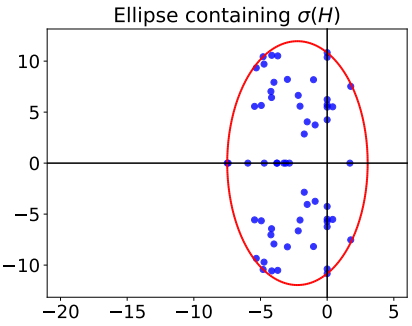

(c) Ellipse of minimum γ containing the $n = 60$ eigenvalues of H.

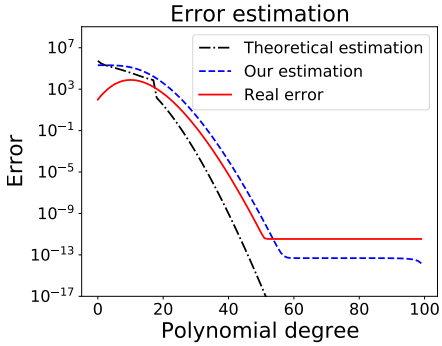

(d) Error bounds for the exponential of matrix H.

Fig. 1: (Upper images) Error estimation of $e^{\boldsymbol{H}}$ for a real normal matrix $\boldsymbol{H}$ with randomly generated eigenvalues on the right half plane. (Lower images) Same as before, but on both half planes. (Right images) The theoretical estimation is based on Bergamaschi and Vianello [6], our approximation is based on inequality (15), and the real error are the effectively calculated errors, subject to rounding errors effects, when approximating the exponential. The bound proposed in this research is sharper than the one reported in the literature.

Therefore, we dedicate this Section to discuss the approximation performance for different types of conics.

The necessity of enclosing $\sigma(\boldsymbol{H})$ within the ellipse $\mathcal{E}(d, c_f, a)$ for the Faber series approximation of matrix functions is not solely a theoretical requirement. Violations of this condition in numerical experiments show considerably worsened solutions. Moreover, opting for an ellipse larger than required results in a deceleration of convergence. In practical terms, this implies that a higher polynomial degree will be needed to attain a certain error by using an ellipse larger than necessary. When contrasted with the optimal ellipse, this approach proves to be less efficient. Fig. 2 depicts the error in an exponential approxi-

mation with respect to the polynomial degree considering ellipses of different sizes.

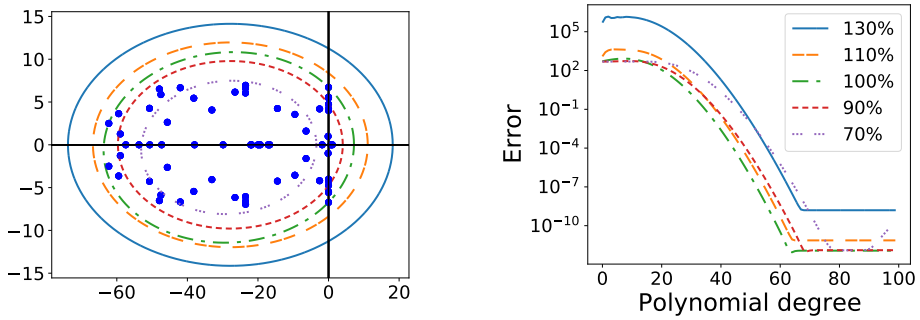

(a) Five ellipses, one optimal (green), four others varying in sizes, and the eigenvalues of a randomly generated normal matrix.

(b) Error of Faber approximation using each of the ellipses on the left to approximate the exponential of the matrix.

Fig. 2: Error of Faber polynomials on the approximation of the exponential of a randomly generated normal matrix by using the optimal ellipse (green), and four other ellipses with varying sizes in a percentage of the optimal ellipse. If the ellipse does not enclose all eigenvalues or if the ellipse is too large, errors can be considerably larger.

As we notice, the best approximation is given by the smallest ellipse that still covers all eigenvalues of the operator. To compute this ellipse, we employed a modified version of the algorithm outlined in Welzl [42] to identify the minimum capacity circle enclosing a finite set of points. As indicated by Welzl [42], the required changes for ellipses are minimal. Upon comparing this ellipse with the largest one, a notable disparity of at least two orders of magnitude in the approximation error becomes apparent. Notably, it appears that employing the 90% ellipse yields a superior approximation compared to the 110% ellipse. This could be because very few eigenvalues are left outside by the 90% ellipse, making the impact of the excluded eigenvalues less pronounced. Nevertheless, this observation is not necessarily true for other numerical examples or polynomial degrees. Should we opt for a higher polynomial degree, such as 200, the approximation linked to the 90% ellipse would diverge, while the approximations using ellipses encompassing all eigenvalues would maintain their convergence. Hence, a good estimation of a small-as-possible convex cover of $\sigma(\boldsymbol{H})$ to construct the ellipse seems to be of utmost importance when dealing with computational efficiency.

From bound (15), we notice that the amplitude of Faber coefficients a_j influences the convergence speed. When they are smaller, the error bound (15) is lower; therefore, a faster convergence may be achieved. The principal constants influencing the magnitude of a_j coefficients are the ellipse capacity

γ, and the ellipse eccentricity c_f. In Fig. 2, we observe that when the capacity of the ellipse increases, the rapidity of the convergence decreases.

Next, we also investigate decreasing the ellipse eccentricity c_f at the cost of increasing the ellipse capacity. Starting from the ellipse with minimum capacity, we construct the optimal ellipses with a predefined c_f, followed by reducing step-by-step c_f with each ellipse until we get a circle ($c_f = 0$).

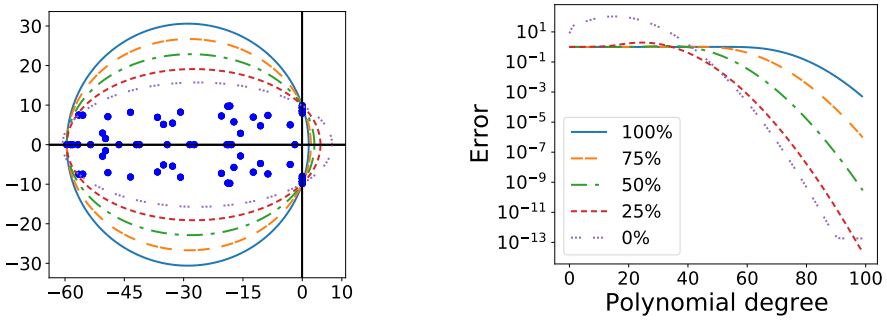

(a) Five ellipses with decreasing c_f and the eigenvalues of a randomly generated normal matrix.

(b) Error of Faber approximation for each of the ellipses on the left.

Fig. 3: Error of Faber polynomials on the approximation of the exponential of a normal matrix by using five different ellipses with decreasing eccentricity. When the eccentricity diminishes, the error is lower for some degrees and higher for others.

Fig. 3 shows the errors of calculating the matrix exponential for each conics using the matrix infinity norm. For low polynomial degrees, the approximations using conics with less eccentricity are better, but the magnitude of the errors is too high to be considered a good approximation. In addition, the ellipse with minimum capacity has the lowest error for high degrees. An interesting observation is that the minimum capacity ellipse exhibits a hump effect (Fig. 3 (b)) that diminishes as we decrease the eccentricity of the ellipse. However, this should not be confused with the hump phenomenon described in [29], relating the approximation error of the exponential matrix with the time step size and the number of time steps. Remarkably, as demonstrated by Figure 4 (b), adopting a circular shape does not necessarily eliminate this phenomenon in all cases.

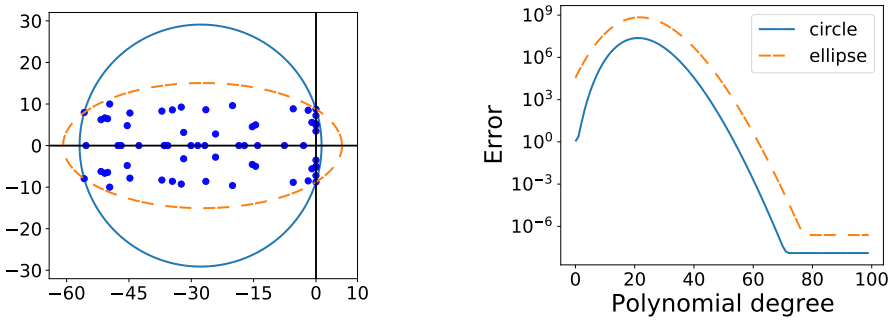

(a) Ellipse and circle used in the Faber exponential approximation.

(b) Error of Faber approximation for ellipse and circle shown on the left.

Fig. 4: Error of Faber polynomials on the approximation of the exponential of a normal matrix by using the optimal ellipse and an optimal circle. In this particular case, a circle with higher capacity outperforms the use of the optimal ellipse.

In general, the conclusion that an ellipse with minimum capacity has the lowest error for high degrees is not always valid. If we have a different distribution of eigenvalues, similar to the ones appearing in the wave equations discussed in the next sections, we may get different relations as illustrated in Fig. 4. As such, a circle can provide a better alternative than an ellipse with minimum capacity under special circumstances. Hence, it is conceivable that other conic shapes might be more suitable for achieving faster convergence, depending on the eigenvalue distribution. Further investigations on the Faber convergence with respect to eccentricity and conic form may be of interest but go beyond the scope of this paper and will be discussed elsewhere. Hence, this paper will only study the method over an ellipse with minimum capacity.

3 Application to seismic waves

This section is dedicated to the mathematical formulations of the wave equations with an absorbing boundary condition, its numerical discretization, and the description of the experiments used in this work. Taking all these different aspects into account is of utmost importance for the Faber approximation since they define the discrete operator, and the exponential method relies on the spectrum of the operator.

3.1 Formulations of the wave equations with PML

The eigenvalue distribution of a discrete operator is strongly influenced by the continuous equations. Therefore, to study the spectrum $\sigma(\boldsymbol{H})$ of the matrix

operator $\boldsymbol{H}$, and the characteristics of the approximation using Faber polynomials, we take different formulations into account to obtain better numerical conclusions. All formulations include the PML absorbing boundary condition, as discussed next.

The PML is one of the most popular absorbing boundary conditions used for the wave equations and related areas [13, 24, 40]. While termed as a boundary condition, it is in fact an extension of the problem to a larger domain, containing an absorbing layer, together with a set of additional variables and equations acting on this layer. It is very effective for most seismic imaging applications, but it is also of relatively complex implementation due to an increase in the number of equations. It is built from a transformation of the real domain to the complex plane, where the waves outside the physical region of interest (PML layers) are attenuated, while the others (inside the physical domain) remain unchanged [4, 5].

For the acoustic wave equations, we have two formulations in one and two dimensions, and they differ in the order of spatial discretization, given as follows.

One dimensional form: ($x \in \Omega = [a_1, a_2]$, $t > t_0$)

$$\frac{\partial}{\partial t}\begin{pmatrix} u \\ v \\ w \end{pmatrix} = \begin{pmatrix} 0 & 1 & 0 \\ c^2\frac{\partial^2}{\partial x^2} & -\beta_x & c^2\frac{\partial}{\partial x} \\ -\beta_x\frac{\partial}{\partial x} & 0 & -\beta_x \end{pmatrix}\begin{pmatrix} u \\ v \\ w \end{pmatrix}\begin{pmatrix} 0 \\ f \\ 0 \end{pmatrix}, \qquad \text{(2SD)} \tag{16}$$

$$\frac{\partial}{\partial t}\begin{pmatrix} u \\ v \\ w \end{pmatrix} = \begin{pmatrix} 0 & c^2\frac{\partial}{\partial x} & -c^2 \\ \frac{\partial}{\partial x} & -\beta_x & 0 \\ 0 & \beta_x\frac{\partial}{\partial x} & -\beta_x \end{pmatrix}\begin{pmatrix} u \\ v \\ w \end{pmatrix} + \begin{pmatrix} \int f \\ 0 \\ 0 \end{pmatrix}. \qquad \text{(1SD)} \tag{17}$$

Two-dimensional form: ($(x, y) \in \Omega = [a_1, a_2] \times [b_1, b_2]$, $t > t_0$)

$$\frac{\partial}{\partial t}\begin{pmatrix} u \\ v \\ w_x \\ w_y \end{pmatrix} = \begin{pmatrix} 0 & 1 & 0 & 0 \\ -\beta_x\beta_y + c^2\left(\frac{\partial^2}{\partial x^2} + \frac{\partial^2}{\partial y^2}\right) & -(\beta_x + \beta_y) & c^2\frac{\partial}{\partial x} & c^2\frac{\partial}{\partial y} \\ (\beta_y - \beta_x)\frac{\partial}{\partial x} & 0 & -\beta_x & 0 \\ (\beta_x - \beta_y)\frac{\partial}{\partial y} & 0 & 0 & -\beta_y \end{pmatrix}\begin{pmatrix} u \\ v \\ w_x \\ w_y \end{pmatrix} + \begin{pmatrix} 0 \\ f \\ 0 \\ 0 \end{pmatrix}, \text{(2SD)} \tag{18}$$

$$\frac{\partial}{\partial t}\begin{pmatrix} u \\ v_x \\ v_y \\ w_x \\ w_y \end{pmatrix} = \begin{pmatrix} 0 & c^2\frac{\partial}{\partial x} & c^2\frac{\partial}{\partial y} & -c^2 & -c^2 \\ \frac{\partial}{\partial x} & -\beta_x & 0 & 0 & 0 \\ \frac{\partial}{\partial y} & 0 & -\beta_y & 0 & 0 \\ 0 & \beta_x\frac{\partial}{\partial x} & 0 & -\beta_x & 0 \\ 0 & 0 & \beta_y\frac{\partial}{\partial y} & 0 & -\beta_y \end{pmatrix}\begin{pmatrix} u \\ v_x \\ v_y \\ w_x \\ w_y \end{pmatrix} + \begin{pmatrix} \int f \\ 0 \\ 0 \\ 0 \\ 0 \end{pmatrix}. \qquad \text{(1SD)} \tag{19}$$

Here, $u = u(t, x)$ (or $u = u(t, x, y)$ in 2D) is the displacement, $c = c(x)$ (or $c = c(x, y)$ in 2D) is the given velocity distribution in the medium, $v =$

$v(t,x)$ (or $(v_x, v_y) = (v_x(t,x,y), v_y(t,x,y))$ in 2D) is the wave velocity, $f = f(x,t)$ (or $f = f(x,y,t)$ in 2D) is the source term, and its time integral $\int f$ is calculated over the interval $[t_0, t]$, where t_0 is the initial time. The w-functions ($w = w(t,x)$ in 1D and $(w_x, w_y) = (w_x(t,x,y), w_y(t,x,y))$ in 2D) are the auxiliary variables of the PML approach and the β-functions are known and control the damping factor in the absorbing layer. The parameters a_1, a_2, b_1, and b_2 are real numbers that define the boundaries of the domain Ω.

The spatial domain is decomposed into two parts: a main physical domain of interest and an outer domain layer surrounding the physical one, used to place the wave-absorbing boundary conditions. On the physical domain (without the PML layer), the β-functions are zero, and the system of equations coincides with the classic wave propagation without absorbing boundary conditions. Therefore, the auxiliary w-functions are different from zero only in the PML domain. On the other hand, since the displacement is attenuated in the PML layer, arbitrary conditions can be set at the boundary of the PML region, where zero-Dirichlet conditions are adopted. The differential equations are then well-defined once the initial conditions are given in conjunction with the Dirichlet (null displacement) outer boundary conditions, see Assi and Cobbold [4].

For the sake of readability, equations, and details for the two-dimensional elastic wave problem are only provided in Appendix A.1, together with a further description of the continuous equations for the acoustic problem.

3.2 Numerical discretization by finite differences

In this Section, we present the basic information about the spatial discretization methods focused on classic finite difference schemes. To ensure an adequate representation of high-frequency waves, we use a staggered grid, representing waves up to frequencies of $2/\Delta x$, improving spatial stability and dispersion properties [41]. Fig. 5 depicts the variable positioning of 1SD equations for two dimensions, employing uniform spacing. Figures for other formulations are provided in App. A.2.

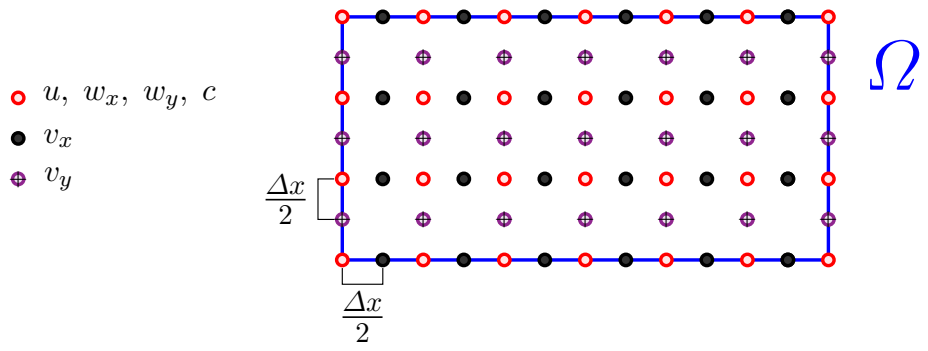

Fig. 5: Uniformly staggered grid in 2D with the relative positions of the (1SD) wave equations variables and parameters. u, w_x, w_y and c are collocated (centered) and v_x, v_y are staggered in the grid.

We use discretizations of fourth and eighth order for the spatial derivatives. Having a high-order spatial discretization relates to a reduction of dispersion effects due to spatial discretizations [27], supporting us to investigate errors in the time domain of exponential integration schemes.

For collocated and staggered variables, in a similar way to [26], we used the expansion in the Taylor series to construct the fourth-order scheme

$$\frac{\partial u_{i+\frac{1}{2}}}{\partial x} \approx \frac{u_{i-1} - 27u_i + 27u_{i+1} - u_{i+2}}{24\Delta x} \tag{20}$$

and the eighth-order scheme

$$\frac{\partial u_{i+\frac{1}{2}}}{\partial x} \approx \frac{1225}{1024\Delta x}\left(u_{i+1} - u_i - \frac{u_{i+2} - u_{i-1}}{15} + \frac{u_{i+3} - u_{i-2}}{125} - \frac{u_{i+4} - u_{i-3}}{1715}\right) \tag{21}$$

with analogous expressions for the y-coordinate in the 2D discretization.

For the points near the outer boundary, we use the same discretization formulas as for the interior points, but with zero-valued functions (Dirichlet Boundary condition) for points outside the domain. After all, if a wave reaches the outer boundary, it will be continuously weakened on its way to the boundary and back to the physical domain, attaining minimal energy.

For the PML thickness δ, and the parameter β_0, Assi and Cobbold [4] proposed a relation between them and the spatial grid space Δx. However, our objective in this paper is not the study of the PML absorbing boundary, but the solution of the wave equations with PML constraints. Therefore, we choose suitable values for δ and β_0, such that δ is small and the wave reflections remain minimal but without numerical errors because of large values of β_0. The values for these parameters and other numerical details are in Appendix A.3.

We continue with a description of various test cases used for further investigation of numerical experiments in one of the following sections.

3.3 Test cases

To construct the operator, we also require the definition of the velocity field and other model parameters. Their description is organized in several numerical experiments for the wave propagation equations with PML used throughout this paper. The numerical tests comprehend scenarios with variable difficulty, changing the dimension of the wave equations, the characteristics of the medium, the initial conditions, and the use of a source term. The general features of the numerical experiments used in the remainder of this work are summarized in Table 1, with further details provided in Appendix A.3. The source term for the test cases consists of a Ricker's wavelet since this is one of the most frequently used source terms in seismic imaging [22].

Test Case ID	**Type**	**Dim**	**Medium**	**Initial cond.**	**Source term**
TC#1	acoustic	1D	homog.	non-zero	-
TC#2	acoustic	1D	heterog.	non-zero	-
TC#3	acoustic	1D	heterog.	zero	yes
TC#4	acoustic	2D	homog.	non-zero	-
TC#5	acoustic	2D	heterog.	non-zero	-
TC#6	acoustic	2D	heterog.	zero	yes
TC#7	elastic	2D	heterog.	zero	yes

Table 1: General features of the numerical experiments: type of equation, problem dimensions, medium heterogeneity (homogeneous or heterogeneous), initial conditions, and the use of Ricker's source term.

The cases TC#1 and TC#4, where the wave is propagated in a *homogeneous* medium *without a source term* in one and two dimensions, are intended to analyze the Faber approximation of the wave equation with PML in a mathematical scenario of lowest complexity. A non-zero initial condition is used in case of no source term.

4 Spectrum of discrete operator

The Faber approximation requires an estimation of the convex hull of the spectrum of the matrix operator to construct the ellipse where the polynomials will be defined. This is a difficult task for the matrix operators derived from the spatial discretization of PDE systems, where the analytical expression of the eigenvalues is not generally known. Since the matrix dimensions can be very large, the computational time to compute the eigenvalues can be inadequate for practical applications. In addition, when solving PDEs numerically, variations in the parameters of the equations often produce significant changes in the spectrum of the discrete operator. This is the case in seismic imaging for the

wave equations with PML, where the velocity field is constantly modified when solving the inverse problem.

Based on empirical results produced by the numerical considerations and the test experiments of the previous section, we propose an estimate of the spectrum of the discrete operator $\boldsymbol{H}$. We start by studying the eigenvalue distribution of a lower-resolution discrete wave equations operator for which a computation of eigenvalues is possible. By doing so, we aim for sharp bounds of the $\boldsymbol{H}$ operator spectrum $\sigma(\boldsymbol{H})$ for the construction of the optimal ellipse, which can be generalized to high-resolution discretizations.

4.1 General properties

We study the spectrum of $\boldsymbol{H}$ by calculating all of its eigenvalues for a finite decreasing sequence of Δx, utilizing the `eigs` function from the `Scipy` Python package. Different distributions of eigenvalues on the complex plane for a 4th-order spatial discretization with 1SD formulation are given in Figure 6. When $\Delta x \to 0$, the convex hull of $\sigma(\boldsymbol{H})$ tends to a rectangle with sides parallel to the real axis. Thus, finding a relation between the rectangle sides and Δx provides an estimator of the convex hull of $\sigma(\boldsymbol{H})$ for small Δx.

We also notice from Fig. 6 that $\sigma(\boldsymbol{H})$ is symmetric with respect to the real axis. Since H is a real matrix, it is straightforward to verify that if $\zeta \in \sigma(\boldsymbol{H})$, then $\overline{\zeta} \in \sigma(\boldsymbol{H})$. Consequently, it is sufficient to only investigate the eigenvalues with non-negative imaginary parts. Moreover, Fig. 6 indicates that the limits of the rectangle on the imaginary limit seem to relate linearly to $1/\Delta x$. At the same time, for the real part, there is apparently a constant negative limit on the left side, $-\beta_0$, for the PML parameter $\beta_0 > 0$, and zero on the right. The spectral distribution for the 2SD formulation is given in Appendix A.4.

These bounds for the real axis agree with the theoretical bounds for the continuous spectrum of the wave equations with PML conditions. For instance, performing a Fourier analysis of the eigenvalues of the continuum operator H of the (1SD) formulation (Eq. (17)), in a unitary spatial domain ($[0, 1]$), using

$$(u,\ v,\ w)^T = \sum_{k=-\infty}^{\infty} (A_k,\ B_k,\ C_k)^T e^{ikx}, \tag{22}$$

and considering the linear map of the continuum operator H on each term, we obtain the symbol of the operator H [39] as

$$\mathsf{H} \begin{pmatrix} A_k \\ B_k \\ C_k \end{pmatrix} e^{ikx} = \begin{pmatrix} 0 & c^2 ik & -c^2 \\ ik & -\beta_x(x) & 0 \\ 0 & \beta_x(x) ik & -\beta_x(x) \end{pmatrix} \begin{pmatrix} A_k \\ B_k \\ C_k \end{pmatrix} e^{ikx}. \tag{23}$$

Now, the eigenvalues of the operator symbol are given by

$$\lambda_0 = 0,\ \lambda_{1,2} = -\beta_x(x) \pm ick. \tag{24}$$

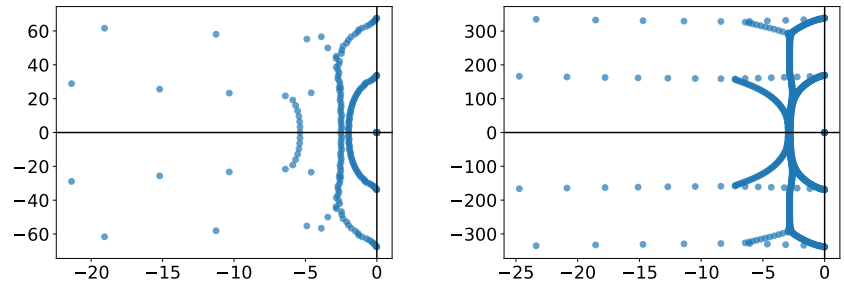

(a) $\Delta x = 0.105$

(b) $\Delta x = 0.021$

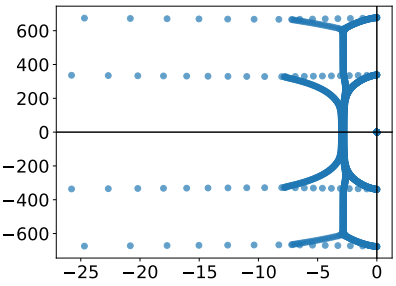

(c) $\Delta x = 0.0105$

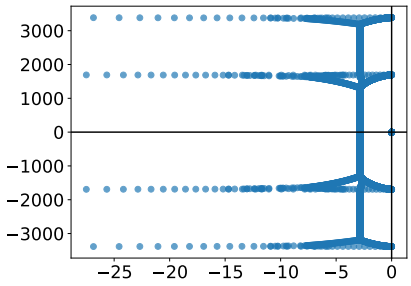

(d) $\Delta x = 0.0021$

Fig. 6: Eigenvalues on the complex plane (using coordinates $(Re(\lambda), Im(\lambda))$) using a fourth-order spatial discretization of the acoustic wave equation in one dimension, with formulation 2SD, considering TC#3, for $\Delta x = \{0.105, 0.021, 0.0105, 0.0021\}$. For each Δx, the spectrum has a rectangular-shaped convex hull.

Therefore, if the wave number k is constrained within $[-\frac{1}{\Delta x}, \frac{1}{\Delta x}]$, as it is the case for discrete representations of the domain, the bounds of $\sigma(\mathsf{H})$ on the complex plane are given by $[-\beta_{\max}, 0] \times [-\frac{c_{\max}}{\Delta x}, \frac{c_{\max}}{\Delta x}]$, where $c_{\max}$ is the maximum velocity in the medium and $\beta_{\max}$ is the maximum of $\beta_x(x)$. So, we have a linear relation of the imaginary limits of the axis with respect to $\frac{1}{\Delta x}$, and the real part is within the interval $[-\beta_{\max}, 0]$, where

$$\beta_{\max} = \beta_0 \left(\frac{\delta - \Delta x/2}{\delta} \right)^2, \tag{25}$$

where β_0 and δ are PML parameters.

It is worth noting that while we have exclusively presented the complete spectrum for the particular instance of the 4th-order spatial discretization and TC#3, the preceding analysis remains valid for the other test cases. This holds whether they involve a 4th or 8th-order spatial discretization, span one

or two dimensions, or pertain to different equation formulations. The omission of these plots is only for the sake of brevity.

In the next two subsections, we will examine the dependency of the imaginary and real limits of the eigenvalues on the problem variables. While the presented numerical examples focus on acoustic cases, it is pertinent to highlight that these findings also hold for the elastic formulation in TC#7 (see Appendix A.4).

4.2 Estimation of the imaginary limit

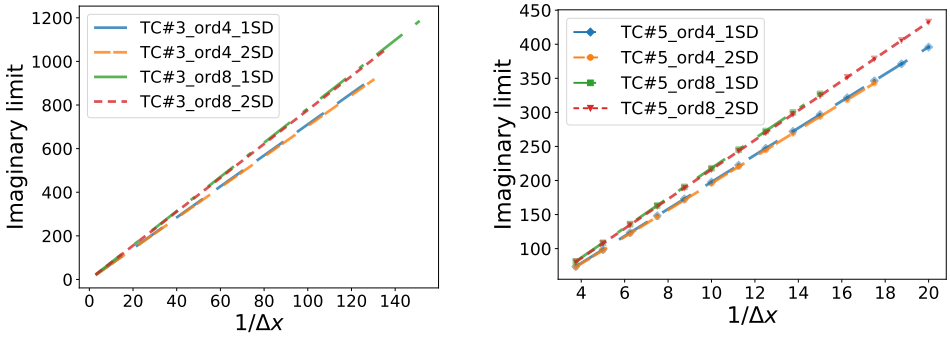

(a) TC#3, in 1D, acoustic.

(b) TC#5, in 2D, acoustic.

Fig. 7: Maximum imaginary parts of the eigenvalues of $\sigma(\boldsymbol{H})$ for varying $1/\Delta x$. The plot indicates a linear relation between the maximum imaginary part of the eigenvalues and $1/\Delta x$.

We perform experiments varying the resolution and other parameters to empirically validate the linear relation between the maximum imaginary part of $\sigma(\boldsymbol{H})$ and $1/\Delta x$. These parameters include the medium velocity field, equation formulation, and discretization order. The results of these experiments are presented in Figure 7. The linear relations are clear in all experiments performed, with slope variations, due to the different maximum velocities (from different test cases) and discretization orders, in agreement with the expected theory discussed in Sec 4.1. However, we do not notice dependence on the model formulation (1SD or 2SD). The dependency on the model velocity is more clearly shown in the right panel of Fig. 8. In this case, the imaginary limit is connected linearly with the maximum medium velocity $c_{\max}$. The velocities $c_{\max}$ are the same for TC#2 and TC#3, but differ by a factor of two with respect to $c_{\max}$ of TC#1. This relation is also reflected by the imaginary limits of their respective operator spectrum, where the slope of the curves are 7.84 (for TC#2 and TC#3, which have maximum velocity given by $c_{\max} = 3.048$) and 3.92 (for TC#1, with maximum velocity $c_{\max} = 1.524$), approximately.

Next, we investigate the influence of the PML parameters, with results in the left image of Fig. 8. We can observe a superposition of the three lines, indicating a lack of dependence on the PML parameters. This was also observed for other test cases and parameter choices (not shown).

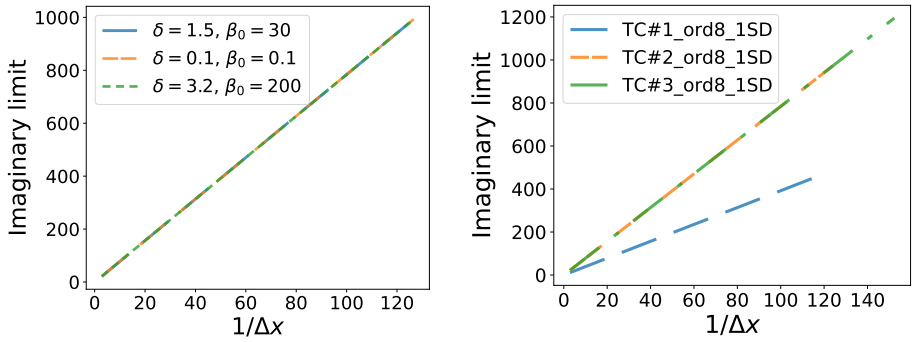

(a) PML parameter variations of TC#3.

(b) Velocity field variations.

Fig. 8: Maximum imaginary parts of the eigenvalues of $\sigma(\boldsymbol{H})$ for varying Δx. (Left figure) Varying PML parameters δ and β_0. Variations of the PML parameters do not affect the maximum imaginary part of the discrete operator. (Right figure) Different velocity fields (test cases). If the maximum velocity $c_{\max}$ does not change, the maximum imaginary parts remain unaltered.

In summary, the specific slope of each curve is primarily influenced by the maximum medium velocity $c_{\max}$, followed by the dimension of the problem, the spatial discretization scheme, and finally, the formulation of the equations (for the acoustic case). Therefore, the linear relationship between the maximum imaginary eigenvalue and $1/\Delta x$ allows determining the maximum imaginary eigenvalue for high-resolution discretizations based on an eigenvalue computation on a low-resolution discretization.

4.3 Estimation of the real limit

Next, we compare the theoretical lower bound of the real part of the eigenvalues given by Eq. (25) with different test cases with results given in Fig. 9, where we vary Δx, and use different dimensions, formulations, spatial discretizations, and equations parameters.

We observe that our estimate provides an adequate lower bound for the 1D problems (left image of Fig. 9). However, this estimate lacks the sharpness exhibited in the 2D example TC#5 or the elastic formulation (as presented in Appendix A.4).

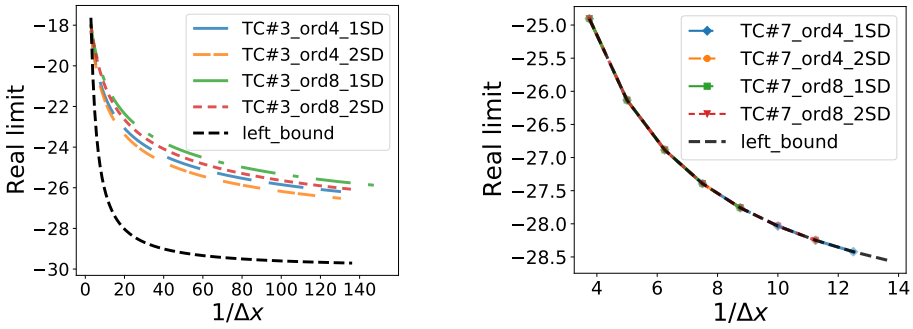

(a) TC#3, in 1D, acoustic.

(b) TC#5, in 2D, acoustic.

Fig. 9: Lower bound of the real part of the eigenvalues for varying Δx, for 1SD, 2SD and elastic formulations, different dimensions, and experimental sets. The dashed line is our estimated lower bound given by Eq. (25).

We observe very good matches for the 2D problems (middle and right image), providing a sharp lower bound.

Concerning the upper bound, we observed that the limit slightly depends on the particular model formulation (not shown), but always results in zero, or a value close to zero. The right limit is zero for the acoustic 1SD formulation and the elastic equations in all the experiments.

Overall, we have found a bound for the real part that only depends on the PML parameters and is independent of the velocity field, the equation formulation, and the spatial discretization scheme.

4.4 Construction of enclosing rectangle

We close this Section with some final remarks on the overall construction of the rectangle enclosing the spectrum $\sigma(\boldsymbol{H})$. For the imaginary limit, we can use the linearity between the maximum imaginary part of the spectrum and Δx, where the linear relation can be estimated with an eigenvalue computation on a sufficiently low-resolution discretization. For the real part, we found an explicit lower bound, based on Eq. (25), and an upper bound of zero. Finally, we can determine the enclosing rectangle, which will be the basis for constructing the optimal ellipse with the Faber polynomials.

We would also like to highlight that estimating the spectrum is important for other time integration methods, such as the explicit exponential integrator based on the Leja points [8, 10]. In contrast to the Faber exponential integrator, which employs the Faber series for the matrix function expansion, the Leja approximation utilizes a basis of interpolating polynomials at specific points called Leja points. When the method is defined within an ellipse encompassing the eigenvalues of $\boldsymbol{H}$, it is stated in [10] that the approximation error is akin

to the second term in Eq. (14). Hence, the development of optimal ellipses could potentially find application in the interpolation polynomials of the Leja points as well.

5 Fourier's stability and dispersion results

Next, we investigate two fundamentally important properties. First, the numerical stability using a von Neumann approach in the next subsection and, after this, the numerical dispersion, considered highly relevant in seismic imaging [22, 40]. We analyze both aspects for several degrees of Faber polynomials separately, aiming to define and compute optimal criteria.

5.1 Von Neumann stability analysis

In this Section, we investigate the stability with Faber polynomials and estimate the CFL number (c_{CFL}) for each polynomial degree by performing a classical von Neumann analysis. We start by replacing the absorbing boundary conditions with periodic ones and drop the source term. This reduces the equations to solve a purely hyperbolic system (purely oscillatory, e.g., [15]). We also assume a constant velocity profile (homogenous medium). When expressed in the Fourier series, the solution is given by

$$U(t,x) = \sum_{m=0}^{M} \begin{pmatrix} A_m(t)e^{ik_m x} \\ B_m(t)e^{ik_m x} \end{pmatrix}, \tag{26}$$

where M is the number of frequencies considered in the solution, k_m are the wave numbers, and the terms in the first and second rows stand for the solutions in the u and v variables (see Eqs. (16)-(17)), respectively. This particular form of the linear wave equations allows an analysis of each spectral mode (A_m, B_m) separately. Then, depending on the spatial scheme and formulation used, there will be a different matrix operator $\boldsymbol{G}$ known as amplification matrix (or stability function for this particular mode), such that

$$\begin{pmatrix} A_m(t_{n+1})e^{ikx_i} \\ B_m(t_{n+1})e^{ikx_{i+1/2}} \end{pmatrix} = \boldsymbol{G} \begin{pmatrix} A_m(t_n)e^{ikx_i} \\ B_m(t_n)e^{ikx_{i+1/2}} \end{pmatrix}. \tag{27}$$

For the 1SD system, the amplification matrix $\boldsymbol{G}$ of Faber polynomial methods may be written as

$$\boldsymbol{G} = \sum_{j=0}^{m} a_j(\Delta t\boldsymbol{H})\boldsymbol{F}_j(\Delta t\boldsymbol{H}), \tag{28}$$

where $\boldsymbol{H}$ is the right-hand side operator of equations formulation 1SD (see Eq. (17)), but without the PML term, and the coefficients a_j are determined by Eq. (11). As an intermediate step preceding the utilization of Eq. (28), we

first delve into the application of $\Delta t\boldsymbol{H}$—a fundamental basic building block of the polynomial approximations employed in this context.

In what follows, we provide an example of a spatial fourth-order finite-difference approximation (20), where we obtain

$$\begin{aligned}\Delta t\boldsymbol{H}\begin{pmatrix}A_m(t)e^{ikx}\\ B_m(t)e^{(i+1/2)kx}\end{pmatrix} &= \frac{\Delta t}{24\Delta x}\begin{pmatrix}0 & c^2g_1\\ g_2 & 0\end{pmatrix}\begin{pmatrix}A_m(t)e^{ikx}\\ B_m(t)e^{(i+1/2)kx}\end{pmatrix}\\ &= \frac{\alpha}{24}\begin{pmatrix}0 & cg_1\\ \frac{1}{c}g_2 & 0\end{pmatrix}\begin{pmatrix}A_m(t)e^{ikx}\\ B_m(t)e^{(i+1/2)kx},\end{pmatrix}\end{aligned}$$

where

$$\alpha = \frac{c\Delta t}{\Delta x}, \quad \theta = k\Delta x \in [0,\pi], \tag{29}$$

$$g_1 = e^{-2i\theta} - e^{i\theta} + 27(1 - e^{-i\theta}) \tag{30}$$

$$g_2 = e^{-i\theta} - e^{2i\theta} + 27(e^{i\theta} - 1), \tag{31}$$

and we are considering the wavenumber $k \in [0, \pi/\Delta x]$. This leads to the representation of $\Delta t\boldsymbol{H}$

$$\Delta t\boldsymbol{H} = \frac{\alpha}{24}\begin{pmatrix}0 & g_1\\ g_2 & 0\end{pmatrix}, \tag{32}$$

which also holds for other spatial discretization orders, but in other cases, we may have different g_1 and g_2 values.

Given this form, we build the operator $\boldsymbol{G}$ by substituting (32) into expression (28). For the operators derived from the other formulations, spatial schemes, and dimensions, the reader can refer to Section A.5.

Next, we compute the CFL number (c_{CFL}) as the largest α so that the spectral radius $\rho(\boldsymbol{G})$ is at most $1+\epsilon$, with $\epsilon = 10^{-7}$ accounting for round-off errors. We compute this CFL number for several polynomial degrees and different numerical specifications with results shown in the upper row of Fig. 10. We observe that for the acoustic equations, the spatial discretization and equation formulations considered have little influence on the stability of the method. Yet, this is not the case for the elastic equations, and an important gain is observed when the spatial discretization order is increased. Overall, there is a small improvement in the performance using 2SD equations instead of 1SD, and the passing from 1D to 2D reduces the values of c_{CFL}. This reduction is partly because, in two dimensions, the CFL number is divided by a factor of a square root of two. Moreover, in all scenarios, the CFL number is enhanced with the increase in polynomial degrees.

Furthermore, we use the MVOs as a reference for computational cost and define

$$\mathrm{N}_{\mathrm{op}}^{\mathrm{CFL}} = \frac{\#\ \mathrm{MVOs}}{c_{\mathrm{CFL}}}, \tag{33}$$

representing the ratio between the computational requirements and a value relating to the CFL. Hence, this scalar value represents the computational efficiency, where smaller values relate to better efficiency. Since the number of

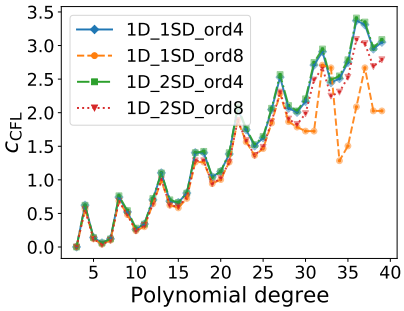

(a) CFL number for one dimension, acoustic.

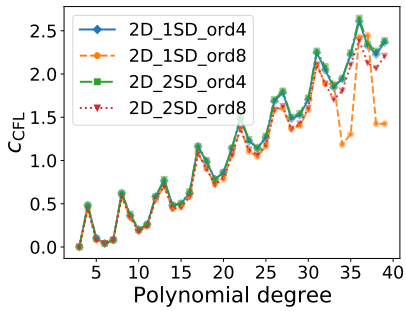

(b) CFL number for two dimensions, acoustic.

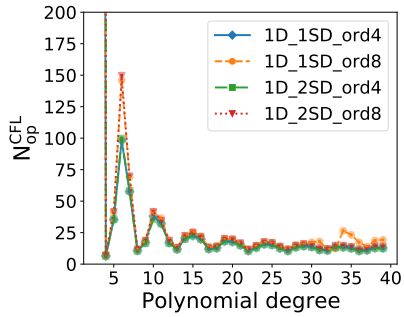

(c) N_{op}^{CFL} number for one dimension, acoustic.

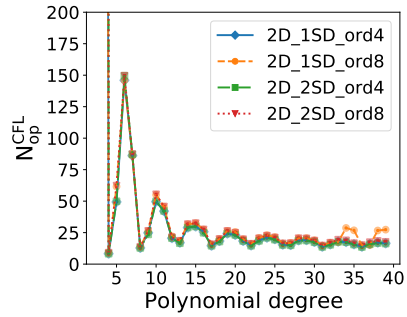

(d) N_{op}^{CFL} number for one dimension, acoustic.

Fig. 10: Stability graphics of the Faber approximation method for different spatial discretizations, dimensions, 1SD and 2SD formulations, and polynomial degrees $m = \{3, 4, ..., 40\}$. The CFL number (top row), and the measure of the operations number of Eq. (33) (bottom row). Higher polynomial degrees imply larger c_{CFL}, but this does not necessarily result in a decrease in computations, owing to the oscillations.

MVOs coincides with the polynomial degree used in the approximation, for the graphics, we will use polynomial degrees instead of MVOs with results given in Fig. 10. The oscillatory behavior indicates that higher polynomial degrees are not reflected by fewer computations, but rather some particular degrees are more fitted to improve the values of N_{op}^{CFL}. The oscillations of the curves have a periodicity of four and five degrees, which we account for by relating it to some sort of symmetry of the complex polynomials $\boldsymbol{F}_j$. The results for the elastic equations correspond to those discussed in this section and can be found in the Appendix (Section A.5).

5.2 Numerical dispersion

We continue studying the dispersion (R) given by the quotient between the velocity of the numerical solution c_{num} and the real wave velocity c, hence

$$R = \frac{c_{\text{num}}}{c} = \frac{w_{\text{num}}}{k\,c}, \tag{34}$$

where w_{num} is the numerical angular frequency, and k is the wavenumber. Ideally, a method with no spurious numerical dispersion should have $R = 1$. Therefore, we define the dispersion error as $|R - 1|$.

In Equation (34), the velocity c is known, k is any wavenumber value contained in the interval $[0, \pi/\Delta x]$, and w_{num} is calculated from the phase of the eigenvalues of $\boldsymbol{G}$.

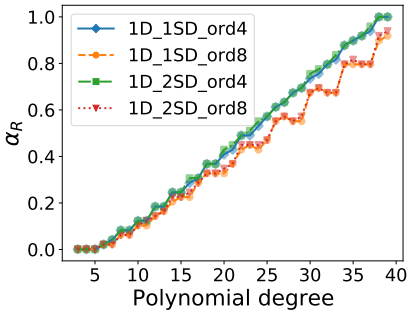

(a) Dispersion number, α_R, for one dimension, acoustic.

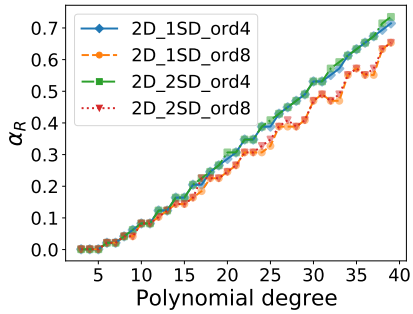

(b) Dispersion number, α_R, for two dimensions, acoustic.

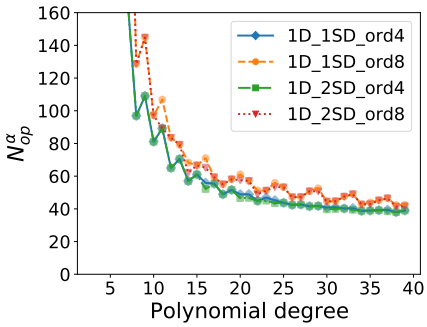

(c) N^{α}_{op} number for one dimension, acoustic.

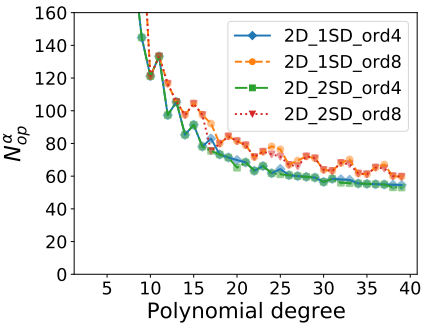

(d) N^{α}_{op} number for two dimension, acoustic.

Fig. 11: Dispersion studies of Faber approximation method using different spatial discretizations, dimensions, equations formulations, and polynomial degrees $m = \{3, 4, ..., 40\}$. Higher polynomial degrees imply larger α_R and a non-monotonous decrease in the number of operations.

Now, we introduce α_R, similar to the c_{CFL} number, but relating to a maximum dispersion error instead. We define α_R to be the maximum α (see Eq. (29)) such that the dispersion error is less than $\epsilon_R = 10^{-5}$, which is set to be the required dispersion accuracy. We can then compute the computational efficiency with respect to dispersion by using

$$\mathrm{N}_{\mathrm{op}}^{\alpha} = \frac{\#\ \mathrm{MVOs}}{\alpha_R}. \tag{35}$$

Results are presented in Fig. 11, using 1SD and 2SD formulations in one and two dimensions, with different spatial discretization orders.

From Fig. 11, we observe that the α_R in 1D is larger than in the 2D case, and the dispersion changes very little with respect to the spatial discretization order. For the elastic equations, α_R decreases even more, and there is only a small difference between the spatial discretization order. Moreover, in agreement with the stability analysis, increasing the polynomial degree leads to larger α_R. However, in contrast with the results on stability, there is a stronger impact on the equation formulation, and higher polynomial degrees imply fewer computations. This agrees with the expected behavior since larger polynomial degrees allow larger time steps, diminishing the number of time steps needed for the computations and, then, reducing the dispersion error.

6 Convergence and efficiency

In this section, we address the numerical convergence and computational efficiency of Faber polynomial approximations for the full equation sets on the limited area domain with the PML absorbing conditions. Due to the complexity of the equations, the analysis is purely numerical, relying on the test cases shown in Section 3.3. To ensure the robustness of the results, and as explained in Section 3.3, the seven experiments vary in levels of complexity and problem specifications. Then, we assess the convergence of the experiments, using the approximation error in L_2, computed for a wide range of Faber polynomial degrees and time-step sizes Δt.

To approximate the solutions using Faber polynomials, we define a spatial step size $\Delta x = 0.0025$ for the 1D examples and $\Delta x = 0.02$ for the 2D examples and use a finite difference scheme with 4th and 8th spatial order. For comparison purposes, we use a nine-stage seventh-order temporal Runge-Kutta scheme RK(9,7) recommended for hyperbolic problems (see Calvo et al. [11])) with a small time-step size ($\Delta t = \Delta x/(8c_{\max})$), where $c_{\max}$ is the maximum velocity. The formulas of the RK(9-7) algorithm are presented in Appendix A.6. The equation formulation and spatial discretization size and order used in the RK(9,7) are the same as the one adopted in the Faber approximations, so the spatial operator is exactly the same as the one used in the Faber approximation scheme. Therefore, only temporal effects are visible in the numerical errors shown.

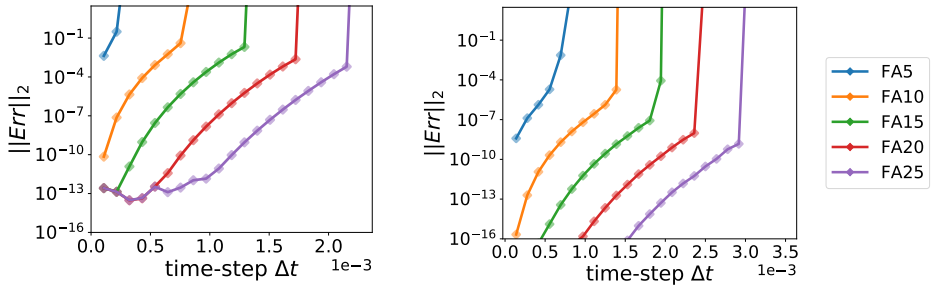

(a) TC#2, in 1D, acoustic, 1SD, spatial order 4.

(b) TC#6, in 2D, acoustic, 2SD, spatial order 4.

Fig. 12: Approximation error of Faber polynomials using 1SD and 2SD formulations, to solve TC#1, TC#6, respectively. The curves represent the error when using polynomials of degrees $m = \{5, 10, \ldots, 25\}$. Increasing the degree of the polynomial allows for larger steps in time while keeping the approximation error smaller than a fixed threshold.

Fig. 12 shows the approximation error for three different examples, with one and two dimensions, using three different formulations and for different spatial approximations order. We observe in all cases that increasing the polynomial degree of the method allows larger stable time-step sizes. This is also demonstrated for the elastic equations (refer to Appendix A.6). If we define a maximum Δt such that the approximation error is bounded by a fixed threshold, we note that the magnitude of this $\Delta t_{\max}$ changes depending on the problem specifications. We also notice that for each polynomial degree, the convergence deteriorates before reaching the critical Δt.

Moreover, we point out that the solution behavior described in Fig. 12 is sustained for other scenarios and is independent of the wave formulation, spatial discretization, and numerical examples considered in this paper. This is due to the fact that larger polynomial degrees relate to higher approximation orders, hence allowing larger time steps.

Next, we further investigate $\Delta t_{\max}$, the maximum time-step size allowed by the polynomials while maintaining an error lower than $\epsilon_{\Delta t} = 10^{-6}$ (see Fig. 13). In (a), we notice that the medium velocity influences $\Delta t_{\max}$, as expected, since the maximum velocity in TC#1 is two times lower than the maximum velocity in TC#3. From the same figure, we also note that even when there is a consistent increase in maximum time-step size, the behavior is not monotonic (TC#1 lines in (a)). Moreover, there are experiments where the equation formulation seems to have no influence on the convergence (SubFig. (a)). Still, there are others where the 2SD formulation seems to perform better than the 1SD (SubFig. (b)). We account for the increased difficulty of the 2D experiments TC#4 and TC#5 when compared to the 1D TC#1 and TC#3. This difference highlights the distinctions between the 1SD and 2SD

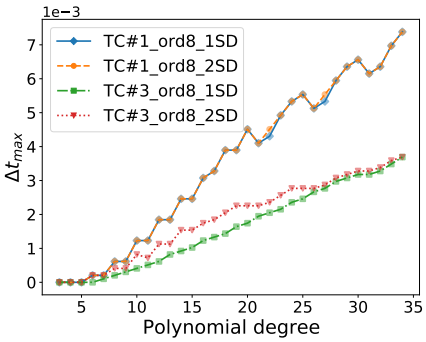

(a) Maximum time step, $\Delta t_{\max}$, for TC#1 and TC#3, using 8th order spatial discretization.

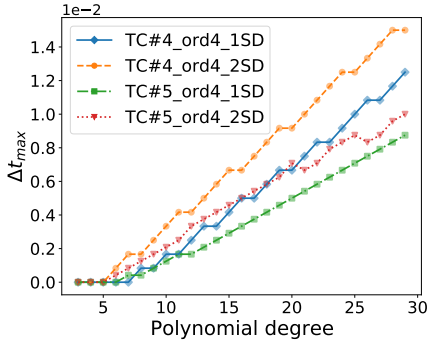

(b) Maximum time step, $\Delta t_{\max}$, for TC#4 and TC#5, using 4th order spatial discretization.

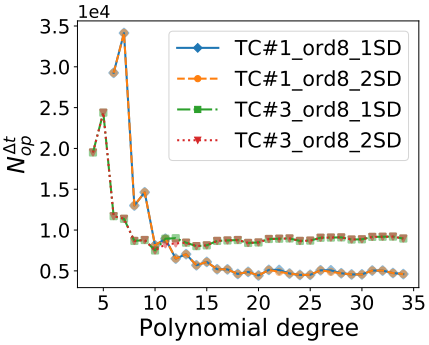

(c) Number of computations, $\mathrm{N}_{\mathrm{op}}^{\Delta t}$, for TC#1 and TC#3, using 8th order spatial discretization.

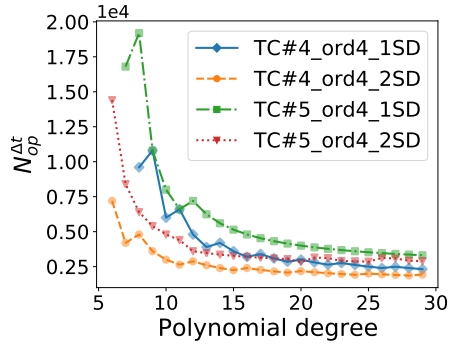

(d) Number of computations, $\mathrm{N}_{\mathrm{op}}^{\Delta t}$, for TC#4 and TC#5, using 8th order spatial discretization.

Fig. 13: Convergence in polynomial order for 1SD and 2SD formulations, using different experimental sets, spatial discretization orders, and a wide range of polynomial degrees. The maximum Δt such that the error of Faber approximations is less than 10^{-6} is shown in the top row. In the bottom row, we show the number of operations using the values of $\Delta t_{\max}$ of the upper line. When the polynomial degree increases, the maximum allowed time-step size also increases, together with a decrease of the number of operations.

formulations. However, further investigation is needed to confirm this hypothesis. In general, we have observed that 2SD always performs similarly or better than 1SD. This suggests the continuum formulation of the wave equation with PML to be an important factor to consider when solving the equations. The situation for the elastic case is comparable, although the discretization order has a lesser impact on the elastic equations (see Appendix A.6).

We again remark that our experiments consider the reference solution to have the same discrete operator as the exponential scheme. Therefore, only

temporal effects are to be noted. Here, we see that the increase in spatial order has only a minor effect of reducing the maximum time step size.

We now define a measure of the number of operations depending on the time step sizes (analogously to Eq. (33) and Eq. (35)) as

$$\mathrm{N}_{\mathrm{op}}^{\Delta t} = \frac{\#\ \mathrm{MVOs}}{\Delta t_{\max}},$$

where again Δt_{max} is the maximum Δt such that the approximation error is bounded by a fixed threshold $\gamma = 10^{-6}$.

In Sections 5.1 and 5.2, we used simplified formulations on periodic domains. Here, we finally consider the full equation sets on the limited area domain with the PML absorbing conditions. Therefore, $N_{\mathrm{op}}^{\Delta t}$ represents a realistic measure of the number of computations by a unit of time.

A general behavior in the number of operations graphics in Fig. 13 is to have a lot of computations for low degree approximations, followed by a declination pattern, and seems to approximate an equilibrium.

The corner model

Although the previous figures of convergence are useful for understanding the approximation error with different setups, they offer little insight into the spatial distribution of the error. Now, we use the TC#5, which has a high velocity contrast heterogeneous medium, to compute the approximation error along a straight line that cuts vertically the space (as shown in Fig. 14 (c)). The Faber solution is calculated with a time-step size Δt, which is $11\times$ larger than the one used in the reference solution and its error is computed for several polynomial degrees.

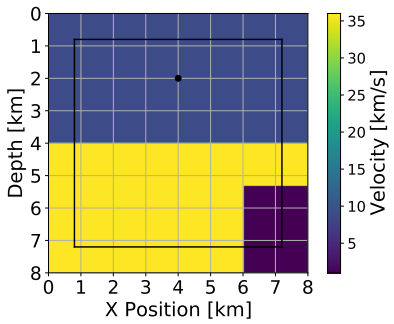

(a) High velocity contrast heterogeneous medium.

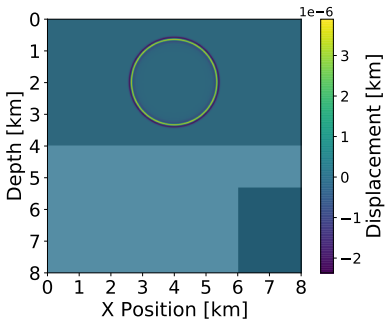

(b) Displacement snapshot at time $t = 0.6s$.

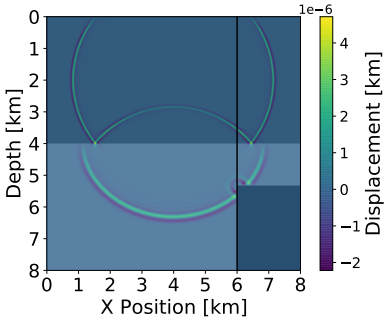

(c) Displacement snapshot at time $t = 1.2s$.

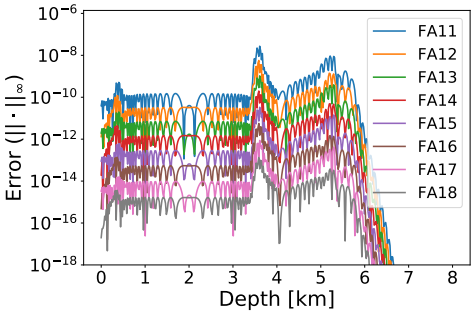

(d) Reference solution at time $t = 1.2s$.

Fig. 14: (Subfigure (a)) Acoustic wave propagation in a heterogeneous medium with a sharp corner. The physical domain is the region enclosed by the black squared contour, the region outside it is the PML domain, and the initial wave explosion arises at the dot black point inside the physical region. (Subfigures (b)-(c)) The reference solution is calculated at the final time and at intermediate time instants. (Subfigure (d)) Approximation errors at the final time $t = 1.3$ for several degrees of Faber polynomials $m = \{10, \ldots, 18\}$ over the black vertical line in Subfigure (c). When the degree of the polynomial increases, the error calculated over the black line in Subfigure (c) diminishes by several orders of magnitude (Subfigure (d)).

Fig. 14 is composed of the velocity field of TC#5, two wave propagation snap-shoots for different time instants, and Subfigure (d) showing the spatial error for different polynomial degrees over the line drawn in Subfigure (c). If the reference solution was to be calculated with the same Δt as the one used in the Faber approximations, it would not have converged to the solution. The same applies to the Faber polynomials with degrees lower than 11. However, for the polynomials of degrees higher than 10, we observe that the error decreases almost an order of magnitude for each degree increment. Therefore, at least

for this particular experiment, when using the large fixed Δt, increasing the approximation order results in a reduction of one order in the numerical error. We again highlight that the dominant error shown here is the temporal one, since our reference solution uses the same discrete operator as the exponential scheme. The peaks of the errors illustrated in Figure 14 (d), occurring within the depth intervals of (3km, 4km) and (5km, 6km), are a result of the presence of front waves at the time $t = 1.2s$ within those particular intervals.

We found that the numerical experiments agree with the theoretical analysis of stability and dispersion. For higher polynomial degrees, we have a larger CFL number, which translates into larger time-step sizes, such that high accuracy solution can be achieved with large time-step sizes.

7 Discussion, contributions & outlook

Faber's polynomials provide a way to generalize exponential integration based on Chebyshev polynomials to non-symmetric or non-antisymmetric matrices. In the present work, we have developed sharper bounds of Faber approximations for normal matrices and a discussion about the importance of the conics used in the construction of the method. We showed that these conics are of utmost importance to ensure a fast convergence of the polynomial approximation. Furthermore, if the conics do not encompass the spectrum of the operator, the convergence of the approximation is not assured.

We provided explicit bounds of the convex hull of the spectrum using different scenarios with respect to continuous model formulation and discretization schemes for the acoustic and elastic wave operators with the popular PML absorbing boundaries. These estimates remove the necessity of computing the eigenvalues of the full operator matrix, requiring only a calibration about the growth of the imaginary part with large Δx for only one velocity model. In this manner, we can predefine the spectrum ranges of the discrete operator using a simplified velocity model, leading to substantial computational savings during the wave inversion process. This is particularly important since the wave inversion involves solving multiple wave propagation scenarios with varying velocity configurations. It is worth recalling that the computation of discretized operators for partial differential equations remains a persistent challenge. This is the reason why in previous research (e.g. [7, 23]) computational algorithms were necessary to calculate the eigenvalues. In the context of the wave equation with absorbing boundary conditions, there is the work of Alonso-Mallo and Portillo [3], predominantly centered around the influence of the real part limits of the eigenvalues of the discretized operator. However, this specific aspect is closely tied to the boundary conditions, and the treatment of the PML was not investigated. A promising approach in this direction is the generalized local Toeplitz sequences. These have been applied in selected cases to derive closed-form expressions that offer precise approximations of eigenvalues [12, 17].

Furthermore, we studied the stability, dispersion error, numerical convergence, and computational cost for the Faber approximation utilizing polynomial orders ranging from 3 up to 30 (and in certain examples, up to 35 or 40). Exploring diverse scenarios involving various wave equation formulations with distinct PML parameters, spatial discretization orders, and dimensions. We observed relatively small differences between distinct formulations of the continuum operator. In particular, we observed that 2SD performs better than the other formulation. This suggests that the choice of an adequate formulation could improve even more the performance of Faber approximation. We also found that increasing the order of the approximation implies a larger CFL number, and the solution calculated for larger time steps maintains high accuracy. Due to the high order expansion of the source term (integral of Eq. (2)), we also note that these results of large time step sizes are not affected by time-frequency sampling issues of the source term. Moreover, from the computational efficiency results, we conclude that, at least for the Faber polynomials applied to seismic waves, the increase in the polynomial degrees is also computationally more efficient than using lower-order polynomials. We assume this could lead to real improvements in seismic imaging, where low dispersion errors are extremely important and very demanding on computational resources. Nonetheless, determining the optimal polynomial degree in general scenarios for the Faber exponential integrators is an unresolved challenge. Potential strategies to advance in this direction include studying numerical tests to understand the behavior of the approximation error and propose sharp bounds, as discussed in Section 2.2.1. In this context, we consider our research to contribute to this subject.

In future research, we intend to work on the open problem of Section 2.2.2 and explore the conics that grant the fastest convergence for Faber polynomials. Additionally, further investigation is required to prove the convergence of the spectra of the discrete operators to the continuum operators, as has been done for the Schrödinger equations in Nakamura and Tadano [32]. This would theoretically predict the asymptotic behavior of the discrete operator's eigenvalues when Δx tends to zero.

We plan a follow-up work on comparing the Faber polynomial exponential scheme with other exponential integrators and several classic methods in the context of wave propagation equations and realistic seismic wave problems.

Acknowledgements This research was carried out in association with the ongoing R&D project registered as ANP20714-2 STMI - Software Technologies for Modelling and Inversion, with applications in seismic imaging (USP/Shell Brasil/ANP). It was funded in part by the Coordenação de Aperfeiçoamento de Pessoal de Nível Superior - Brasil (CAPES) - Finance Code 001, and in part by Conselho Nacional de Desenvolvimento Científico e Tecnológico (CNPq) - Brasil. Fundação de Amparo à Pesquisa do Estado de São Paulo (FAPESP) grant 2021/06176-0 is also acknowledged. It has also partially received funding from the Federal Ministry of Education and Research and the European High-Performance Computing Joint Undertaking (JU) under grant agreement No 955701, Time-X. The JU receives support from the European Union's Horizon 2020 research and innovation programme and Belgium, France, Germany, Switzerland.

Data Avaliability All the data used in the paper was synthetically generated, following the instructions on the paper. The data and the methods codes are available in the git-hub link https://github.com/fernanvr/Faber_1D_2D.

Competing Interests The authors have no relevant financial or non-financial interests to disclose.

References

1. Al-Mohy AH, Higham NJ (2010) A new scaling and squaring algorithm for the matrix exponential. SIAM Journal on Matrix Analysis and Applications 31(3):970–989
2. Al-Mohy AH, Higham NJ (2011) Computing the action of the matrix exponential, with an application to exponential integrators. SIAM journal on scientific computing 33(2):488–511
3. Alonso-Mallo I, Portillo AM (2015) Absorbing boundary conditions and geometric integration: A case study for the wave equation. Mathematics and Computers in Simulation 111:1–16
4. Assi H, Cobbold RS (2017) Compact second-order time-domain perfectly matched layer formulation for elastic wave propagation in two dimensions. Mathematics and Mechanics of Solids 22(1):20–37
5. Berenger JP (1994) A perfectly matched layer for the absorption of electromagnetic waves. Journal of computational physics 114(2):185–200
6. Bergamaschi L, Vianello M (2000) Efficient computation of the exponential operator for large, sparse, symmetric matrices. Numerical linear algebra with applications 7(1):27–45
7. Bergamaschi L, Caliari M, Vianello M (2003) Efficient approximation of the exponential operator for discrete 2d advection–diffusion problems. Numerical linear algebra with applications 10(3):271–289
8. Bergamaschi L, Caliari M, Vianello M (2004) The relpm exponential integrator for fe discretizations of advection-diffusion equations. In: International Conference on Computational Science, Springer, pp 434–442
9. Brachet M, Debreu L, Eldred C (2022) Comparison of exponential integrators and traditional time integration schemes for the shallow water equations. Applied Numerical Mathematics
10. Caliari M, Vianello M, Bergamaschi L (2004) Interpolating discrete advection–diffusion propagators at leja sequences. Journal of Computational and Applied Mathematics 172(1):79–99
11. Calvo M, Franco J, Montijano J, Rández L (1996) Explicit runge-kutta methods for initial value problems with oscillating solutions. Journal of computational and applied mathematics 76(1-2):195–212
12. Capizzano SS (2003) Generalized locally toeplitz sequences: spectral analysis and applications to discretized partial differential equations. Linear Algebra and its Applications 366:371–402

13. Chern A (2019) A reflectionless discrete perfectly matched layer. Journal of Computational Physics 381:91–109
14. Cohen D, Dujardin G (2017) Exponential integrators for nonlinear schrödinger equations with white noise dispersion. Stochastics and Partial Differential Equations: Analysis and Computations 5(4):592–613
15. Cox SM, Matthews PC (2002) Exponential time differencing for stiff systems. Journal of Computational Physics 176(2):430–455
16. Deka PJ, Einkemmer L (2022) Efficient adaptive step size control for exponential integrators. Computers & Mathematics with Applications 123:59–74
17. Garoni C, Serra-Capizzano S, et al. (2017) Generalized locally Toeplitz sequences: theory and applications, vol 1. Springer
18. Gaudreault S, Rainwater G, Tokman M (2021) Kiops: A fast adaptive krylov subspace solver for exponential integrators (vol 372, pg 236, 2018). JOURNAL OF COMPUTATIONAL PHYSICS 441
19. Higham NJ (2005) The scaling and squaring method for the matrix exponential revisited. SIAM Journal on Matrix Analysis and Applications 26(4):1179–1193
20. Hochbruck M, Ostermann A (2010) Exponential integrators. Acta Numerica 19:209–286
21. Huber D, Schreiber M, Schulz M (2021) Graph-based multi-core higher-order time integration of linear autonomous partial differential equations. Journal of Computational Science p 101349, DOI 10.1016/j.jocs.2021.101349
22. Ikelle LT, Amundsen L (2018) Introduction to petroleum seismology. Society of Exploration Geophysicists
23. Jackiewicz Z, Renaut R (2002) A note on stability of pseudospectral methods for wave propagation. Journal of computational and applied mathematics 143(1):127–139
24. Jing H, Chen Y, Wang J, Xue W (2019) A highly efficient time-space-domain optimized method with lax-wendroff type time discretization for the scalar wave equation. Journal of Computational Physics 393:1–28
25. Kole J (2003) Solving seismic wave propagation in elastic media using the matrix exponential approach. Wave Motion 38(4):279–293
26. Leveque R (1998) Finite difference methods for differential equations
27. Liu Y (2013) Globally optimal finite-difference schemes based on least squares. Geophysics 78(4):T113–T132
28. Loffeld J, Tokman M (2013) Comparative performance of exponential, implicit, and explicit integrators for stiff systems of odes. Journal of Computational and Applied Mathematics 241:45–67
29. Moler C, Van Loan C (2003) Nineteen dubious ways to compute the exponential of a matrix, twenty-five years later. SIAM review 45(1):3–49
30. Moret I, Novati P (2001) The computation of functions of matrices by truncated faber series. Numerical Functional Analysis and Optimization
31. Munch NJ (2019) A chebyshev theorem for ellipses in the complex plane. The American Mathematical Monthly 126(5):430–436

32. Nakamura S, Tadano Y (2021) On a continuum limit of discrete schrodinger operators on square lattices. Journal of Spectral Theory 11(1):355–368
33. Niesen J, Wright W (2009) A krylov subspace algorithm for evaluating the φ-functions in exponential integrators. arXiv preprint arXiv:09074631
34. Pototschnig M, Niegemann J, Tkeshelashvili L, Busch K (2009) Time-domain simulations of the nonlinear maxwell equations using operator-exponential methods. IEEE Transactions on Antennas and Propagation 57(2):475–483
35. Ramadan MA, Raslan KR, El Danaf TS, Abd El Salam MA (2017) An exponential chebyshev second kind approximation for solving high-order ordinary differential equations in unbounded domains, with application to dawson's integral. Journal of the Egyptian Mathematical Society 25(2):197–205
36. Schreiber M, Schaeffer N, Loft R (2019) Exponential integrators with parallel-in-time rational approximations for the shallow-water equations on the rotating sphere. Parallel Computing 85:56–65
37. Sidje RB (1998) Expokit: A software package for computing matrix exponentials. ACM Transactions on Mathematical Software (TOMS) 24(1):130–156
38. Starke G, Varga RS (1993) A hybrid arnoldi-faber iterative method for nonsymmetric systems of linear equations. Numerische Mathematik 64(1):213–240
39. Strikwerda JC (2004) Finite difference schemes and partial differential equations. SIAM
40. Tago J, Cruz-Atienza V, Chaljub E, Brossier R, Coutant O, Garambois S, Prieux V, Operto S, Mercerat D, Virieux J, et al. (2012) Modelling seismic wave propagation for geophysical imaging. In: Seismic waves-research and analysis, IntechOpen
41. Wang Y, Liang W, Nashed Z, Li X, Liang G, Yang C (2014) Seismic modeling by optimizing regularized staggered-grid finite-difference operators using a time-space-domain dispersion-relationship-preserving method. Geophysics 79(5):T277–T285
42. Welzl E (2005) Smallest enclosing disks (balls and ellipsoids). In: New Results and New Trends in Computer Science: Graz, Austria, June 20–21, 1991 Proceedings, Springer, pp 359–370
43. Wilcox LC, Stadler G, Burstedde C, Ghattas O (2010) A high-order discontinuous galerkin method for wave propagation through coupled elastic–acoustic media. Journal of Computational Physics 229(24):9373–9396
44. Zhang X, Yang D, Song G (2014) A nearly analytic exponential time difference method for solving 2d seismic wave equations. Earthquake Science 27(1):57–77

A Appendix

A.1 Continuous framework

We formally write the equations formulations, with PML conditions, used throughout the work. For 1D the domain $\Omega = [a_1, a_2]$ is an interval and for 2D $\Omega = [0, a_2] \times [0, b_2]$ is considered a square. The particular values of a_1 and a_2 are fixed in the numerical tests.

One dimensional acoustic waves with PML:

1. Using second order spatial derivatives (2SD)

$$\frac{\partial u}{\partial t}(x,t) = v(x,t), \tag{36}$$

$$\frac{\partial v}{\partial t}(x,t) = -\beta_x(x)v(x,t) + c^2(x)\left(\frac{\partial^2 u}{\partial x^2}(x,t) + \frac{\partial w}{\partial x}(x,t)\right) + f(x,t), \tag{37}$$

$$\frac{\partial w}{\partial t}(x,t) = -\beta_x(x)\left(w(x,t) + \frac{\partial u}{\partial x}(x,t)\right). \tag{38}$$

2. Using only first order spatial derivatives [13] (1SD)

$$\frac{\partial u}{\partial t}(x,t) = c^2(x)\left(\frac{\partial v}{\partial x}(x,t) - w(x,t)\right) + \int_{t_0}^{t} f(x,s)ds, \tag{39}$$

$$\frac{\partial v}{\partial t}(x,t) = -\beta_x(x)v(x,t) + \frac{\partial u}{\partial x}(x,t), \tag{40}$$

$$\frac{\partial w}{\partial t}(x,t) = \beta_x(x)\left(-w(x,t) + \frac{\partial v}{\partial x}(x,t)\right). \tag{41}$$

Two dimension acoustic waves with PML:

1. Using second order spatial derivatives (2SD)

$$\frac{\partial u}{\partial t}(x,y,t) = v(x,y,t), \tag{42}$$

$$\begin{aligned}\frac{\partial v}{\partial t}(x,y,t) = &-\big(\beta_x(x) + \beta_y(y)\big)v(x,y,t) - \beta_x(x)\beta_y(y)u(x,y,t)\\ &+ c^2(x,y)\left(\frac{\partial^2 u}{\partial x^2}(x,y,t) + \frac{\partial^2 u}{\partial y^2}(x,y,t) + \frac{\partial w_x}{\partial x}(x,y,t)\right.\\ &\left.+\frac{\partial w_y}{\partial y}(x,y,t)\right) + f(x,y,t),\end{aligned} \tag{43}$$

$$\frac{\partial w_x}{\partial t}(x,y,t) = -\beta_x(x)w_x(x,y,t) + (\beta_y(y) - \beta_x(x))\frac{\partial u}{\partial x}(x,y,t), \tag{44}$$

$$\frac{\partial w_y}{\partial t}(x,y,t) = -\beta_y(y)w_y(x,y,t) + (\beta_x(x) - \beta_y(y))\frac{\partial u}{\partial y}(x,y,t). \tag{45}$$

2. Using only first order spatial derivatives [13] (1SD)

$$\frac{\partial u}{\partial t}(x,y,t) = c^2(x,y)\Big(\frac{\partial v_x}{\partial x}(x,y,t) + \frac{\partial v_y}{\partial y}(x,y,t) - w_x(x,y,t) - w_y(x,y,t)\Big) + \int_{t_0}^{t} f(x,y,s)ds, \tag{46}$$

$$\frac{\partial v_x}{\partial t}(x,y,t) = -\beta_x(x)v_x(x,y,t) + \frac{\partial u}{\partial x}(x,y,t), \tag{47}$$

$$\frac{\partial v_y}{\partial t}(x,y,t) = -\beta_y(y)v_y(x,y,t) + \frac{\partial u}{\partial y}(x,y,t), \tag{48}$$

$$\frac{\partial w_x}{\partial t}(x,y,t) = \beta_x(x)\left(-w_x(x,y,t) + \frac{\partial v_x}{\partial x}(x,y,t)\right), \tag{49}$$

$$\frac{\partial w_y}{\partial t}(x,y,t) = \beta_y(y)\left(-w_y(x,y,t) + \frac{\partial v_y}{\partial y}(x,y,t)\right). \tag{50}$$

Two-dimensional elastic waves with PML, see Assi and Cobbold [4]:

$$\frac{\partial u_x}{\partial t}(x,y,t) = v_x(x,y,t), \tag{51}$$

$$\frac{\partial u_y}{\partial t}(x,y,t) = v_y(x,y,t), \tag{52}$$

$$\frac{\partial v_x}{\partial t}(x,y,t) = -\big(\beta_x(x)+\beta_y(y)\big)v_x(x,y,t) - \beta_x(x)\beta_y(y)u_x(x,y,t) + \frac{1}{\rho(x,y)}\left[\frac{\partial}{\partial x}\left(T_{xx}(x,y,t)+w_{xx}(x,y,t)\right) + \frac{\partial}{\partial y}\left(T_{xy}(x,y,t)+w_{xy}(x,y,t)\right)\right] + f_x(x,y,t), \tag{53}$$

$$\frac{\partial v_y}{\partial t}(x,y,t) = -\big(\beta_x(x)+\beta_y(y)\big)v_y(x,y,t) - \beta_x(x)\beta_y(y)u_y(x,y,t) + \frac{1}{\rho}\left[\frac{\partial}{\partial x}\left(T_{xy}(x,y,t)+w_{yx}(x,y,t)\right) + \frac{\partial}{\partial y}\left(T_{yy}(x,y,t)+w_{yy}(x,y,t)\right)\right] + f_y(x,y,t), \tag{54}$$

$$\frac{\partial T_{xx}}{\partial t}(x,y,t) = \big(2\mu(x,y)+\lambda(x,y)\big)\frac{\partial v_x}{\partial x}(x,y,t) + \lambda(x,y)\frac{\partial v_y}{\partial y}(x,y,t), \tag{55}$$

$$\frac{\partial T_{xy}}{\partial t}(x,y,t) = \mu(x,y)\left(\frac{\partial v_x}{\partial y}(x,y,t) + \frac{\partial v_y}{\partial x}(x,y,t)\right), \tag{56}$$

$$\frac{\partial T_{yy}}{\partial t}(x,y,t) = \lambda(x,y)\frac{\partial v_x}{\partial x}(x,y,t) + \big(2\mu(x,y)+\lambda(x,y)\big)\frac{\partial v_y}{\partial y}(x,y,t), \tag{57}$$

$$\frac{\partial w_{xx}}{\partial t}(x,y,t) = -\beta_x(x)w_{xx}(x,y,t) + \big(\beta_y(y)-\beta_x(x)\big)\big(2\mu(x,y)+\lambda(x,y)\big)\frac{\partial u_x}{\partial x}(x,y,t), \tag{58}$$

$$\frac{\partial w_{xy}}{\partial t}(x,y,t) = -\beta_y(y)w_{xy}(x,y,t) + \big(\beta_x(x)-\beta_y(y)\big)\mu(x,y)\frac{\partial u_x}{\partial y}(x,y,t), \tag{59}$$

$$\frac{\partial w_{yx}}{\partial t}(x,y,t) = -\beta_x(x)w_{yx}(x,y,t) + \big(\beta_y(y)-\beta_x(x)\big)\mu(x,y)\frac{\partial u_y}{\partial x}(x,y,t), \tag{60}$$

$$\frac{\partial w_{yy}}{\partial t}(x,y,t) = -\beta_y(y)w_{yy}(x,y,t) + \big(\beta_x(x)-\beta_y(y)\big)\big(2\mu(x,y)+\lambda(x,y)\big)\frac{\partial u_y}{\partial y}(x,y,t), \tag{61}$$

with the variables and parameters described in Table 2.

Symbol	**Description**
$x,\ y$	Spatial variables
t	Time
t_0	Initial time instant
$u(x,y,t)$	Displacement of acoustic waves
$v(x,y,t)$	Displacement velocity for 2SD, and material velocity for 1SD
$u_x(x,y,t),\ u_y(x,y,t)$	Displacement of elastic waves in x and y directions, respectively
$v_x(x,y,t),\ v_x(x,y,t)$	Displacement velocity for elastic waves, and material velocity for 1SOD, in x and y directions, respectively
$T_{xx}(x,y,t)$, $T_{xy}(x,y,t),\ T_{yy}(x,y,t)$	Stress components of elastic waves
$w(x,y,t),\quad w_x(x,y,t)$, $w_y(x,y,t),\ w_{xx}(x,y,t)$, $w_{xy}(x,y,t)$, $w_{yx}(x,y,t)$, $w_{yy}(x,y,t)$	auxiliary variables of the PML boundary condition
$c(x,y)$	wave propagation velocities in 1D and 2D, respectively
$\mu(x,y),\ \lambda(x,y)$	Lamé parameters
$\rho(x,y)$	density
$\beta_x(x,y), \beta_y(x,y)$	wave damping functions

Table 2: Variables used in the equations and their description

The damping functions β_z, related to the absorption factor are defined as

$$\beta_z(z) = \begin{cases} 0, & \text{if } d(z,\partial\Omega) > \delta \\ \beta_0 \left(\frac{d(z,\Omega_1)}{\delta}\right)^2, & \text{if } d(z,\partial\Omega) \leq \delta \end{cases}, \quad z = x,\ y \tag{62}$$

where $d(z,\partial\Omega)$ is the distance from z to the boundary of Ω, δ is the thickness of the PML domain, β_0 is the magnitude of the absorption factor, and Ω_1 is the numerical domain without the damping layer (physical domain). Thus, Ω is composed by the union of Ω_1 and a damping layer of thickness δ extending on the boundary of Ω_1.

A.2 Discrete framework

The spatial discretizations are based on a staggered grid using 4th and 8th order approximation of the spatial derivatives defined by equations (20) and (21). Figs. 15 and 16 describe the discrete space for the 1SD and 2SD formulation in 1D, and the 2SD and elastic formulations in 2D, respectively.

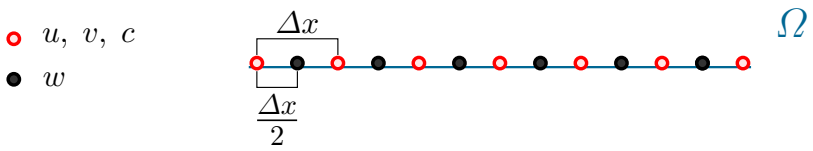

Fig. 15: Staggered grid in 1D with the relative positions of the (2SD) and (1SD) wave equation variables and parameters. u, v and c are collocated (centered) and w is staggered in the grid.

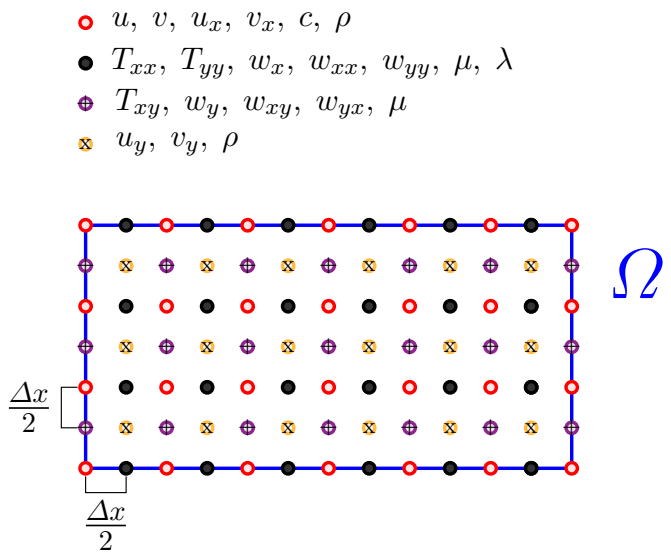

Fig. 16: Staggered grid in 2D with the relative positions of the (2SD and elastic) wave equations variables and parameters. u, v, u_x, v_x, ρ and c are collocated.

A.3 Numerical benchmarks

We define the numerical experiments, called "Test Case" used through the paper. In all the tests we use a zero Dirichlet condition on the boundary of the domain Ω, a PML layer thickness of $\delta = 0.8$km, a damping parameter $\beta_0 = 30$, and Ricker peak frequency of $f_0 = 25$Hz. If not otherwise stated, the initial condition for all the variables is zero. The particular benchmarks are then defined as follows:

Test Case #1: $\Omega = [0, 10.5\text{km}]$

$$c \equiv 1.524\text{km/s}, \quad u_0(x) = ((1 - 10(x - 5.25)^2)e^{-10(x-5.25)^2}, \quad f \equiv 0$$

Test Case #2: $\Omega = [0, 10.5\text{km}]$

$$c(x) = \begin{cases} 1.524 \text{ km/s}, & \text{if } x < 5.25 \\ 3.048 \text{ km/s} & \text{if } 5.25 \le x < 7 \\ 0.1524 \text{ km/s} & \text{if } 7 \le x \end{cases},$$

$$u_0 = \begin{cases} 0, & \text{if } |x-2.6| \ge 0.01 \\ e^{\frac{(x-2.6)^2}{(x-2.6)^2 - 0.01^2}}, & \text{if } |x-2.6| < 0.01 \end{cases}, \quad f \equiv 0$$

Test Case #3: $\Omega = [0, 10.5\text{km}]$

$$c(x) = \begin{cases} 1.524 \text{ km/s}, & \text{if } x < 5.25 \\ 3.048 \text{ km/s} & \text{if } 5.25 \le \end{cases}, \quad u_0 \equiv 0,$$

$$f(x,t) = \begin{cases} 0, & \text{if } |x-2.6| \ge 0.01 \\ e^{\frac{(x-2.6)^2}{(x-2.6)^2 - 0.01^2}} (1 - f_0^2 \pi^2 (t-t_0)^2) e^{-f_0^2 \pi^2 (t-t_0)^2}, & \text{if } |x-2.6| < 0.01 \end{cases}$$

Test Case #4: $\Omega = [0, 8 \text{ km}] \times [0, 8 \text{ km}]$

$$c \equiv 3 \text{ km/s}, \quad u_0(x,y) = \begin{cases} 0, & \text{if } \|(x,y) - (4,2)\| \ge 0.01 \\ e^{\frac{\|(x,y)-(4,2)\|^2}{\|(x,y)-(4,2)\|^2 - 0.01^2}}, & \text{if } \|(x,y) - (4,2)\| < 0.01 \end{cases},$$

$$f \equiv 0$$

Test Case #5: $\Omega = [0, 8 \text{ km}] \times [0, 8 \text{ km}]$

$$c(x,y) = \begin{cases} 3 \text{ km/s, if } y \ge 4 \\ 6 \text{ km/s, if } (y < 4 \text{ and } x \le 6) \text{ or } (16/3 < y < 4 \text{ and } x > 6) \\ 1 \text{ km/s, if } 6 \le x \text{ and } y \le 16/3 \end{cases},$$

$$u_0 = \begin{cases} 0, & \text{if } \|(x,y) - (4,2)\| \ge 0.01 \\ e^{\frac{\|(x,y)-(4,2)\|^2}{\|(x,y)-(4,2)\|^2 - 0.01^2}}, & \text{if } \|(x,y) - (4,2)\| < 0.01 \end{cases}, \quad f \equiv 0$$

Test Case #6: $\Omega = [0, 8 \text{ km}] \times [0, 8 \text{ km}]$

$$c(x,y) = \begin{cases} 3 \text{ km/s, if } y \ge 4 \\ 6 \text{ km/s, if } y < 4 \end{cases}, \quad u_0 \equiv 0,$$

$$f(x,y,t) = \begin{cases} 0, & \text{if } \|(x,y) - (4,2)\| \ge 0.01 \\ e^{\frac{\|(x,y)-(4,2)\|^2}{\|(x,y)-(4,2)\|^2 - 0.01^2}} (1 - f_0^2 \pi (t-t_0)^2) e^{-f_0^2 \pi^2 (t-t_0)^2}, & \text{if } \|(x,y) - (4,2)\| < 0.01 \end{cases}$$

Test Case #7: $\Omega = [0, 8 \text{ km}] \times [0, 8 \text{ km}]$ for elastic waves

$$\rho \equiv 0.25, \quad \mu(x,y) = \begin{cases} 1 \text{ km/s}, & \text{if } y \ge 4 \\ 1.5 \text{ km/s}, & \text{if } (y < 4 \text{ and } x \le 6) \text{ or } (16/3 < y < 4 \text{ and } x > 6) \\ 2.25 \text{ km/s, if } 6 \le x \text{ and } y \le 16/3 \end{cases}$$

$$\lambda(x,y) = \begin{cases} 8 \; km/s, & \text{if } y \ge 4 \\ 12 \; km/s, & \text{if } (y < 4 \text{ and } x \le 6) \text{ or } (16/3 < y < 4 \text{ and } x > 6) \\ 18 \; km/s, & \text{if } 6 \le x \text{ and } y \le 16/3 \end{cases}, \quad u_0 \equiv 0,$$

$$f(x,y,t) = \begin{cases} 0, & \text{if } \|(x,y) - (4,2)\| \ge 0.01 \\ e^{\frac{\|(x,y)-(4,2)\|^2}{\|(x,y)-(4,2)\|^2 - 0.01^2}} (1 - f_0^2 \pi (t-t_0)^2) e^{-f_0^2 \pi^2 (t-t_0)^2}, & \text{if } \|(x,y) - (4,2)\| < 0.01 \end{cases}$$

A.4 Spectrum complementary results

In this subsection, we present the spectral distribution results using the 2SD formulation, along with the real and imaginary limits of the spectrum for the elastic equations with PML.

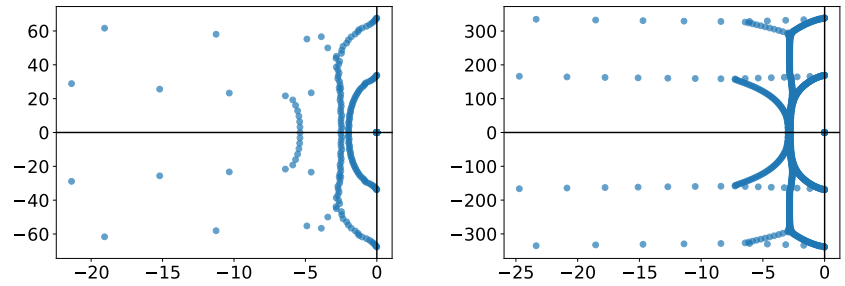

(a) $\Delta x = 0.105$ (b) $\Delta x = 0.021$

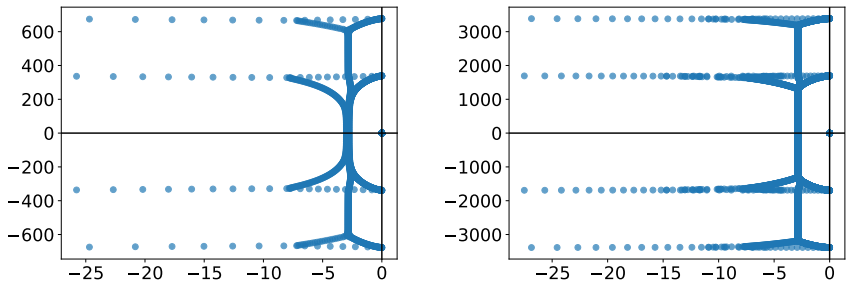

(c) $\Delta x = 0.0105$ (d) $\Delta x = 0.0021$

Fig. 17: Eigenvalues on the complex plane (using coordinates $(Re(\lambda), Im(\lambda))$) using a fourth-order spatial discretization of the acoustic wave equation in one dimension, with formulation 2SD, considering TC#3, for $\Delta x = \{0.105, 0.021, 0.0105, 0.0021\}$. For each Δx, spectrum, the spectrum has a rectangular-shaped convex hull.

Based on Figure,17, it is evident that besides $\sigma(\boldsymbol{H})$ being symmetric with respect to the real axis, the limits of the rectangle on the imaginary axis appear to have a linear relationship with $1/\Delta x$. However, for the real part, the relationship is different, exhibiting a constant negative limit on the left side $(-\beta_0)$ for the PML parameter $\beta_0 > 0$, and a small positive number on the right. In general, we observed similar results for other formulations.

For the acoustic 2SD equations, empirical studies, as the one shown in Figure 6, indicate that the upper bound is a positive small number, smaller than 1. Since in all experiments this upper bound is always close to zero, this will not affect the estimates of the optimal ellipse for Faber polynomial approximations, as the ellipse size will be dominated by the imaginary axis bounds and the lower bound in the real axis. Therefore, a precise upper real bound will not be further required.

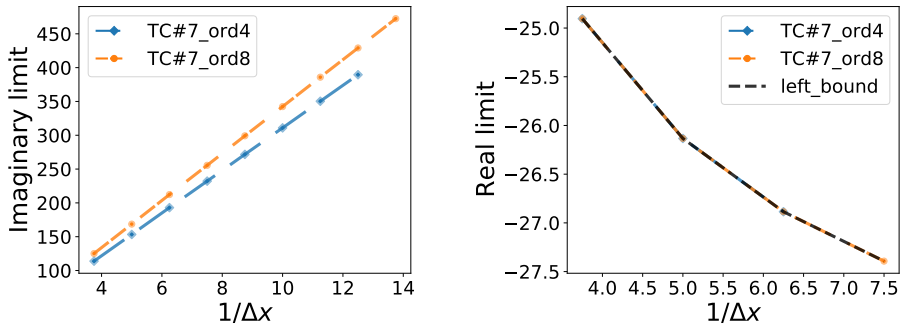

(a) Imaginary limit of the TC#7, in 2D, elastic.

(b) Negative real limit of the TC#7, in 2D, elastic.

Fig. 18: Maximum imaginary parts (left) and lower bound of the real parts (right) of the eigenvalues of $\sigma(\boldsymbol{H})$, for varying $1/\Delta x$.

A.5 Stability and dispersion

Here we present the operators and results of stability and dispersion for all the systems of equations considered in Section A.2 (assuming no PML and no source term), with a spatial discretization of fourth and eighth orders. At the end of the section are also presented the graphics of stability and dispersion of the elastic formulation.

1. 1SD and 2SD in one dimension

$$\Delta t\boldsymbol{H} = \frac{c\Delta t}{\Delta x}\begin{pmatrix} 0 & g_{11} \\ g_{21} & 0 \end{pmatrix}, \qquad \Delta t\boldsymbol{H} = \frac{c\Delta t}{\Delta x}\begin{pmatrix} 0 & 1 \\ h_{11} & 0 \end{pmatrix}.$$

2. 1SD and 2SD in two dimension

$$\Delta t\boldsymbol{H} = \frac{c\Delta t}{\Delta x}\begin{pmatrix} 0 & g_{11} & g_{12} \\ g_{21} & 0 & 0 \\ g_{22} & 0 & 0 \end{pmatrix}, \qquad \Delta t\boldsymbol{H} = \frac{c\Delta t}{\Delta x}\begin{pmatrix} 0 & 1 \\ h_{11}+h_{22} & 0 \end{pmatrix}.$$

3. elastic in two dimension (without considering the decoupled two first equations)

$$\Delta t\boldsymbol{H} = \frac{\Delta t}{\Delta x}\frac{2\mu+\lambda}{\rho}\begin{pmatrix} 0 & 0 & \frac{1}{2\mu+\lambda}g_{11} & \frac{1}{2\mu+\lambda}g_{12} & 0 \\ 0 & 0 & 0 & \frac{1}{2\mu+\lambda}g_{21} & \frac{1}{2\mu+\lambda}g_{22} \\ \rho g_{21} & \frac{\rho\lambda}{2\mu+\lambda}g_{12} & 0 & 0 & 0 \\ \frac{\rho\mu}{2\mu+\lambda}g_{22} & \frac{\rho\mu}{2\mu+\lambda}g_{11} & 0 & 0 & 0 \\ \frac{\rho\lambda}{2\mu+\lambda}g_{21} & \rho g_{12} & 0 & 0 & 0 \end{pmatrix}.$$

Where

1. For 4th order

$$
\begin{aligned}
g_{11} &= \frac{1}{24}\left(27(1-e^{-ik_x\Delta x})+e^{-2k_x\Delta x}-e^{k_x\Delta x}\right)\\
g_{12} &= \frac{1}{24}\left(27(1-e^{-ik_y\Delta x})+e^{-2k_y\Delta x}-e^{k_y\Delta x}\right)\\
g_{21} &= \frac{1}{24}\left(27(e^{ik_x\Delta x}-1)+e^{-k_x\Delta x}-e^{2k_x\Delta x}\right)\\
g_{22} &= \frac{1}{24}\left(27(e^{ik_x\Delta x}-1)+e^{-k_x\Delta x}-e^{2k_x\Delta x}\right)\\
h_{11} &= -\frac{1}{6}\cos(2\theta_x)+\frac{8}{3}\cos(\theta_x)-\frac{5}{2}\\
h_{22} &= -\frac{1}{6}\cos(2\theta_y)+\frac{8}{3}\cos(\theta_y)-\frac{5}{2}
\end{aligned}
$$

2. For 8th order

$$
\begin{aligned}
g_{11} &= \frac{1225}{1024}\left(1-e^{-ik_x\Delta x}+\frac{1}{15}(e^{-2k_x\Delta x}-e^{k_x\Delta x})+\frac{1}{125}(e^{2k_x\Delta x}-e^{-3k_x\Delta x})\right.\\
&\quad\left.+\frac{1}{1715}(e^{-4k_x\Delta x}-e^{3k_x\Delta x})\right)\\
g_{12} &= \frac{1225}{1024}\left(1-e^{-ik_y\Delta x}+\frac{1}{15}(e^{-2k_y\Delta x}-e^{k_y\Delta x})+\frac{1}{125}(e^{2k_y\Delta x}-e^{-3k_y\Delta x})\right.\\
&\quad\left.+\frac{1}{1715}(e^{-4k_y\Delta x}-e^{3k_y\Delta x})\right)\\
g_{21} &= \frac{1225}{1024}\left(e^{ik_x\Delta x}-1+\frac{1}{15}(e^{-k_x\Delta x}-e^{2k_x\Delta x})+\frac{1}{125}(e^{3k_x\Delta x}-e^{-2k_x\Delta x})\right.\\
&\quad\left.+\frac{1}{1715}(e^{-3k_x\Delta x}-e^{4k_x\Delta x})\right)\\
g_{22} &= \frac{1225}{1024}\left(e^{ik_y\Delta x}-1+\frac{1}{15}(e^{-k_y\Delta x}-e^{2k_y\Delta x})+\frac{1}{125}(e^{3k_y\Delta x}-e^{-2k_y\Delta x})\right.\\
&\quad\left.+\frac{1}{1715}(e^{-3k_y\Delta x}-e^{4k_y\Delta x})\right)\\
h_{11} &= -\frac{1}{560}(e^{-4k_x\Delta x}+e^{4k_x\Delta x})+\frac{8}{315}(e^{-3k_x\Delta x}+e^{3k_x\Delta x})-\frac{1}{5}(e^{-2k_x\Delta x}+e^{2k_x\Delta x})\\
&\quad+\frac{8}{5}(e^{-k_x\Delta x}+e^{k_x\Delta x})-\frac{205}{72}\\
h_{22} &= -\frac{1}{560}(e^{-4k_y\Delta x}+e^{4k_y\Delta x})+\frac{8}{315}(e^{-3k_y\Delta x}+e^{3k_y\Delta x})-\frac{1}{5}(e^{-2k_y\Delta x}+e^{2k_y\Delta x})\\
&\quad+\frac{8}{5}(e^{-k_y\Delta x}+e^{k_y\Delta x})-\frac{205}{72}
\end{aligned}
$$

A.6 Convergence

In this section, we detail the construction of the RK(9-7) scheme employed for computing the reference solution. Furthermore, we provide the convergence and computational efficiency results achieved through the utilization of Faber polynomials in solving elastic wave propagation equations.

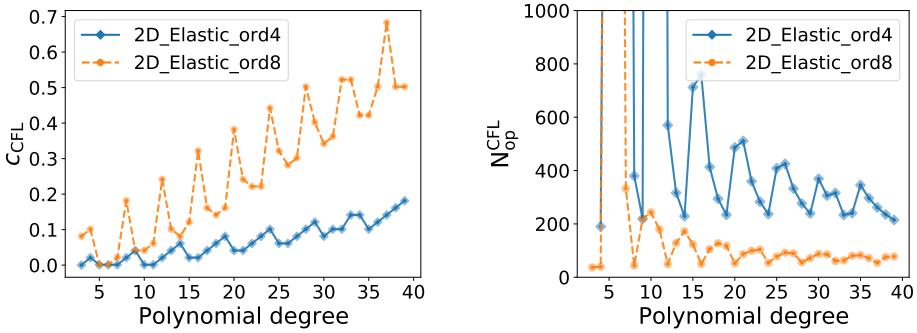

(a) CFL number of the 2D, elastic equations. (b) N_{op}^{CFL} quantity of the 2D, elastic equations.

Fig. 19: Stability graphics of the Faber approximation method for different spatial discretizations, and polynomial degrees $m = \{3, 4, ..., 40\}$, for the elastic formulation. The CFL number (left), and the measure of the operations number of Eq. (33) (right). Higher polynomial degrees implies in larger c_{CFL}, but this does not necessarily results in a decrease of the MVOs.

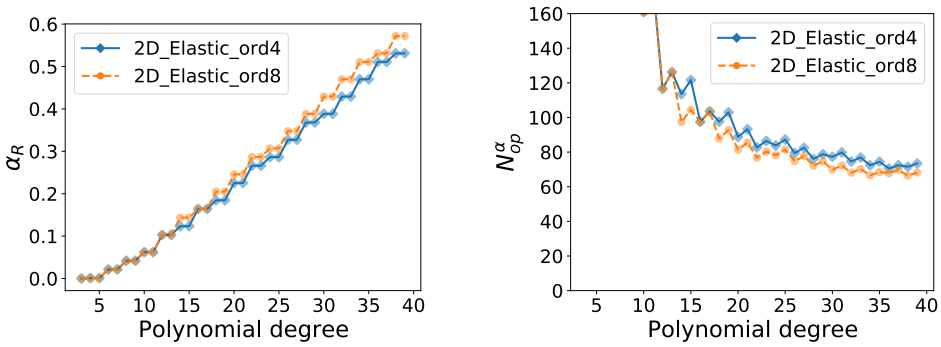

(a) Dispersion number, α_R, of the 2D, elastic equations. (b) N_{op}^{α} quantity of the 2D, elastic equations.

Fig. 20: Dispersion studies of Faber approximation method using different spatial discretizations, dimensions, equations formulations, and polynomial degrees $m = \{3, 4, ..., 40\}$. Higher polynomial degrees implies larger α_R and a non-monotonous decrease of the operations number.

RK(9-7) algorithm:

$$\boldsymbol{k}_1 = \boldsymbol{H}\boldsymbol{u}_n + \boldsymbol{f}(t_n)$$

$$\boldsymbol{k}_2 = \boldsymbol{H}\left(\boldsymbol{u}_n + \frac{4}{63}\Delta t\boldsymbol{k}_1\right) + \boldsymbol{f}\left(t_n + \frac{4}{63}\Delta t\right)$$

$$\boldsymbol{k}_3 = \boldsymbol{H}\left(\boldsymbol{u}_n + \Delta t\left[\frac{1}{42}\boldsymbol{k}_1 + \frac{1}{14}\boldsymbol{k}_2\right]\right) + \boldsymbol{f}\left(t_n + \frac{2}{21}\Delta t\right)$$

$$\boldsymbol{k}_4 = \boldsymbol{H}\left(\boldsymbol{u}_n + \Delta t\left[\frac{1}{28}\boldsymbol{k}_1 + \frac{3}{28}\boldsymbol{k}_3\right]\right) + \boldsymbol{f}\left(t_n + \frac{1}{7}\Delta t\right)$$

$$\boldsymbol{k}_5 = \boldsymbol{H}\left(\boldsymbol{u}_n + \Delta t\left[\frac{12551}{19652}\boldsymbol{k}_1 - \frac{48363}{19652}\boldsymbol{k}_3 + \frac{10976}{4913}\boldsymbol{k}_4\right]\right) + \boldsymbol{f}\left(t_n + \frac{7}{17}\Delta t\right)$$

$$\boldsymbol{k}_6 = \boldsymbol{H}\left(\boldsymbol{u}_n + \Delta t\left[-\frac{36616931}{27869184}\boldsymbol{k}_1 + \frac{2370277}{442368}\boldsymbol{k}_3 - \frac{255519173}{63700992}\boldsymbol{k}_4 + \frac{226798819}{445906944}\boldsymbol{k}_5\right]\right) + \boldsymbol{f}\left(t_n + \frac{13}{24}\Delta t\right)$$

$$\boldsymbol{k}_7 = \boldsymbol{H}\left(\boldsymbol{u}_n + \Delta t\left[-\frac{10401401}{7164612}\boldsymbol{k}_1 + \frac{47383}{8748}\boldsymbol{k}_3 - \frac{4914455}{1318761}\boldsymbol{k}_4 - \frac{1498465}{7302393}\boldsymbol{k}_5 + \frac{2785280}{3739203}\boldsymbol{k}_6\right]\right) + \boldsymbol{f}\left(t_n + \frac{7}{9}\Delta t\right)$$

$$\boldsymbol{k}_8 = \boldsymbol{H}\left(\boldsymbol{u}_n + \Delta t\left[\frac{181002080831}{17500000000}\boldsymbol{k}_1 - \frac{14827049601}{400000000}\boldsymbol{k}_3 + \frac{23296401527134463}{857600000000000}\boldsymbol{k}_4 + \frac{2937811552328081}{949760000000000}\boldsymbol{k}_5 - \frac{243874470411}{69355468750}\boldsymbol{k}_6 + \frac{2857867601589}{3200000000000}\boldsymbol{k}_7\right]\right) + \boldsymbol{f}\left(t_n + \frac{91}{100}\Delta t\right)$$

$$\boldsymbol{k}_9 = \boldsymbol{H}\left(\boldsymbol{u}_n + \Delta t\left[-\frac{228380759}{19257212}\boldsymbol{k}_1 + \frac{4828803}{113948}\boldsymbol{k}_3 - \frac{331062132205}{10932626912}\boldsymbol{k}_4 - \frac{12727101935}{3720174304}\boldsymbol{k}_5 + \frac{22627205314560}{4940625496417}\boldsymbol{k}_6 - \frac{268403949}{461033608}\boldsymbol{k}_7 + \frac{3600000000000}{19176750553961}\boldsymbol{k}_8\right]\right) + \boldsymbol{f}\left(t_n + \Delta t\right)$$

$$\boldsymbol{u}_{n+1} = \boldsymbol{u}_n + \Delta t\left(\frac{95}{2366}\boldsymbol{k}_1 + \frac{3822231133}{16579123200}\boldsymbol{k}_4 + \frac{555164087}{2298419200}\boldsymbol{k}_5 + \frac{1279328256}{9538891505}\boldsymbol{k}_6 + \frac{5963949}{25894400}\boldsymbol{k}_7 + \frac{50000000000}{599799373173}\boldsymbol{k}_8 + \frac{28487}{712800}\boldsymbol{k}_9\right).$$

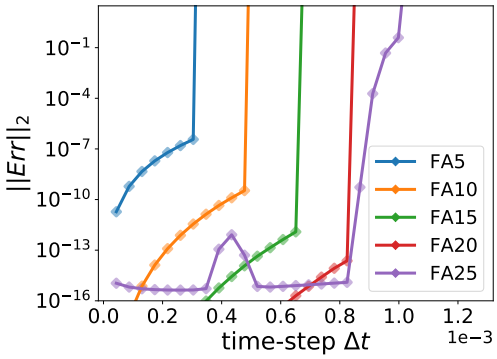

Fig. 21: Approximation error of Faber polynomials using the elastic equations, to solve TC#7. The curves represent the error when using polynomial of degrees $m = \{5, 10, \ldots, 25\}$. Increasing the degree of the polynomial allows for larger steps in time, while keeping the approximation error smaller than a fixed threshold.

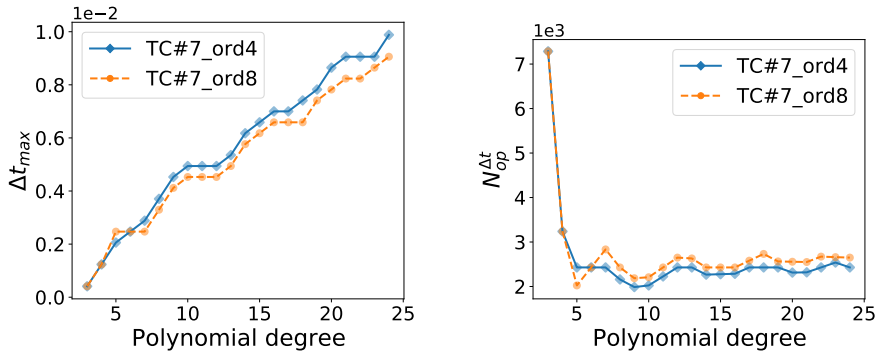

(a) Maximum time step, $\Delta t_{\max}$, for TC#7, using 4th and 8th order spatial discretization.

(b) Number of computations, $N_{op}^{\Delta t}$, for TC#7, using 4th and 8th order spatial discretization.

Fig. 22: Convergence in polynomial order for the elastic equations, using different spatial discretization orders, and a wide range of polynomial degrees. The maximum Δt such that the error of Faber approximations is less than 10^{-6} is shown on the right. On the left, we show the number of operations using the values of $\Delta t_{\max}$ of the upper line. When the polynomial degree increases, the maximum allowed time-step size also increases, together with a decrease of the number of operations.

Remark: In Section 4.1 of Chapter 2, the interval limiting the wavenumber k is $\left[-\frac{1}{2\Delta x}, \frac{1}{2\Delta x}\right]$, instead of $\left[-\frac{1}{\Delta x}, \frac{1}{\Delta x}\right]$.

Chapter 3

High-order exponential integration for seismic wave modeling

This chapter complements our earlier discussion of the optimal adaptation of Faber polynomials in seismic imaging. The primary objective of Chapter 3 is to enhance our comprehension of Faber method potential by comparing it to other well-studied explicit exponential integrators of arbitrary order in the context of seismic imaging, with the aim of determining which method is most qualified. Furthermore, we extend this comparison to include classical low-order methods, providing a comprehensive evaluation of the performance of explicit exponential integrators against commonly used techniques for solving the wave propagation equations. The metrics used for comparison include numerical dispersion, dissipation, convergence, computational cost, and memory utilization.

In Chapter 3, our focus lies on maximizing the time-step of each method while ensuring the accuracy of the solutions remains high. However, it's noteworthy that the time sample rate of seismograms in seismic imaging applications typically operates at a finer scale, around 4 ms. Nevertheless, methods employing larger time-steps are still atractive. This is because if the time-step they can accommodate surpasses the sampling interval, it enables several computations in parallel for smaller time steps, thus enhancing efficiency.

This chapter offers a more comprehensive understanding of the application of explicit exponential integrators in solving the wave equations. It is a self-sufficient Chapter, since it has been written as an article submitted for publication in the journal of Computational Geosciences, co-authored with my advisor Pedro Peixoto and co-advisor Martin Schreiber. I believe it contributes to our knowledge of this class of methods and serves as a first step not only for their application in the linear wave equations with ABC, but also, for linear quasi-hyperbolic partial differential equations.

Noname manuscript No.
(will be inserted by the editor)

High-order exponential integration for seismic wave modeling

Fernando V. Ravelo · Martin Schreiber · Pedro S. Peixoto

Received: date / Accepted: date

Abstract Seismic imaging is a major challenge in geophysics with broad applications. It involves solving wave propagation equations with absorbing boundary conditions (ABC) multiple times. This drives the need for accurate and efficient numerical methods. This study examines a collection of exponential integration methods, known for their good numerical properties on wave representation, to investigate their efficacy in solving the wave equation with ABC. The purpose of this research is to assess the performance of these methods. We compare a recently proposed Exponential Integration based on Faber polynomials with well-established Krylov exponential methods alongside a high-order Runge-Kutta scheme and low-order classical methods. Through our analysis, we found that the exponential integrator based on the Krylov subspace exhibits the best convergence results among the high-order methods. We also discovered that high-order methods can achieve computational efficiency similar to lower-order methods while allowing for considerably larger time steps. Most importantly, the possibility of undertaking large time steps could be used for important memory savings in full waveform inversion imaging problems.

1 Introduction

The resolution of wave propagation equations is a widely researched topic due to its broad range of applications in various fields. One particularly prominent

Fernando V. Ravelo E-mail: fernanvr@ime.usp.br · Pedro S. Peixoto E-mail: ppeixoto@usp.br
Instituto de Matemática e Estatística, Universidade de São Paulo, Brazil

Martin Schreiber E-mail: martin.schreiber@univ-grenoble-alpes.fr
Université Grenoble Alpes / Laboratoire Jean Kuntzmann / Inria, France
Technical University of Munich, Germany

application is seismic imaging, where material parameters of underground regions are estimated based on seismic data. This technique is extensively utilized in the industry for the exploration and extraction of fossil fuels [Ikelle and Amundsen, 2018].

The numerical approximation of propagating wave equations is a critical stage in this procedure. Consequently, the complexity of the problem impels the development of novel techniques competitive to the efficiency and accuracy of existing schemes [Alkhadhr et al., 2021, Kwon et al., 2020, Lee, 2023].

The propagation of elastic waves can be described as a linear hyperbolic system of PDEs. Nonetheless, the addition of absorbing boundary conditions to replicate an infinite domain modifies the eigenvalues, and they are no longer purely imaginary. In this context, low-order classical explicit schemes such as the Leap-Frog [Ruud and Hestholm, 2001] approximation, fourth-order Runge-Kutta [Walters et al., 2020], and similar methods [Jing et al., 2019, Li and Liao, 2020] have proven effective. Nevertheless, despite their computational speed, these algorithms require very small time steps to approximate the solution accurately. Consequently, this leads to high memory requirements, which can be a significant challenge in solving inverse problems, which is another crucial step in seismic imaging.

In recent decades, a class of numerical algorithms known as exponential integrators have emerged and demonstrated successful applications in various fields. These algorithms have been effectively utilized in areas such as photonics [Pototschnig et al., 2009], the development of numerical methods for weather prediction [Peixoto and Schreiber, 2019], and the modeling of diverse physical phenomena [Loffeld and Tokman, 2013], often surpassing the performance of classical schemes. Another example of successful applications of exponential integrators is provided by Brachet et al. [2022], where classical explicit and implicit schemes were compared with exponential integrators, revealing that exponential integrators exhibit superior dissipation and dispersion properties. In Cohen and Dujardin [2017], exponential integrators were compared with explicit and implicit schemes for solving the non-linear Schrödinger equation, demonstrating accuracy comparable to the best performance of classical methods and surpassing other schemes such as the Crank-Nicholson method. In Iyiola and Wade [2018], an exponential integrator was compared with an Implicit-Explicit (IMEX) scheme and a second-order backward difference scheme for solving non-linear space-fractional equations, concluding that it offers a significantly larger stability region. Enabling the use of larger time steps, with the potential for parallel implementation to enhance efficiency. Exponential integrators are typically employed to preserve favorable dispersion properties while allowing for larger time steps Schreiber et al. [2019].

Exponential integrators can be categorized into two types: one primarily concerned with approximating the exponential (or related φ-functions) of a large matrix resulting from the spatial discretization of the linear term of a system of PDE, and the other focused on different schemes to approximate the non-linear term [Hochbruck and Ostermann, 2010, Mossaiby et al., 2015]. In the context of wave propagation equations with absorbing boundary condi-

tions, these equations are primarily governed by the linear term, and a source function replaces the non-linear term with a well-defined analytic representation. This leads to a transformation of the problem, as demonstrated by Al-Mohy and Higham [2011], which is a generalization of the work of Sidje [1998], where the problem transforms into calculating the exponential of a slightly enlarged matrix.

The approximation of a matrix exponential has received significant attention [Acebron, 2019, Alonso et al., 2023, Moler and Van Loan, 2003]. Numerous exponential integrators have been developed to address this matrix function calculation [Al-Mohy and Higham, 2011, Hochbruck and Ostermann, 2010, Lu, 2003]. One notable exponential integrator is based on the Krylov subspace, with several schemes utilizing this approach and demonstrating good performance [Gaudreault et al., 2021, Niesen and Wright, 2009, Sidje, 1998]. Another method relies on rational approximations [Al-Mohy and Higham, 2010], which are generally implicit and less suitable for large operators. However, they can be combined with the Krylov method to reduce matrix dimensions [Al-Mohy and Higham, 2011]. Another approach utilizes Chebyshev polynomials, an explicit method that can be formulated as a three-term recurrence relation [Bergamaschi and Vianello, 2000, Kole, 2003]. Additionally, there are other methodologies, such as Leja points interpolation [Bergamaschi et al., 2004, Deka et al., 2023], optimized Taylor approximations [Bader et al., 2019], and contour integrals [Schmelzer and Trefethen, 2006], among others.

When applied to solve hyperbolic systems, such as the wave equations in heterogeneous media, their performance is poorly understood. To the best of our knowledge, only a limited number of literature publications have focused on methods of practical relevance for this specific problem [Kole, 2003, Kosloff et al., 1989, Ravelo F, 2023, Tal-Ezer et al., 1987, Tessmer, 2011, Zhang et al., 2014].

In Zhang et al. [2014], an implicit exponential integrator method is developed, and a comparison with other methods is presented, demonstrating superior results in terms of accuracy and dispersion. However, a notable drawback of the implicit method is its high computational cost for each time step, making it primarily suitable for very stiff problems.

Kole [2003] proposes an explicit exponential integrator based on Chebyshev polynomial approximations, which achieves high solution accuracy and permits large time steps. Nevertheless, the applicability of Chebyshev polynomials for approximating the solution is limited to cases where the system matrix is symmetric or antisymmetric, preventing the modeling of absorbing boundary conditions. As a result, its usage in seismic applications is constrained.

In the researches [Kosloff et al., 1989, Tal-Ezer et al., 1987, Tessmer, 2011] there have been proposed the use of Chebyshev expansions to approximate the matrix exponential, and with the use of absorbing boundary conditions. Nonetheless, the numerical results are primarily validated using simplistic ABCs, and there is a lack of proof demonstrating convergence for these boundary conditions.

In previous work [Ravelo F, 2023], we explored a generalization of the exponential integrator using Faber polynomials, a variant of Chebyshev polynomials. This approach enabled us to solve the wave equations with absorbing boundary conditions. We found that employing higher approximation degrees in the Faber polynomial-based method allows for increased time step sizes without incurring additional computational costs. Furthermore, the augmented time step approximations exhibit favorable accuracy and dispersion properties.

A notable gap in the existing literature is the absence of experiments comparing high-order methods with classical low-order schemes for solving wave equations with absorbing boundary conditions. Our work fills in this gap by comparing exponential integrators based on Faber polynomials, Krylov subspace projection, and High-order Runge-Kutta with various classical methods. Specifically, we consider classical low-order methods such as Leap-frog, fourth-order and four-stage Runge-Kutta (RK4-4), second-order and three-stage Runge-Kutta (RK3-2), and seventh-order and nine-stage Runge-Kutta (RK9-7). Detailed descriptions of these methods can be found in Section 3. The comparison between these algorithms focuses on several key characteristics, including numerical dispersion, dissipation, convergence, and computational cost, which are thoroughly discussed in Sections 4 and 5. By investigating these aspects, we aim to comprehensively evaluate the different methods and their suitability for solving wave equations with absorbing boundary conditions. Finally, in Section 6, we summarize the main findings and draw conclusive remarks based on our research.

2 The wave equation

The execution of finite difference methods when solving a system of partial differential equations depends on the continuum formulation and the approximation of the spatial derivatives [Thomas, 2013]. These factors directly impact the discrete operator used in the computations. This section lays the groundwork for the entire analysis presented in the manuscript. We discuss the fundamental elements defining the discrete spatial operator present in seismic imaging applications. These elements include formulating wave propagation equations with absorbing boundary conditions (ABC), spatial discretization using derivative approximations, and free surface treatment.

We employ Perfectly Matching Layers (PML) as the absorbing boundary condition [Assi and Cobbold, 2017] to simulate an infinite domain. Despite the significant computational cost associated with PML absorbing boundaries, they remain widely used in numerous numerical studies within the field of seismic imaging [Chern, 2019, Jing et al., 2019, Tago et al., 2012]. For computational efficiency, we implement the PML for the two-dimensional acoustic wave propagation equations. While we can extend our analysis to propagating waves in three dimensions, the complexity of the equations substantially increases, resulting in a significant rise in computational requirements. Thus, for

our purposes, we define the system of equations within a rectangular domain $\Omega = [0, a] \times [0, -b]$ for $t > 0$, as follows:

$$\frac{\partial}{\partial t}\begin{pmatrix} u \\ v \\ w_x \\ w_y \end{pmatrix} = \begin{pmatrix} 0 & 1 & 0 & 0 \\ -\beta_x\beta_y + c^2\left(\frac{\partial^2}{\partial x^2} + \frac{\partial^2}{\partial y^2}\right) & -(\beta_x + \beta_y) & c^2\frac{\partial}{\partial x} & c^2\frac{\partial}{\partial y} \\ (\beta_y - \beta_x)\frac{\partial}{\partial x} & 0 & -\beta_x & 0 \\ (\beta_x - \beta_y)\frac{\partial}{\partial y} & 0 & 0 & -\beta_y \end{pmatrix}\begin{pmatrix} u \\ v \\ w_x \\ w_y \end{pmatrix} + \begin{pmatrix} 0 \\ f \\ 0 \\ 0 \end{pmatrix}, \tag{1}$$

where, $u = u(t, x, y)$ is the displacement, $c = c(x, y)$ is the given velocity distribution in the medium, $v = v(t, x, y)$ is the wave velocity, and $f = f(x, y, t)$ is the source term. The w-functions, $(w_x, w_y) = (w_x(t, x, y), w_y(t, x, y))$, are the auxiliary variables of the PML approach and the β-functions are known and control the damping factor in the absorbing layer.

$$\beta_z(z) = \begin{cases} 0, & \text{if } d(z, \partial\Omega) > \delta \\ \beta_0\left(1 - \frac{d(z,\Omega)}{\delta}\right)^2, & \text{if } d(z, \partial\Omega) \leq \delta \end{cases}, \quad z \in \{x,\ y\} \tag{2}$$

where $d(z, \partial\Omega)$ is the distance from z to the boundary of Ω, δ is the thickness of the PML domain, and β_0 is the magnitude of the absorption factor. Thus, the domain Ω comprises a physical domain, where the wave propagates normally, and an outer layer of thickness δ (the domain of the PML), where the waves dampen.

Due to the attenuation of displacement within the PML domain, we opt for a Dirichlet boundary condition (null displacement) along three sides of the rectangular domain Ω. However, this boundary condition does not apply to the top side, as a free-surface boundary condition is more suitable for seismic-imaging simulations. Therefore, on the upper side of Ω, we exclude the PML domain ($\beta_y(y) = 0$, for all $y \in [0, \delta]$), and determine the solution approximation at the upper boundary based on the chosen spatial discretization.

2.1 Spatial discretization

Several finite difference discretization schemes have been proposed for the wave propagation equations [Jing et al., 2019, Miao and Zhang, 2022, Moczo et al., 2000, Robertsson and Blanch, 2020, Zingg et al., 1996]. While determining the optimal approach remains an open problem, staggered grids have gained significant popularity for these equations, as noted in Moczo et al. [2000]. Staggered grids offer the capability to consider information of wave up to wavenumbers of $\frac{1}{\Delta x}$. Additionally, in the study of Moczo et al. [2000], the effectiveness of second and fourth order staggered grid spatial discretizations was compared for solving the wave equation, with the fourth-order discretization demonstrating superior accuracy and stability over the second-order counterpart. As our main interest is the time integration methods, to minimize spatial numerical errors we adopted an eighth-order staggered grid spatial discretization. However, we

do not use higher-order approximations, as their advantage in the numerical approximation is unclear and they have greater computational demands.

The spatial discretization consists of a uniform staggered grid ($\Delta x = \Delta y$) of 8th-order. The positions of the discrete points are depicted in Fig. 1.

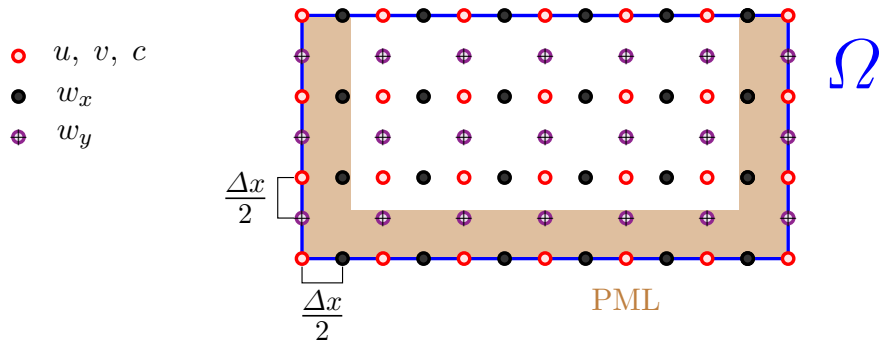

Fig. 1: Uniform staggered grid in 2D with the relative positions of the acoustic wave equations' variables and parameters. u, v and c are collocated. The shaded region represents the PML domain.

For the inner discrete points, the 8th-order approximation of the derivatives is given by

$$\frac{\partial u_{i+\frac{1}{2}}}{\partial x} \approx \frac{1225}{1024\Delta x}\left(u_{i+1} - u_i - \frac{u_{i+2} - u_{i-1}}{15} + \frac{u_{i+3} - u_{i-2}}{125} - \frac{u_{i+4} - u_{i-3}}{1715}\right) \tag{3}$$

$$\frac{\partial^2 u_i}{\partial x^2} \approx -\frac{205}{72}u_i + \frac{8}{5}\left(u_{i+1} - u_{i-1}\right) - \frac{1}{5}\left(u_{i+2} - u_{i-2}\right) + \frac{8}{315}\left(u_{i+3} - u_{i-3}\right) - \frac{1}{560}\left(u_{i+4} - u_{i-4}\right) \tag{4}$$

with analogous expressions for the y-coordinate in the 2D discretization.

The approximation of derivatives near the sides and bottom boundaries, where Dirichlet boundary conditions within a PML domain are applied, is performed using the formulas (3) and (4). In these cases, the function values required outside the domain Ω are set to zero. However, this does not impact the accuracy of the numerical approximations because, within the PML domain, the wave amplitudes decrease to zero.

A different strategy is necessary to approximate derivatives at points near the upper boundary. Since there is no PML domain, and the boundary condition corresponds to a free surface.

2.2 Free surface

From the free-surface condition $\nabla u \cdot (0,1) = 0$, we deduce the Neumann boundary condition $\frac{\partial u}{\partial y} = 0$. Additionally, by substituting $\beta_y = 0$ at the free surface in the third equation of 1, we obtain $w_y = 0$ at the free surface. Utilizing these values, we can approximate the required spatial derivatives of the functions in (1) concerning the variable y.

There are two main approaches for approximating the spatial derivatives concerning y. The first approach introduces artificial points outside Ω, assigning function values at these points to satisfy the conditions at the free surface. The second procedure involves approximating the derivatives at the free surface and its nearest points using only the function values within the domain Ω, without artificially extending the functions. According to Kristek et al. [2002], the latter alternative brings greater accuracy to the numerical solution and is the approach employed throughout this work.

Next, assuming that the grid points lying on the free surface correspond to the evaluation of the displacement u (i.e., the free surface is at $y = 0$), we need 8th-order approximations for

1. the second derivative $\frac{\partial^2 u}{\partial y^2}$ at the points with $y = \{0, -\Delta x, -2\Delta x, -3\Delta x\}$.
2. the first derivative $\frac{\partial u}{\partial y}$ at the points with $y = \{-\frac{1}{2}\Delta x, -\frac{3}{2}\Delta x, -\frac{5}{2}\Delta x\}$.
3. the first derivative $\frac{\partial w_y}{\partial y}$ at the points with $y = \{0, -\Delta x, -2\Delta x, -3\Delta x\}$.

The referred approximations for the derivatives $\frac{\partial^2 u}{\partial y^2}$ and $\frac{\partial u}{\partial y}$, using Taylor expansions, can be found in the Appendix A.1. As for the derivative $\frac{\partial w_y}{\partial y}$, we apply the algorithm outlined in Fornberg [1988]. This algorithm computes the derivative with any approximation order and utilizes an arbitrary points distribution where the values of the derived function are known.

3 Time integration methods

After characterizing the spatial discretization and the approximation of the spatial derivatives, we obtain the following linear system of equations:

$$\frac{d}{dt}\boldsymbol{U}(t) = \boldsymbol{H}\boldsymbol{U}(t) + \boldsymbol{f}(t), \quad \boldsymbol{U}(t_0) = \boldsymbol{U}_0. \tag{5}$$

Here, $\boldsymbol{U}(t)$ is a vector comprising the discretized functions u, v, w_x, and w_y, while the matrix $\boldsymbol{H}$ represents the discretized spatial operator of the system (1). The vector $\boldsymbol{f}$ consists of the source function evaluated at each grid point.

Most of the numerical methods described in this section solve the first-order system of ordinary differential equations (5). Our primary focus lies in approximating the time dimension, leading to the classification of methods as either low or high order concerning time. The following subsections present the numerical schemes employed in the former classifications.

3.1 Low order methods

We consider four low-order methods that offer attractive features for approximating the solution of wave equations. Three of these methods are based on the Runge-Kutta (RK) approach, while the fourth is the Leap-frog scheme.

- **2nd order Runge-Kutta (RK3-2):** The RK3-2 method is a second-order RK scheme with three stages. It is a modification of the classical RK2-2 method designed to increase its stability region [Crouseilles et al., 2020], enabling its application to hyperbolic problems. The scheme can be expressed as follows:

$$\begin{aligned}
\boldsymbol{k_1} &= H\boldsymbol{u}^n + \boldsymbol{f}(t_n),\\
\boldsymbol{k_2} &= H(\boldsymbol{u}^n + (\Delta t/2)\boldsymbol{k_1}) + \boldsymbol{f}(t_n + \Delta t/2),\\
\boldsymbol{k_3} &= H(\boldsymbol{u}^n + (\Delta t/2)\boldsymbol{k_2}) + \boldsymbol{f}(t_n + \Delta t/2),\\
\boldsymbol{u}^{n+1} &= \boldsymbol{u}^n + \Delta t\boldsymbol{k_3}.
\end{aligned}$$

- **4th order Runge-Kutta (RK4-4):** The classical RK4-4 scheme balances stability region and computational requirements [Burden et al., 2015].
- **7th order Runge-Kutta of nine stages (RK9-7):** This scheme has been specifically constructed for hyperbolic equations and exhibits favorable dispersion properties [Calvo et al., 1996].
- **Two step method (Leap-frog):** The Leap-frog method is highly efficient for solving wave equations. It utilizes two time steps to approximate the second-order time derivative. The equations solved by the Leap-frog method are

$$\begin{aligned}
\frac{\partial^2 u}{\partial t^2} &= -\beta_x\beta_y u - (\beta_x + \beta_y)\frac{\partial u}{\partial t} + c^2\left(\frac{\partial^2 u}{\partial x^2} + \frac{\partial^2 u}{\partial y^2} + \frac{\partial \omega_x}{\partial x} + \frac{\partial \omega_y}{\partial y}\right) + f\\
\frac{\partial w_x}{\partial t} &= -\beta_x w_x + (\beta_y - \beta_x)\frac{\partial u}{\partial x}\\
\frac{\partial w_y}{\partial t} &= -\beta_y w_y + (\beta_x - \beta_y)\frac{\partial u}{\partial y}
\end{aligned}$$

  with the discrete approximations in time

$$\begin{aligned}
\frac{\partial^2 u_i^n}{\partial t^2} &\approx \frac{u_i^{n+1} - 2u_i^n + u_i^{n-1}}{\Delta t^2},\\
\frac{\partial w^n_{z_{i+1/2}}}{\partial t} &\approx \frac{w^{n+1}_{z_{i+1/2}} - w^{n-1}_{z_{i+1/2}}}{2\Delta t}, \text{ with } z \in \{x, y\}.
\end{aligned}$$

3.2 High order methods

The methods presented in this section are of arbitrary order and utilize exponential integrators based on Faber polynomials, Krylov subspaces, and a high-order Runge-Kutta method.

According to Hochbruck and Ostermann [2010], an exponential integrator approximates the semi-analytic solution of (5) using the formula of constant variation

$$\boldsymbol{U}(t) = e^{(t-t_0)\boldsymbol{H}}\boldsymbol{U}_0 + \int_{t_0}^{t} e^{(t-\tau)\boldsymbol{H}}\boldsymbol{f}(\tau)d\tau.$$

Expanding the function $\boldsymbol{f}$ in a Taylor series, the solution of (3.2) can be expressed as the matrix exponential [Al-Mohy and Higham, 2011]

$$\boldsymbol{u}(t) = \begin{bmatrix}\boldsymbol{I}_{n\times n} & \boldsymbol{0}\end{bmatrix} e^{(t-t_0)\tilde{\boldsymbol{H}}} \begin{bmatrix}\boldsymbol{u}_0 \\ \boldsymbol{e}_p\end{bmatrix}, \tag{6}$$

where $\boldsymbol{e}_p \in \mathbb{R}^p$ is a vector with zeros in its first $p-1$ elements and one in its last element, $\boldsymbol{I}_{n\times n}$ is the identity matrix of dimension n, and

$$\tilde{\boldsymbol{H}} = \begin{pmatrix}\boldsymbol{H} & \boldsymbol{W} \\ \boldsymbol{0} & \boldsymbol{J}_{p-1}\end{pmatrix},$$

where the columns of the matrix $\boldsymbol{W}$ consist of the values of the function $\boldsymbol{f}$ and the approximations of the first $p-1$ derivatives of $\boldsymbol{f}$, and $\boldsymbol{J}_{p-1}$ is a square matrix of dimensions $p\times p$ with ones in the upper diagonal and zeros elsewhere.

Equation (6) forms the basis for the exponential integrator methods implemented in this research, and the approach used to compute the matrix exponential in (6) determines each of the following exponential integrators.

- **Faber approximation (FA):** This method is an exponential integrator based on Faber polynomials. As presented in Ravelo F [2023], the exponential approximation is carried on with the three-term recurrence Faber series

$$\begin{aligned}
&\boldsymbol{F}_0(\boldsymbol{H}) = \boldsymbol{I}_{n\times n}, \quad \boldsymbol{F}_1(\boldsymbol{H}) = \boldsymbol{H}/\gamma - c_0\boldsymbol{I}_{n\times n}, \\
&\boldsymbol{F}_2(\boldsymbol{H}) = \boldsymbol{F}_1(\boldsymbol{H})\boldsymbol{F}_1(\boldsymbol{H}) - 2c_1\boldsymbol{I}_{n\times n}, \\
&\boldsymbol{F}_j(\boldsymbol{H}) = \boldsymbol{F}_1(\boldsymbol{H})\boldsymbol{F}_{j-1}(\boldsymbol{H}) - c_1\boldsymbol{F}_{j-2}(\boldsymbol{H}), \quad j \geq 3,
\end{aligned}$$

  where the parameters c_0 and c_1 depend on the eigenvalues distribution of the operator $\boldsymbol{H}$. Then, the solution in the next time instant is expressed as

$$\boldsymbol{u}^{n+1} = \sum_{j=0}^{m} a_j \boldsymbol{F}_j(\boldsymbol{H})\boldsymbol{u}^n, \tag{7}$$

  where a_j are the Faber coefficients.
- **Krylov subspace projection (KRY):** This method is an exponential integrator utilizing operator projections within the Krylov subspace. Various proposed algorithms involve adaptive time steps and different strategies for generating the subspace basis [Gaudreault et al., 2021]. However, to ensure an impartial comparison among all the schemes, we opt for the traditional Arnoldi algorithm to establish the vector basis and perform the projection of H [Gallopoulos and Saad, 1992].

$\boldsymbol{u}_1 = \boldsymbol{u}_0/\|\boldsymbol{u}_0\|_2$
Do j from 1 to m:
  $\boldsymbol{w} = \boldsymbol{H}\boldsymbol{u}_j$
  Do k from 1 to j:
    $A_{i,j} = \boldsymbol{w} \cdot \boldsymbol{u}_k$
    $\boldsymbol{w} = \boldsymbol{w} - A_{i,j}\boldsymbol{u}_k$
  $A_{j+1,j} = \|\boldsymbol{w}\|_2$
  $\boldsymbol{u}_{j+1} = \boldsymbol{w}/A_{j+1,j}$
Then, $e^{\boldsymbol{H}}\boldsymbol{u}_0 \approx \|\boldsymbol{u}_0\|_2[\boldsymbol{u}_1|\ldots|\boldsymbol{u}_m]e^{\boldsymbol{A}}\boldsymbol{e}_1$

Listing 1: Pseudocode of Arnoldi algorithm.

After constructing the matrix projection $\boldsymbol{A}$, we compute the reduced matrix's exponential using the Padé polynomial approximation method, as outlined in Al-Mohy and Higham [2011].
The Arnoldi algorithm to construct an orthonormal basis is very computationally intensive, and the amount of matrix-vector operations does not represent its actual computational cost. Regarding this subject, the use of non-orthonormal bases has been proposed to greatly reduce this cost Gaudreault et al. [2021]. However, due to the non-orthogonality of the Krylov basis, the reduced matrix $\boldsymbol{A}$ does not represent an orthogonal projection of the linear transformation $\boldsymbol{H}$ onto the Krylov subspace [Gaudreault et al., 2021]. This discrepancy may lead to numerical errors that differ from those encountered in the classical Arnoldi method. As we aim to use the classical Krylov method, we employ the Arnoldi algorithm without considering the cost of constructing the Krylov subspace, given the potential to significantly reduce the computational cost.

– **High-order Runge-Kutta (HORK):** Runge-Kutta methods are extensively used for solving differential equations Butcher [1996], and also in combination with exponential integrator schemes [Crouseilles et al., 2020, Lawson, 1967]These methods are naturally extended to high-order schemes. They can be explicit and are easy to implement. For this research, we adopt the Runge-Kutta algorithm of arbitrary order proposed by Gottlieb and Gottlieb [2003], defined by the relation

$$\begin{aligned}
\boldsymbol{k}_0 &= \boldsymbol{u}^n \\
\boldsymbol{k}_i &= \left(\boldsymbol{I}_{n\times n} + \Delta t\boldsymbol{H}\right)\boldsymbol{k}_{i-1}, \quad i = 1\ldots m-1 \\
\boldsymbol{k}_m &= \sum_{i=0}^{m-2} \lambda_i \boldsymbol{k}_i + \lambda_{m-1}\left(\boldsymbol{I}_{n\times n} + \Delta t\boldsymbol{H}\right)\boldsymbol{k}_{m-1} \\
\boldsymbol{u}^{n+1} &= \boldsymbol{k}_m,
\end{aligned}$$

where λ_i are the coefficients of the Runge-Kutta and have a straightforward computation. According to Gottlieb and Gottlieb [2003], the Runge-Kutta method exhibits strong stability-preserving properties if the coefficients λ_i are non-negative.

3.3 Computational cost and memory usage

In addition to the accuracy of the numerical solution when discussing the different approaches, we are also interested in their resource consumption. Specifically, we focus on the computational operations required by each algorithm and their utilization of computational memory.

Determining the exact number of computations performed by these methods is a complex task, further complicated by the fact that sparse matrix-vector multiplications are known to be bandwidth-limited in terms of performance Alappat et al. [2022], Huber et al. [2020]. Therefore, we adopt a simplified model that focuses exclusively on counting the loading and storing of elements. We consider only the matrix-vector operations, as the other vector operations introduce, at most, small variations in the number of operations. Consequently, the cost of each method by time step will be its number of stages or matrix-vector operations (MVOs). Therefore, the overall number of MVOs of a method for computing the solution up to a fixed time T and using a time step size Δt can be expressed as:

$$\mathrm{N_{op}} = \#\mathrm{MVOs}\frac{T}{\Delta t} = \frac{\#\mathrm{MOVs}}{\Delta t}T,$$

where the value of T can be disregarded when comparing the methods since it remains constant within a numerical experiment.

Memory consumption becomes a critical factor when solving the three-dimensional wave equation for seismic imaging applications. The primary concern is for the inverse problem, where the solution for each time step must be stored to be accessed later. Therefore, the number of time steps required for each method

$$N_{\mathrm{mem}} = \frac{T}{\Delta t},$$

is also an important variable that we will take into account afterward.

4 Analysis on homogeneous media

A common challenge arises when utilizing finite difference methods to solve wave equations due to numerical dispersion and dissipation. Numerical dispersion occurs when phase velocities depend on the frequency, leading to distortions in wave signals. On the other hand, numerical dissipation is associated with wave amplitude and is responsible for the emergence of high-frequency waves with small amplitudes in finite difference methods (Section 5.1 of Strikwerda [2004]).

Since the continuous wave equation is non-dispersive and non-dissipative, it is essential to ensure that the numerical methods used to solve it do not introduce excessive dispersion and dissipation. In seismic imaging problems, these issues can lead to significant inaccuracies in estimating the velocity field.

Therefore, special attention must be given to identifying and mitigating these errors.

In this section, we conduct a comparative analysis of the methods introduced in Section 3 within the context of a homogeneous velocity field and a single wave signal. We focus on evaluating their dispersion and dissipation errors and examining how these errors depend on the choice of time-step size.

4.1 Numerical dispersion and dissipation by Fourier transform

Our analysis investigates numerical dispersion and dissipation by quantifying variations in phase velocities of numerical approximations concerning a reference solution. To achieve this, we conduct a comparison in the frequency domain and estimate velocity changes for each frequency. For this analysis, a Fourier transform is applied to the solution, consisting of a single signal of a Ricker wavelet [Harold, 1994]. Consequently, we consider a homogeneous medium with a source point and a receiver (a spatial position where the signal is recorded over time).

Let $\mathcal{F}_{\text{appr}}(\omega)$ and $\mathcal{F}_{\text{ref}}(\omega)$ denote the Fourier transforms of the approximated and reference signals, respectively, with ω representing the frequency. Thus, we establish the relationship as follows:

$$\mathcal{F}_{\text{ref}}(\omega) = e^{k(\omega)+il(\omega)}\mathcal{F}_{\text{appr}}(\omega),$$

where the real functions $k(\omega)$ and $l(\omega)$ account for the numerical dissipation and dispersion errors, respectively, present in the approximated solution.

It is important to note that minimizing dissipation and dispersion errors hinges upon the extent to which the functions $k(\omega)$ and $l(\omega)$ approaches zero. As the numerical solution is computed at a finite number of time instants, ω is also limited to a finite range. Then, we calculate the mean of the absolute values of $k(\omega)$ and $l(\omega)$, which can be considered an approximation of the integral of their absolute values. Hereafter, we refer to these metrics as the dissipation and dispersion error. Furthermore, to mitigate potential numerical errors arising from divisions by small quantities during the computation of dispersion and dissipation errors, we exclusively consider frequencies where the amplitudes in the reference or approximated solutions surpass 1% of the peak amplitude of the reference solution.

In the next section, we will outline the numerical features of the Ricker signal experiment. Following that, in the subsequent two sections, we will apply the criteria discussed here to assess the numerical dissipation and dispersion errors.

4.2 Single signal experiment

The numerical solutions for wave propagation equations are computed in the homogeneous medium $\Omega = [0\text{km}, 6\text{km}] \times [0\text{km}, 5\text{km}]$, with a velocity $c = 3\text{km/s}$. A Ricker source is placed at position $(3\text{km}, 4.99\text{km})$ (with a delay of $t_0 = 0.18\text{s}$), and a receiver is positioned at $(3\text{km}, 2.5\text{km})$. The time integration is carried out until $T = 1.3\text{s}$ without applying any absorbing boundary conditions, as the reflections at the boundary have not yet reached the receiver by the final time. The spatial discretization size used for numerical solutions of the methods is $\Delta x = 10\text{m}$, while the reference solution is computed with $\Delta x = 2.5\text{m}$ and $\Delta t = 0.104\text{ms}$ using the RK9-7 scheme.

We are mainly interested in the largest time step allowed such that the error of the methods is under a fixed threshold. However, to ensure uniform wave sampling of the numerical approximations at the receiver, we use larger time steps up to the point when the wave closely approaches the receiver ($t = 0.6\text{s}$). Then, a uniform $\Delta t = 0.417\text{ms}$ is employed until the final time $T = 1.3\text{s}$ is reached. Figure 2 displays the homogeneous medium with the source and the receiver positions and the snapshots of the reference solution at times $t = 0.6s$ and $T = 1.3s$.

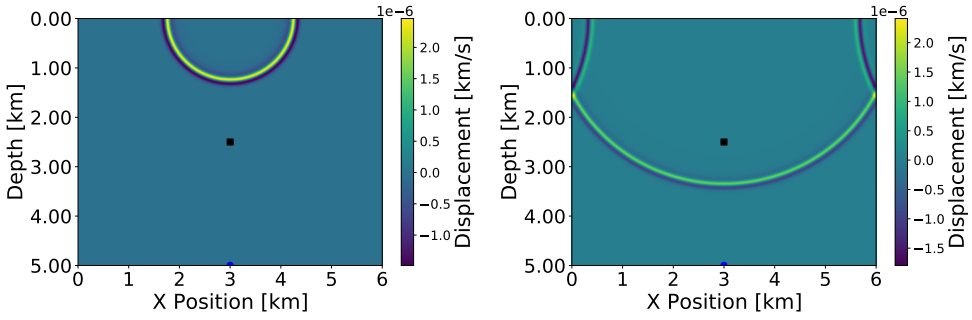

(a) Wave propagation at time $t = 0.6s$. (b) Wave propagation at time $T = 1.3s$.

Fig. 2: Snapshots of the reference solution at times $t = 0.6s$ and $T = 1.3s$ within the homogeneous medium $\Omega = [0\text{km}, 6\text{km}] \times [0\text{km}, 5\text{km}]$. The Ricker signal source position (blue dot) and the receiver location (black square) are highlighted. During the time interval $t \in [0.6, 1.3]s$, the front wave propagates through the receiver location.

Although our primary focus lies in evaluating the time error of the methods, it is essential to acknowledge the influence of spatial discretization on numerical accuracy. To account for this spatial effect, convergence, dispersion, and dissipation are computed for all methods with a small time-step, $\Delta t = 0.417\text{ms}$ (see Figure 10 in Appendix A.2). The minimum convergence, dispersion, and dissipation errors obtained from this computation serve as an

estimation of the spatial effect. Then, we determine the maximum Δt allowable for the methods such that the time error remains less or equal to 50% of the spatial error.

For this experiment, the approximation error due to the spatial discretization is approximately $3.9 \cdot 10^{-6}$ (see Figure 10 in Section A.2). Based on this, we determine $\Delta t_{\max}$ as the maximum Δt such that the approximation error is less or equal to $E_{\text{rr}} = 5.9 \cdot 10^{-6}$. Then, the convergence can be analyzed by investigating the signal error at a specific receiver location $(3\text{km}, 2.5\text{km})$. It becomes clear that an increase in the number of stages leads to an increase in $\Delta t_{\max}$ (see Figure 3).

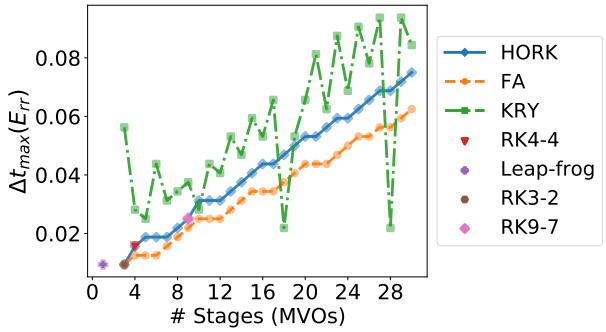

Fig. 3: Dependence of $\Delta t_{\max}$ on the approximation degree of the numerical scheme. A higher number of stages leads to an increase in the maximum allowable time step without significantly increasing the number of computations.

Referring to Figure 3, it can be observed that the Krylov method displays a highly oscillatory pattern concerning its associated $\Delta t_{\max}$. Intriguingly, this pattern reaches its local peak values when the subspace dimension is an odd number. The general behavior of the methods convergence is not sensible to the cutting point of the error threshold, and for variations of $E_{\text{rr}} = 5.9 \cdot 10^{-6}$, they remain valid. So, we expect a similar behavior when studying the dispersion and dissipation.

4.3 Dispersion results

The dispersion error arising from spatial discretization is estimated as 0.002. Consequently, we permit for the time integrator methods an error threshold of 1.5× higher, equating to a maximum allowable dispersion error of 0.003. Then, we search for $\Delta t_{\max}$ such that the dispersion error remains below this limit.

In addition to $\Delta t_{\max}$, we introduce a computational cost measure denoted as $\text{N}_{\text{op}}^{\text{disp}}$, similar to the ideas of Section 3.3, defined as:

$$\mathrm{N}_{\mathrm{op}}^{\mathrm{disp}} = \frac{\#\ \mathrm{MVOs}}{\Delta t_{\max}}.$$

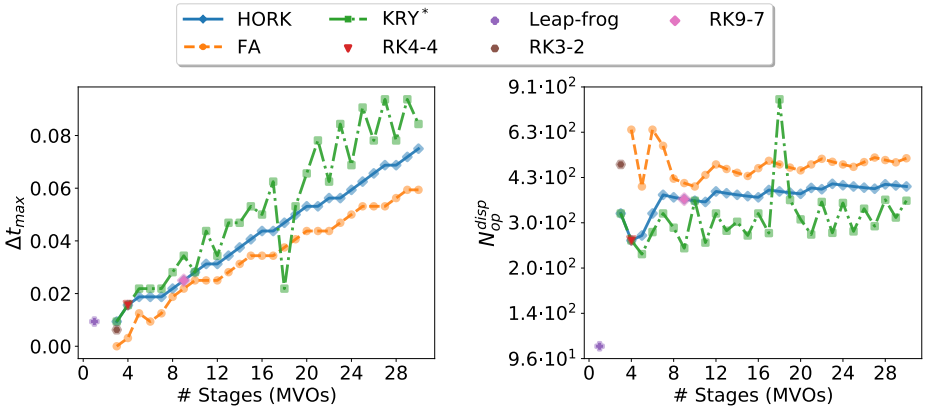

(a) Maximum time-step, $\Delta t_{\max}$. (b) Number of MVOs by $\Delta t_{\max}$.

Fig. 4: Variation of $\Delta t_{\max}$ (left) and $\mathrm{N}_{\mathrm{op}}^{\mathrm{disp}}$ (right) concerning the numerical scheme and the number of stages utilized, according to the numerical dispersion error for a Ricker source peak frequency of $f_M = 15$Hz. Generally, a higher number of stages leads to an increase in the maximum allowable time step size without significantly increasing the number of computations. * Here we neglect the computational complexity of creating the Krylov subspaces.

Based on Fig. 4, the Leap-frog algorithm is approximately two times faster than the other schemes but requires small time steps. On the other hand, the explicit exponential methods exhibit an increase in their maximum time step as the number of stages used rises, without a significant increase in the number of matrix-vector operations required. Interestingly, the peak values of the Krylov methods for the largest Δt and the lower $\mathrm{N}_{\mathrm{op}}^{\mathrm{disp}}$ are consistently for the odd numbers of the subspace dimension 4.

To ensure the robustness of our analysis, we reproduce the previous results in Appendix A.2.1 using various peak frequencies of the Ricker source since wave frequencies influence dispersion.

4.4 Dissipation results

Similar to the previous section, we estimate the minimum dispersion error, independent of the time integrator used. The minimum dissipation error is approximately $2.4 \cdot 10^{-7}$. Thus, we once again compute the maximum time-step, $\Delta t_{\max}$, such that the dispersion error remains below $3.6 \cdot 10^{-7}$. Besides of $\Delta t_{\max}$, we define the computational cost measure as

$$\mathrm{N}_{\mathrm{op}}^{\mathrm{diss}} = \frac{\#\ \mathrm{MVOs}}{\Delta t_{\max}},$$

similar to convergence and dispersion.

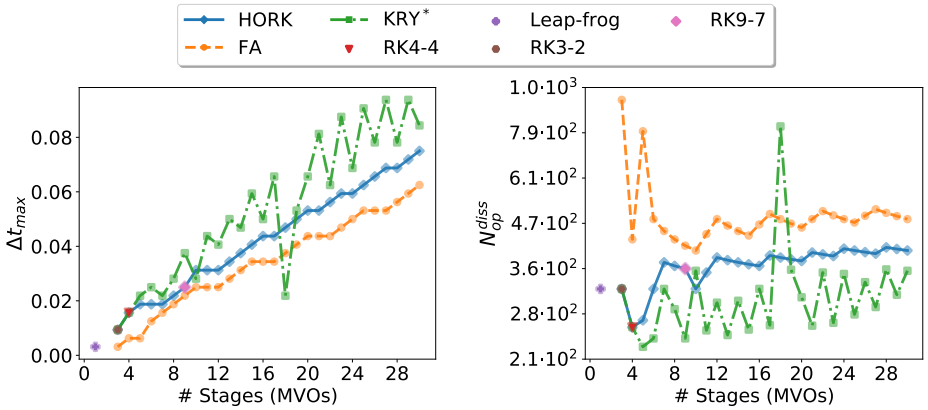

(a) Maximum time-step, $\Delta t_{\max}$.

(b) Number of MVOs by $\Delta t_{\max}$.

Fig. 5: Variation of $\Delta t_{\max}$ (left) and $\mathrm{N}_{\mathrm{op}}^{\mathrm{disp}}$ (right) concerning the numerical scheme and the number of stages utilized, according to the numerical dissipation error for a Ricker source peak frequency of $f_M = 15$Hz. Generally, a higher number of stages leads to an increase in the maximum allowable time step size without significantly increasing the number of computations. * Here we neglect the computational complexity of creating the Krylov subspaces.

In Figure 5, a similar trend is observed with the dispersion error, except that the performance of the exponential integrator is better in relation to the Leap-frog when comparing the dissipation error. Notably, the high-order methods display an increase in the time-step size with the number of stages used without significantly increasing the number of matrix-vector operations required.

As with the numerical dispersion, we reproduce the experiments for different Ricker source peak frequencies in Appendix (Section A.2.2).

5 Analysis on realistic seismic models

In this section, we describe the numerical experiments we will use to compare the accuracy of the approximations of the different methods. For comparison, we generated a reference solution using the RK9-7 scheme with a finer grid ($\Delta x = 5$m) and then estimated the error for each method using various time step sizes. To ensure a robust accuracy assessment, we employ two procedures. First, we compare the approximated solution across the entire physical space

(excluding the PML domain) at a specific time instant. Second, we compare the seismogram data of the solution values at the upper boundary for all the simulation time. For each error evaluation, we determine the maximum time step size, $\Delta t_{\max}$, that allows a scheme of a particular order to achieve a solution accuracy below a predefined threshold with the least number of MVOs. Additionally, we introduce an efficiency measure and an indicator of memory utilization derived from the number of MVOs and $\Delta t_{\max}$, following the concepts outlined in Section 3.3.

5.1 Test cases

We consider four numerical scenarios with different velocity fields (see Figure 6). The first is a synthetic example of a heterogeneous medium with high contrast velocities and a sharp corner. The second is a 2D slice of the velocity field of the Santos Basin[1] oil and gas exploration region. A 2D portion of Marmousi velocity field is the third example, and the final test is the 2D SEG/EAGE synthetic model.

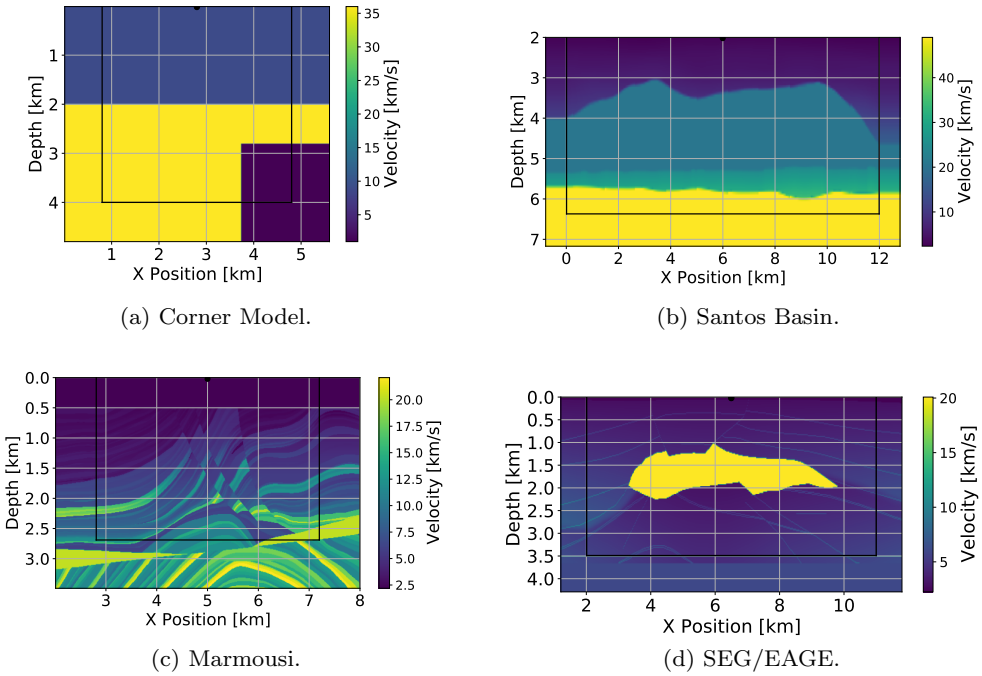

(a) Corner Model.

(b) Santos Basin.

(c) Marmousi.

(d) SEG/EAGE.

Fig. 6: Velocity fields of the test cases Corner Model, Santos Basin, Marmousi, and SEG/EAGE, used to study the numerical convergence.

[1] A typical velocity field of Santos Basin region, in Brazil.

In all the examples, we include a source and an arrangement of receivers near the surface of the medium. The specification of this construct and other parameters of the numerical simulations are specified in Table 1.

Test cases	**Corner Model**	**Santos Basin**
Domain dimensions	$\Omega = [0\text{km}, 4\text{km}] \times [0\text{km}, 4\text{km}]$	$\Omega = [0\text{km}, 12\text{km}] \times [2\text{km}, 6.4\text{km}]$
Simulation time	$T = 1.1\text{s}$	$T = 1.5\text{s}$
Source position	$(2\text{km}, 0.02\text{km})$	$(6\text{km}, 2.02\text{km})$
PML thickness (δ)	1.0km	0.8km
Test cases	**Marmousi**	**SEG/EAGE**
Domain dimensions	$\Omega = [2\text{km}, 8\text{km}] \times [0\text{km}, 3.5\text{km}]$	$\Omega = [2\text{km}, 11\text{km}] \times [0\text{km}, 3.5\text{km}]$
Simulation time	$T = 1.5\text{s}$	$T = 2\text{s}$
Source position	$(5\text{km}, 0.02\text{km})$	$(6.5\text{km}, 0.02\text{km})$
PML thickness (δ)	0.8km	0.8km

Table 1: Parameters of the four numerical simulations considered in this paper.

We save the solution at the upper boundary at each simulated time instant to construct the seismogram. We use a time span twice as long as specified in each experiment outlined in Table 1 to allow the reflected waves to reach the surface.

5.2 Maximum time-step

We need to calculate the maximum allowable time step, denoted as $\Delta t_{\max}$, for all time integration schemes. We initially consider the numerical error inherent to the spatial discretization in each numerical experiment (see Appendix A.3) since this error is independent of the time integration method. Next, we employ a tolerance level equivalent to 150% of the spatial discretization error in each experiment. Finally. we use that tolerance to compute the value of $\Delta t_{\max}$ for the numerical schemes described in Section 3.

We consider a spatial-step size of $\Delta x = 10m$ to compute the approximated solutions mentioned before. Figures 7 and 9 show the allowed $\Delta t_{\max}$ by all the methods for the numerical tests Corner Model, Santos Basin, Marmousi, and SEG/EAGE.

Figure 7 presents the maximum time step, $\Delta t_{\max}$, considering the spatial error of the solution at a time instant. Generally, when the approximation degree increases, we observe an increment in the allowed $\Delta t_{\max}$. Moreover,

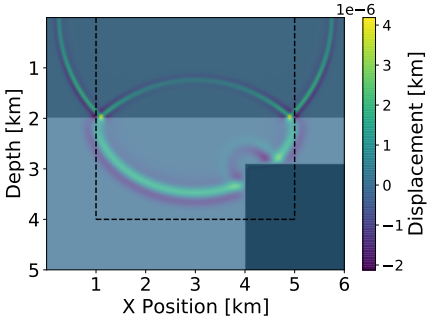

(a) Corner Model solution at time $T = 1.1s$.

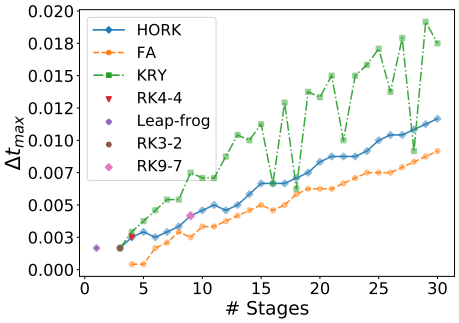

(b) Computing Δt_{max} for Corner Model using an error tolerance of $3.03 \cdot 10^{-7}$.

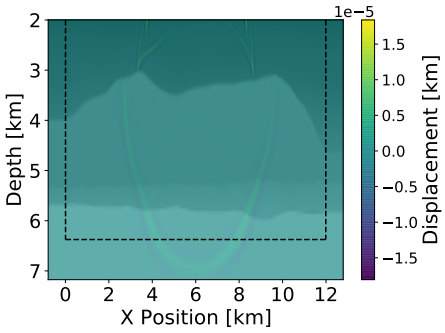

(c) Santos Basin solution at time $T = 1.5s$.

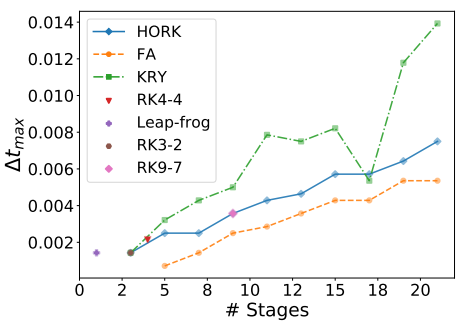

(d) Computing Δt_{max} for Santos Basin using an error tolerance of $8.33 \cdot 10^{-7}$.

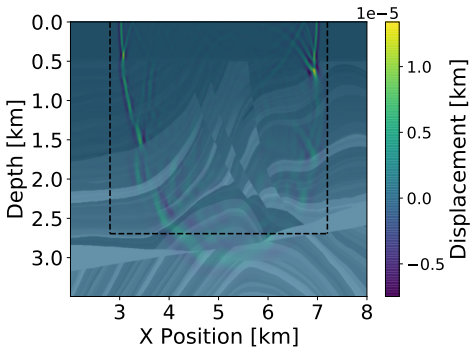

(e) Marmousi solution at time $T = 1.5s$.

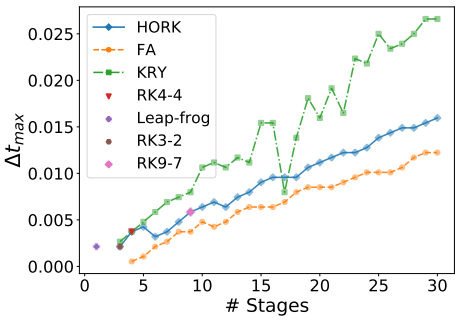

(f) Computing Δt_{max} for Marmousi using an error tolerance of $9.93 \cdot 10^{-7}$.

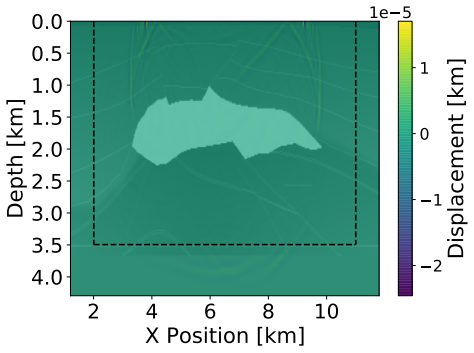

(g) SEG/EAGE solution at time $T = 2s$.

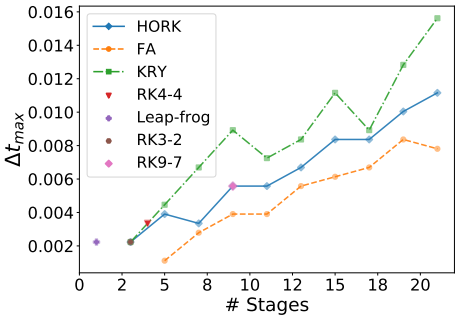

(h) Computing Δt_{max} for SEG/EAGE using an error tolerance of $1.3 \cdot 10^{-6}$.

Fig. 7: Snapshots of the reference solution for Corner Model, Santos Basin, Marmousi, and SEG/EAGE numerical tests (left column), and the Δt_{max} of each method such that the error with the reference solution is under a fixed threshold (right column). An increase in the number of stages of the method leads to a larger Δt_{max}.

the Krylov subspace approximation exhibits the largest time steps among the studied methods, followed by the other high-order methods. In contrast, low-order methods such as Leap-frog and RK3-2 require smaller time steps.

The determination of $\Delta t_{\max}$ based on the seismogram data is illustrated in Figure 9. Similar to Figure 7, an increase in the number of stages leads to a higher maximum time step. Notably, the Krylov subspace method consistently demonstrates the highest $\Delta t_{\max}$ values, followed by other high-order methods.

Based on the insights gained from Figures 7 and 9, we can conclude that the choice between using the error of the solution at a particular time instant or the seismogram data leads to similar values of $\Delta t_{\max}$ for the methods. Therefore, for the sake of simplicity, we estimate $\Delta t_{\max}$ with the error of the approximation in the physical domain at a specific time instant (as illustrated in Figure 7). Next, we estimate the computational efficiency and memory consumption of each method using the concepts of Section 3.3.

5.3 Computational efficiency and memory consumption

From the previous section, we concluded that using a method with a large number of stages allows an increase in the maximum time step such that we have a solution with good accuracy. However, it is unclear if increasing the number of stages to use a larger Δt reduces the number of operations or how it helps in utilizing the memory. To answer this question, we apply the ideas discussed in Section 3.3 and define the measure of computational efficiency

$$\mathrm{N}_{\mathrm{op}}^{\Delta t} = \frac{\#\ \mathrm{MVOs}}{\Delta t_{\max}},$$

and the indicator of memory consumption to store results for a backward propagation

$$\mathrm{N}_{\mathrm{mem}}^{\Delta t} = \frac{T}{\Delta t_{\max}},$$

where T is the simulation time defined by Table 1, for each numerical experiment.

Figure 8 illustrates the number of MVOs and the memory usage for all the methods when solving the Marmousi numerical example. The Leap-frog algorithm proves the most efficient among the tested methods. However, in terms of memory utilization, this method requires a substantial amount of memory. On the other hand, among the high-order methods, the Krylov subspace approximations demonstrate the best performance, even comparable to the Leap-Frog scheme. However, we would like to point out that we are using a simplified model that doesn't consider the creation of the Krylov subspaces. Nevertheless, we observe a significant decrease in the number of stored vectors for high-order methods in general. Additionally, we notice that further increases in the approximation degree have an attenuated effect in reducing memory utilization, which is negligible for degrees larger than 20.

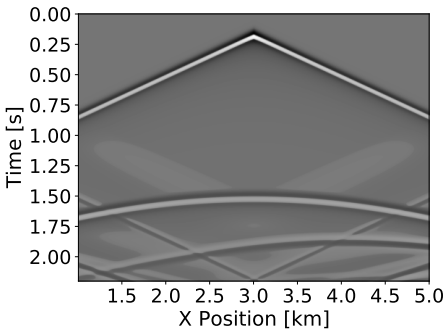

(a) Corner Model seismogram until time $T = 2.2s$.

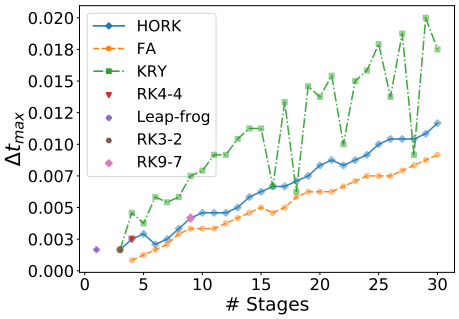

(b) Computing Δt_{max} for Corner Model using an error tolerance of $2.92 \cdot 10^{-7}$.

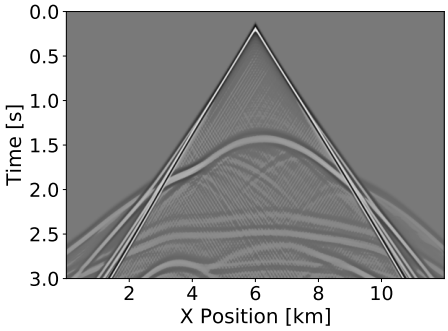

(c) Santos Basin seismogram until time $T = 3s$.

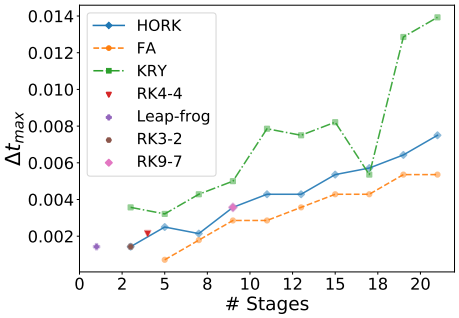

(d) Computing Δt_{max} for Santos Basin using an error tolerance of $2.65 \cdot 10^{-6}$.

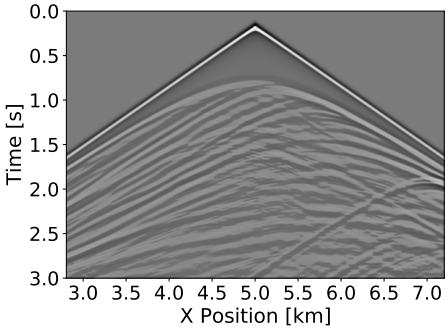

(e) Marmousi seismogram until time $T = 3s$.

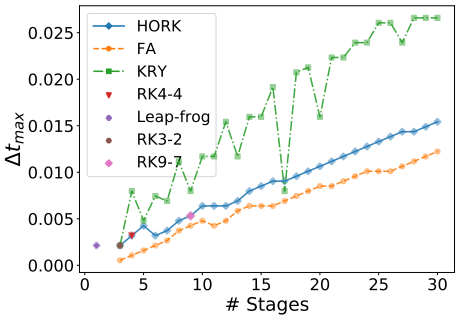

(f) Computing Δt_{max} for Marmousi using an error tolerance of $1.3 \cdot 10^{-6}$.

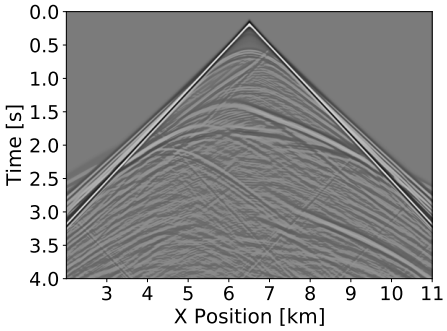

(g) SEG/EAGE seismogram until time $T = 4s$.

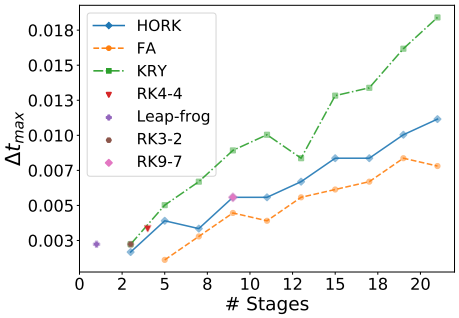

(h) Computing Δt_{max} for SEG/EAGE using an error tolerance of $4.2 \cdot 10^{-6}$.

Fig. 9: Seismogram of the reference solution for Corner Model, Santos Basin, Marmousi, and SEG/EAGE numerical tests (left column), and the corresponding Δt_{max} of each method, ensuring the error remains below a fixed threshold (right column). An increase in the number of stages of the method leads to a larger Δt_{max}.

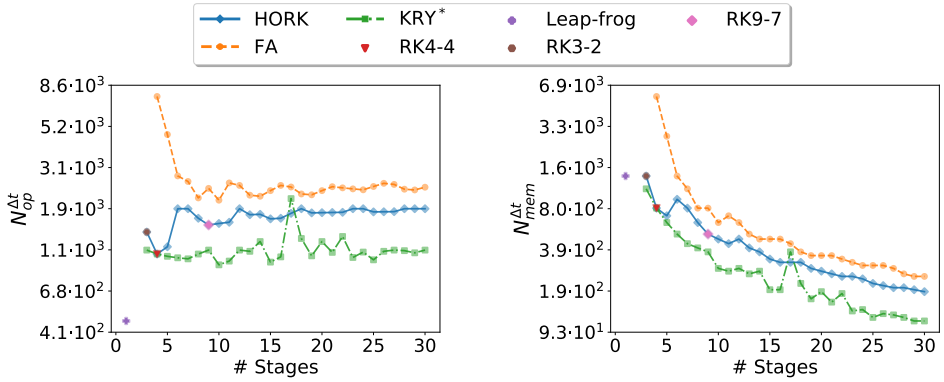

(a) Computational cost. (b) Memory utilization.

Fig. 8: Dependence of the number of MVOs and amount of stored solution vectors on the polynomial degree for the Marmousi numerical test. As the number of stages increases, the number of computations stabilizes, and memory usage decreases. * Here we neglect the computational complexity of creating the Krylov subspaces.

We observed similar behavior in the other numerical tests, and their corresponding graphs can be found in Appendix A.3.1.

6 Discussion

In this paper, we have implemented seven time-integration schemes, consisting of three arbitrary-order schemes based on exponential integrators and four classical low-order schemes. These algorithms have been compared through various numerical accuracy metrics, including stability, dispersion, and convergence. We have also studied the computational cost and memory requirements for each method across different approximation degrees.

The stability and dispersion analyses were conducted within a homogeneous domain by analyzing the Fourier transform of a single wave generated by a Ricker wavelet. We observed that the high-order methods were capable of using larger time steps as the polynomial degree increased. In general, we found that the Leap-frog method, although requiring smaller time steps, outperformed the high-order methods. Yet, when considering the dissipation error, the high-order methods displayed competitiveness and even surpassed all the low-order methods.

We conducted extensive tests to evaluate convergence using four distinct velocity fields: three realistic fields and one with sharp interfaces. We assessed the approximation error both in the physical space at a specific time instant and using seismogram data. Remarkably, our results proved consistent and robust across both types of errors and all four numerical experiments. Moreover,

the Krylov method presented the largest time step size in all the tests, resulting in the least amount of solution vectors required to save for the inverse problem. As a drawback, the Krylov method requires at each time instant to access as many vectors (with the dimensions of the solution of the wave equations) as stages of the method are used. This greatly hinders using the method to solve the direct problem. In general, high approximation degrees allowed for larger time steps, a finding that significantly impacts the number of saved vectors needed for solving the inverse problem. These results provide a different strategy to approach the memory challenges associated with the inverse problem.

This research addresses a gap in the existing literature, as most previous studies on high-order methods have predominantly focused on the spatial dimension Burman et al. [2022], Liu and Sen [2009], Weber et al. [2022], Wilcox et al. [2010]. Additionally, no prior work has comprehensively examined high-order exponential integrators in the context of the wave equation applied to seismic imaging, scrutinizing the performance across a wide range of approximation degrees. Nonetheless, we acknowledge that our implementation of high-order approximations using exponential integrators is naive. Substantial enhancements are possible, particularly in terms of implementing adaptive time-stepping strategies to mitigate the hump phenomena associated with the matrix exponential Moler and Van Loan [2003]. Indeed, adaptive algorithms have been proposed, such as the KIOPS algorithm for the Krylov subspace projections, which significantly outperforms the classical Krylov method used in our study.

Acknowledgements This research was carried out in association with the ongoing R&D project registered as ANP20714-2 STMI - Software Technologies for Modelling and Inversion, with applications in seismic imaging (USP/Shell Brasil/ANP). It was funded in part by the Coordenação de Aperfeiçoamento de Pessoal de Nível Superior - Brasil (CAPES) - Finance Code 001, and in part by Conselho Nacional de Desenvolvimento Científico e Tecnológico (CNPq) - Brasil. Fundação de Amparo à Pesquisa do Estado de São Paulo (FAPESP) grant 2021/06176-0 is also acknowledged.

It has also partially received funding from the Federal Ministry of Education and Research and the European High-Performance Computing Joint Undertaking (JU) under grant agreement No 955701, Time-X. The JU receives support from the European Union's Horizon 2020 research and innovation programme and Belgium, France, Germany, and Switzerland.

References

Acebron JA (2019) A monte carlo method for computing the action of a matrix exponential on a vector. Applied Mathematics and Computation 362:124545

Al-Mohy AH, Higham NJ (2010) A new scaling and squaring algorithm for the matrix exponential. SIAM Journal on Matrix Analysis and Applications 31(3):970–989

Al-Mohy AH, Higham NJ (2011) Computing the action of the matrix exponential, with an application to exponential integrators. SIAM journal on scientific computing 33(2):488–511

Alappat C, Hager G, Schenk O, Wellein G (2022) Level-based blocking for sparse matrices: Sparse matrix-power-vector multiplication. IEEE Transactions on Parallel and Distributed Systems 34(2):581–597

Alkhadhr S, Liu X, Almekkawy M (2021) Modeling of the forward wave propagation using physics-informed neural networks. In: 2021 IEEE International Ultrasonics Symposium (IUS), IEEE, pp 1–4

Alonso JM, Ibáñez J, Defez E, Alonso-Jordá P (2023) Euler polynomials for the matrix exponential approximation. Journal of Computational and Applied Mathematics 425:115074

Assi H, Cobbold RS (2017) Compact second-order time-domain perfectly matched layer formulation for elastic wave propagation in two dimensions. Mathematics and Mechanics of Solids 22(1):20–37

Bader P, Blanes S, Casas F (2019) Computing the matrix exponential with an optimized taylor polynomial approximation. Mathematics 7(12):1174

Bergamaschi L, Vianello M (2000) Efficient computation of the exponential operator for large, sparse, symmetric matrices. Numerical linear algebra with applications 7(1):27–45

Bergamaschi L, Caliari M, Vianello M (2004) The relpm exponential integrator for fe discretizations of advection-diffusion equations. In: International Conference on Computational Science, Springer, pp 434–442

Brachet M, Debreu L, Eldred C (2022) Comparison of exponential integrators and traditional time integration schemes for the shallow water equations. Applied Numerical Mathematics

Burden RL, Faires JD, Burden AM (2015) Numerical analysis. Cengage learning

Burman E, Duran O, Ern A (2022) Hybrid high-order methods for the acoustic wave equation in the time domain. Communications on Applied Mathematics and Computation 4(2):597–633

Butcher JC (1996) A history of runge-kutta methods. Applied numerical mathematics 20(3):247–260

Calvo M, Franco J, Montijano J, Rández L (1996) Explicit runge-kutta methods for initial value problems with oscillating solutions. Journal of computational and applied mathematics 76(1-2):195–212

Chern A (2019) A reflectionless discrete perfectly matched layer. Journal of Computational Physics 381:91–109

Cohen D, Dujardin G (2017) Exponential integrators for nonlinear schrödinger equations with white noise dispersion. Stochastics and Partial Differential Equations: Analysis and Computations 5(4):592–613

Crouseilles N, Einkemmer L, Massot J (2020) Exponential methods for solving hyperbolic problems with application to collisionless kinetic equations. Journal of Computational Physics 420:109688

Deka PJ, Einkemmer L, Tokman M (2023) Lexint: Package for exponential integrators employing leja interpolation. SoftwareX 21:101302

Fornberg B (1988) Generation of finite difference formulas on arbitrarily spaced grids. Mathematics of computation 51(184):699–706

Gallopoulos E, Saad Y (1992) Efficient solution of parabolic equations by krylov approximation methods. SIAM journal on scientific and statistical computing 13(5):1236–1264

Gaudreault S, Rainwater G, Tokman M (2021) Kiops: A fast adaptive krylov subspace solver for exponential integrators (vol 372, pg 236, 2018). JOURNAL OF COMPUTATIONAL PHYSICS 441

Gottlieb S, Gottlieb LAJ (2003) Strong stability preserving properties of runge–kutta time discretization methods for linear constant coefficient operators. Journal of Scientific Computing 18(1):83–109

Harold R (1994) Ricker, ormsby, klander, butterworth – a choice of wavelets. Hi-Res Geoconsulting 19(7):8–9

Hochbruck M, Ostermann A (2010) Exponential integrators. Acta Numerica 19:209–286

Huber D, Schreiber M, Yang D, Schulz M (2020) Cache-aware matrix polynomials. In: Computational Science–ICCS 2020: 20th International Conference, Amsterdam, The Netherlands, June 3–5, 2020, Proceedings, Part I 20, Springer, pp 132–146

Ikelle LT, Amundsen L (2018) Introduction to petroleum seismology. Society of Exploration Geophysicists

Iyiola OS, Wade BA (2018) Exponential integrator methods for systems of non-linear space-fractional models with super-diffusion processes in pattern formation. Computers & Mathematics with Applications 75(10):3719–3736

Jing H, Chen Y, Wang J, Xue W (2019) A highly efficient time-space-domain optimized method with lax-wendroff type time discretization for the scalar wave equation. Journal of Computational Physics 393:1–28

Kole J (2003) Solving seismic wave propagation in elastic media using the matrix exponential approach. Wave Motion 38(4):279–293

Kosloff D, FILHO AQ, TESSMER E, BEHLE A (1989) Numerical solution of the acoustic and elastic wave equations by a new rapid expansion method 1. Geophysical prospecting 37(4):383–394

Kristek J, Moczo P, Archuleta RJ (2002) Efficient methods to simulate planar free surface in the 3d 4th-order staggered-grid finite-difference schemes. Studia Geophysica et Geodaetica 46:355–381

Kwon SB, Bathe KJ, Noh G (2020) An analysis of implicit time integration schemes for wave propagations. Computers & Structures 230:106188

Lawson JD (1967) Generalized runge-kutta processes for stable systems with large lipschitz constants. SIAM Journal on Numerical Analysis 4(3):372–380

Lee JH (2023) Consistent transmitting boundaries for time-domain analyses of wave propagation in layered anisotropic waveguides. International Journal for Numerical Methods in Engineering 124(8):1883–1907

Li K, Liao W (2020) An efficient and high accuracy finite-difference scheme for the acoustic wave equation in 3d heterogeneous media. Journal of Computational Science 40:101063

Liu Y, Sen MK (2009) A new time-space domain high-order finite-difference method for the acoustic wave equation. Journal of computational Physics 228(23):8779–8806

Loffeld J, Tokman M (2013) Comparative performance of exponential, implicit, and explicit integrators for stiff systems of odes. Journal of Computational and Applied Mathematics 241:45–67

Lu YY (2003) Computing a matrix function for exponential integrators. Journal of computational and applied mathematics 161(1):203–216

Miao Z, Zhang J (2022) Optimizing finite-difference scheme in multidirections on rectangular grids based on the minimum norm. Geophysics 87(4):F41–F54

Moczo P, Kristek J, Halada L (2000) 3d fourth-order staggered-grid finite-difference schemes: Stability and grid dispersion. Bulletin of the Seismological Society of America 90(3):587–603

Moler C, Van Loan C (2003) Nineteen dubious ways to compute the exponential of a matrix, twenty-five years later. SIAM review 45(1):3–49

Mossaiby F, Ghaderian M, Rossi R (2015) Implementation of a generalized exponential basis functions method for linear and non-linear problems. International Journal for Numerical Methods in Engineering 105:221–240

Niesen J, Wright W (2009) A krylov subspace algorithm for evaluating the φ-functions in exponential integrators. arXiv preprint arXiv:09074631

Peixoto PS, Schreiber M (2019) Semi-lagrangian exponential integration with application to the rotating shallow water equations. SIAM Journal on Scientific Computing 41(5):B903–B928

Pototschnig M, Niegemann J, Tkeshelashvili L, Busch K (2009) Time-domain simulations of the nonlinear maxwell equations using operator-exponential methods. IEEE Transactions on Antennas and Propagation 57(2):475–483

Ravelo F SM Peixoto P (2023) An explicit exponential integrator based on faber polynomials and its application to seismic wave modeling. Journal of Scientific Computing -(-):(Accepted)

Robertsson JO, Blanch JO (2020) Numerical methods, finite difference. Encyclopedia of solid earth geophysics pp 1–9

Ruud B, Hestholm S (2001) 2d surface topography boundary conditions in seismic wave modelling. Geophysical Prospecting 49(4):445–460

Schmelzer T, Trefethen L (2006) Evaluating matrix functions for exponential integrators via carathéodory-fejér approximation and contour integrals

Schreiber M, Schaeffer N, Loft R (2019) Exponential integrators with parallel-in-time rational approximations for the shallow-water equations on the rotating sphere. Parallel Computing 85:56–65

Sidje RB (1998) Expokit: A software package for computing matrix exponentials. ACM Transactions on Mathematical Software (TOMS) 24(1):130–156

Strikwerda JC (2004) Finite difference schemes and partial differential equations. SIAM

Tago J, Cruz-Atienza V, Chaljub E, Brossier R, Coutant O, Garambois S, Prieux V, Operto S, Mercerat D, Virieux J, et al. (2012) Modelling seismic wave propagation for geophysical imaging. In: Seismic waves-research and analysis, IntechOpen

Tal-Ezer H, Kosloff D, Koren Z (1987) An accurate scheme for seismic forward modelling. Geophysical Prospecting 35(5):479–490

Tessmer E (2011) Using the rapid expansion method for accurate time-stepping in modeling and reverse-time migration. Geophysics 76(4):S177–S185

Thomas JW (2013) Numerical partial differential equations: finite difference methods, vol 22. Springer Science & Business Media

Walters S, Forbes L, Reading A (2020) Analytic and numerical solutions to the seismic wave equation in continuous media. Proceedings of the Royal Society A 476(2243):20200636

Weber I, Kreiss G, Nazarov M (2022) Stability analysis of high order methods for the wave equation. Journal of Computational and Applied Mathematics 404:113900

Wilcox LC, Stadler G, Burstedde C, Ghattas O (2010) A high-order discontinuous galerkin method for wave propagation through coupled elastic–acoustic media. Journal of Computational Physics 229(24):9373–9396

Zhang X, Yang D, Song G (2014) A nearly analytic exponential time difference method for solving 2d seismic wave equations. Earthquake Science 27(1):57–77

Zingg DW, Lomax H, Jurgens H (1996) High-accuracy finite-difference schemes for linear wave propagation. SIAM Journal on scientific Computing 17(2):328–346

A Appendix

A.1 Approximations at the free-surface

We present the finite difference approximations of 8th order for the required derivatives of the functions at the points near the free surface. To simplify the notation, we define $u_i = u(x, -i\Delta x)$, and $w_i = w_y\left(x, -(i+\frac{1}{2})\Delta x\right)$. Since we are considering a uniform grid, we have that $\Delta y = \Delta x$, and so, only Δx will be used.

$$\begin{aligned}
\frac{\partial^2 u}{\partial y^2}(x,0) &\approx \left(-\frac{3144919}{352800}u_0 + 16u_1 - 14u_2 + \frac{112}{9}u_3 - \frac{35}{4}u_4 + \frac{112}{25}u_5 - \frac{14}{9}u_6 + \frac{16}{49}u_7 \right.\\
&\quad \left. -\frac{1}{32}u_8\right)\frac{1}{\Delta x^2},\\
\frac{\partial^2 u}{\partial y^2}(x,-\Delta x) &\approx \left(\frac{271343}{156800}u_0 - \frac{1991}{630}u_1 + \frac{57}{40}u_2 + \frac{13}{60}u_3 - \frac{109}{288}u_4 + \frac{6}{25}u_5 - \frac{11}{120}u_6 \right.\\
&\quad \left. +\frac{179}{8820}u_7 - \frac{9}{4480}u_8\right)\frac{1}{\Delta x^2},\\
\frac{\partial^2 u}{\partial y^2}(x,-2\Delta x) &\approx \left(-\frac{18519}{78400}u_0 + \frac{58}{35}u_1 - \frac{251}{90}u_2 + \frac{22}{15}u_3 - \frac{1}{16}u_4 - \frac{14}{225}u_5 + \frac{1}{30}u_6 - \frac{2}{245}u_7 \right.\\
&\quad \left. +\frac{17}{20160}u_8\right)\frac{1}{\Delta x^2},\\
\frac{\partial^2 u}{\partial y^2}(x,-3\Delta x) &\approx \left(\frac{74801}{1411200}u_0 - \frac{37}{140}u_1 + \frac{67}{40}u_2 - \frac{263}{90}u_3 + \frac{53}{32}u_4 - \frac{23}{100}u_5 + \frac{13}{360}u_6 \right.\\
&\quad \left. -\frac{1}{245}u_7 + \frac{1}{4480}u_8\right)\frac{1}{\Delta x^2},\\
\frac{\partial u}{\partial y}\left(x,-\frac{1}{2}\Delta x\right) &\approx \left(\frac{5034629}{3763200}u_0 - \frac{23533}{15360}u_1 + \frac{4259}{15360}u_2 - \frac{1103}{9216}u_3 + \frac{151}{3072}u_4 - \frac{1171}{76800}u_5 \right.\\
&\quad \left. +\frac{139}{46080}u_6 - \frac{211}{752640}u_7\right)\frac{1}{\Delta x},\\
\frac{\partial u}{\partial y}\left(x,-\frac{3}{2}\Delta x\right) &\approx \left(-\frac{363509}{3763200}u_0 + \frac{6297}{5120}u_1 - \frac{6147}{5120}u_2 + \frac{211}{3072}u_3 + \frac{3}{1024}u_4 - \frac{153}{25600}u_5 \right.\\
&\quad \left. +\frac{29}{15360}u_6 - \frac{57}{250880}u_7\right)\frac{1}{\Delta x},\\
\frac{\partial u}{\partial y}\left(x,-\frac{5}{2}\Delta x\right) &\approx \left(\frac{4631}{250880}u_0 - \frac{305}{3072}u_1 + \frac{1245}{1024}u_2 - \frac{3725}{3072}u_3 + \frac{275}{3072}u_4 - \frac{69}{5120}u_5 + \frac{5}{3072}u_6 \right.\\
&\quad \left. -\frac{5}{50176}u_7\right)\frac{1}{\Delta x},
\end{aligned}$$

A.2 Homogeneous medium

This section complements the results in Section 4. First, we show the convergence, dispersion, and dissipation errors associated with the eighth-order spatial discretization scheme using $\Delta x = 10m$ (Figure 10). Additionally, we present how varying the peak frequencies as $f_M =$ 10, 15, 20, 25, impact the maximum allowable time-step $\Delta t_{\max}$ and the number of matrix-vector operations (MVOs) for different schemes and approximation degrees.

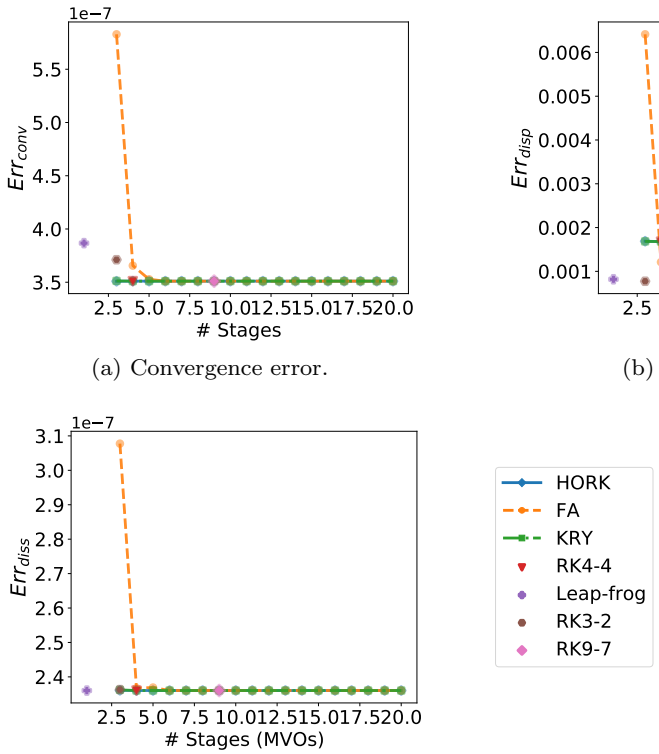

(a) Convergence error.

(b) Dispersion error.

(c) Dissipation error.

Fig. 10: Convergence, dispersion, and dissipation errors using the time-step $\Delta t = \frac{\Delta x}{8c}$ for different numerical methods, with a peak frequency of $f_M = 15$Hz. The approximation order does not matter, since there is an error associated to the spatial discretization.

A.2.1 Dispersion results

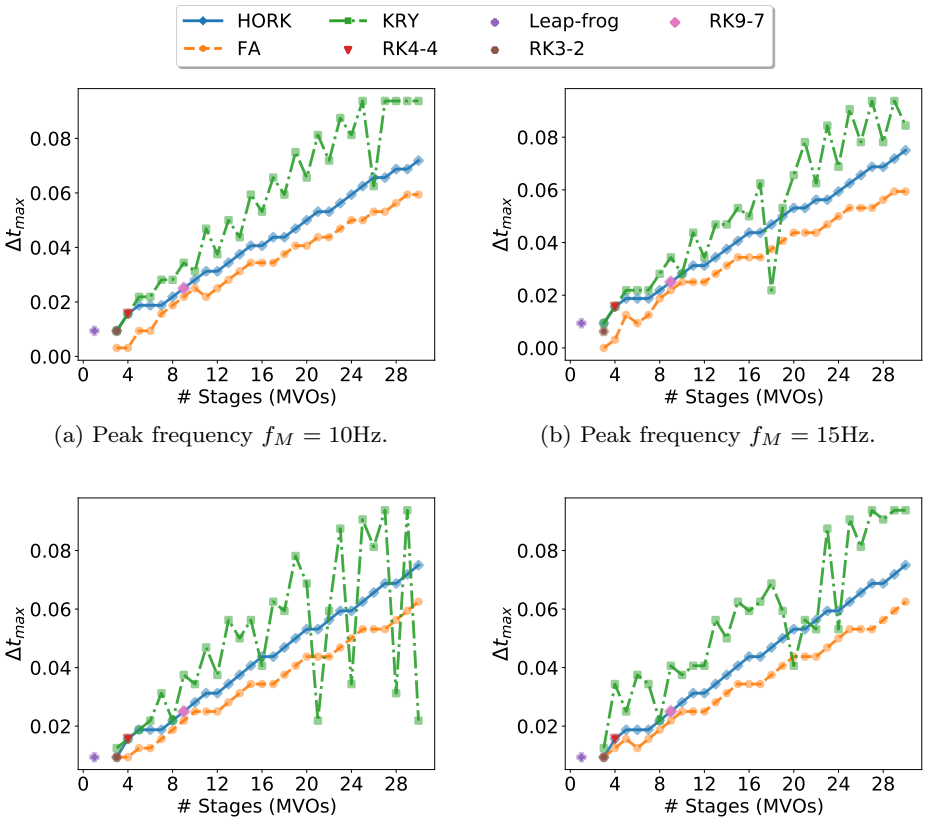

(a) Peak frequency $f_M = 10$Hz.

(b) Peak frequency $f_M = 15$Hz.

(c) Peak frequency $f_M = 20$Hz.

(d) Peak frequency $f_M = 25$Hz.

Fig. 11: Maximum time step ($\Delta t_{\max}$) while controlling the time dispersion error of each method to be below 50% of the spatial dispersion error concerning different peak frequencies of the Ricker wavelet. A grater number of stages generally allows larger time steps.

From Fig. 11, we perceive that the general behavior is maintained independent of the peak frequencies. With the difference that when the peak frequency increases, the results for the Krylov method are more oscillatory, and the high-degree approximations using Faber polynomials suffer from more round-off errors.

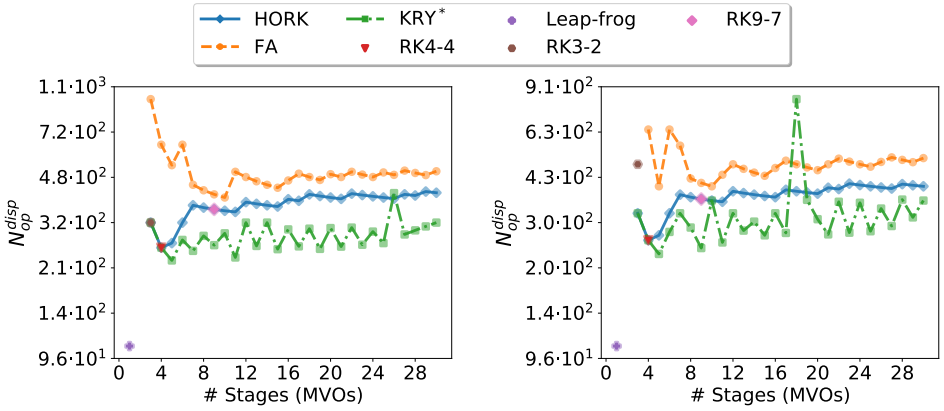

(a) Peak frequency $f_M = 10$Hz.

(b) Peak frequency $f_M = 15$Hz.

(c) Peak frequency $f_M = 20$Hz.

(d) Peak frequency $f_M = 25$Hz.

Fig. 12: Dependence of the number of matrix-vector operations and the maximum time-step required to compute the solution on the polynomial degree, considering different peak frequencies. While increasing the number of stages generally leads to a slight increment in computations. * Here we neglect the computational complexity of creating the Krylov subspaces.

In Figure 12, we still observe that the Leap-frog algorithm requires the least amount of MVOs. The FA and HORK methods share a similar number of computations independent of the peak frequency.

A.2.2 Dissipation results

A similar trend of Fig. 11 is observed in Figure 13, as with the dispersion error. The Krylov method still has the worst performance for the different peak frequencies. However, it is noteworthy that the RK9-7 method (red triangle) displays an even better performance concerning the dissipation error.

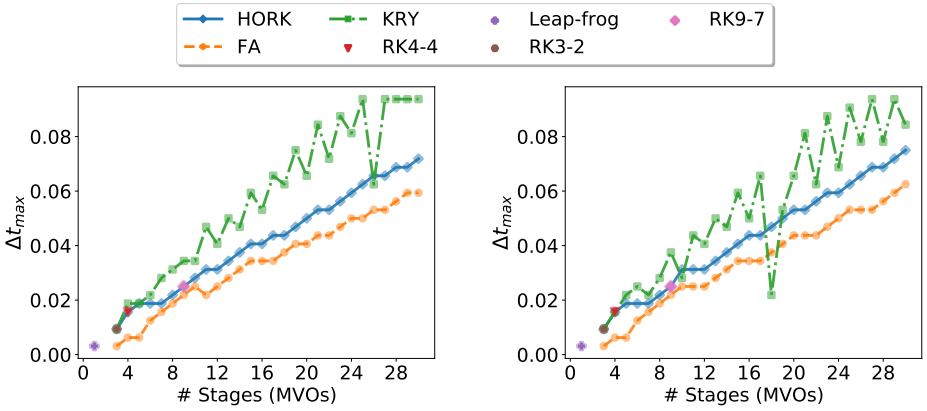

(a) Peak frequency $f_M = 10$Hz.

(b) Peak frequency $f_M = 15$Hz.

(c) Peak frequency $f_M = 20$Hz.

(d) Peak frequency $f_M = 25$Hz.

Fig. 13: Maximum time step such that the time dissipation error of each method is less than 50% of the spatial dispersion error for different peak frequencies of the Ricker wavelet. In general, more stages allow larger time steps, except for the Krylov method, where $\Delta t_{\max}$ reach a limit.

Regarding computational efficiency in the analysis of the dispersion error, the RK9-7 scheme still maintains an efficient computational performance. The FA and HORK exhibit similar behavior among the high-order methods, with a decline in efficiency for high-order Faber polynomials as the peak frequency increases. Nonetheless, the Krylov method exhibits the best performance in general, but with a very marked oscillatory behavior.

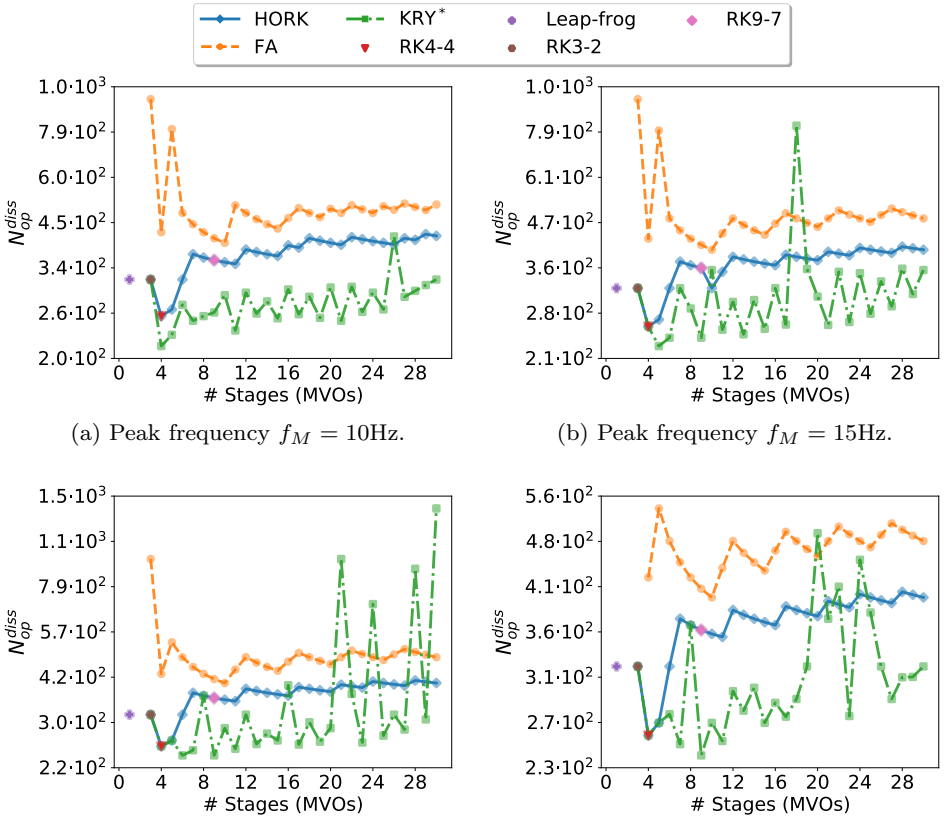

(a) Peak frequency $f_M = 10$Hz.

(b) Peak frequency $f_M = 15$Hz.

(c) Peak frequency $f_M = 20$Hz.

(d) Peak frequency $f_M = 25$Hz.

Fig. 14: Dependence on the polynomial degree of the number of matrix-vector operations by maximum time-step required to compute the solution for different peak frequencies. When the number of stages increases, the number of computations increases slightly. * Here we neglect the computational complexity of creating the Krylov subspaces.

A.3 Convergence and computational efficiency

In this section, we complement the results of the numerical experiments of Section 5. First, we show the error graphics using the minimum time-step of $\Delta t = \frac{\Delta x}{8 c_{\max}}$, where $c_{\max}$ is the medium maximum velocity. These graphs account for all the methods discussed in Section 3 and several approximation degrees for the high-order schemes. Following that, we present the graphics of the estimation of $\Delta t_{\max}$, the computational efficiency, and the memory utilization.

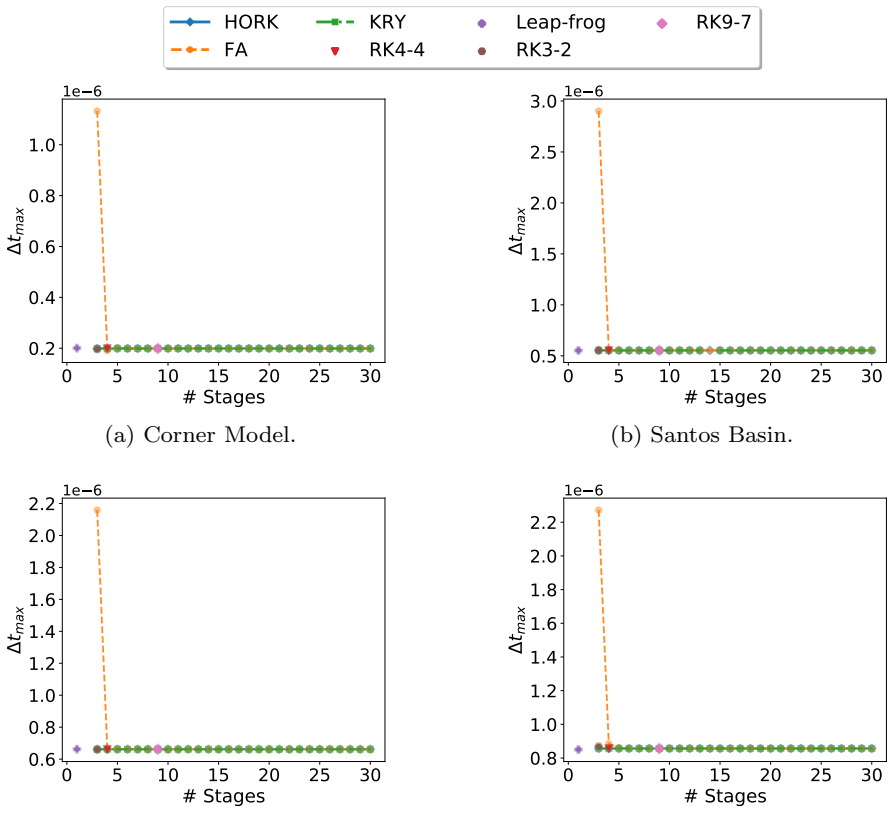

(a) Corner Model.

(b) Santos Basin.

(c) Marmousi.

(d) SEG/EAGE.

Fig. 15: Error at a time instant in the physical space achieved by each time integrator and several approximation degrees, for all the numerical experiments described in Section 5.1, using a time step size of $\Delta t = \frac{\Delta x}{8c_{\max}}$. Regardless of the order of the method, there is an inferior limit for the error due to spatial discretization step-size size and scheme.

Based on Figure 16, we observe an approximation error in all the numerical examples that do not decrease with the order of the method or with the selected method. This error is independent of the time integration strategy and is produced by the spatial discretization operator. While the dependence of the spatial error on the numerical experiment is weak, it is important to estimate it accurately for a reliable computation of $\Delta_{\max}$, as quantified in Table 3.

Numerical experiment	Spatial error	Error tolerance
Corner Model	$2.02 \cdot 10^{-7}$	$3.03 \cdot 10^{-7}$
Santos Basin	$5.55 \cdot 10^{-7}$	$8.33 \cdot 10^{-7}$
Marmousi	$6.62 \cdot 10^{-7}$	$9.93 \cdot 10^{-7}$
SEG/EAGE	$8.65 \cdot 10^{-7}$	$1.3 \cdot 10^{-6}$

Table 2: Numerical error at a time instant in the physical domain produced by the spatial discretization.

Table 3 contains two key columns of information. The first column, labeled "Spatial error", represents the error stemming from the spatial discretization. Meanwhile, the second column, labeled "Error tolerance", accounts for the error tolerance of 150% of the spatial error we defined for the numerical experiment.

For the minimum error using the seismogram data, we have the respective error graphics and tolerance for each numerical test.

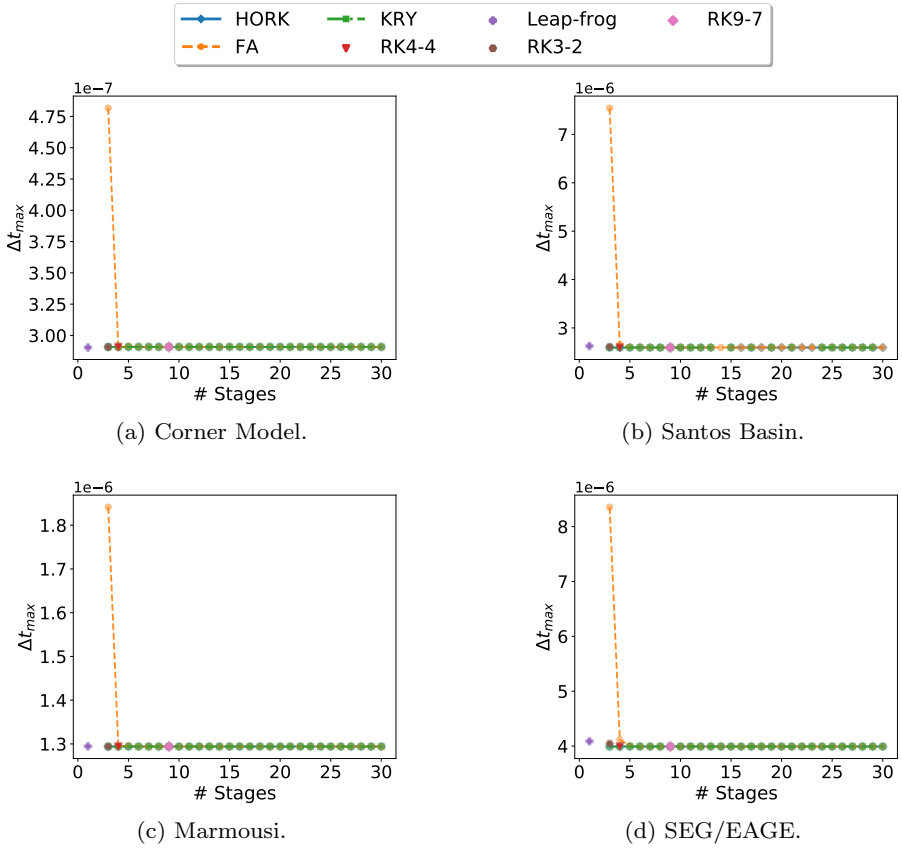

(a) Corner Model.

(b) Santos Basin.

(c) Marmousi.

(d) SEG/EAGE.

Fig. 16: Error using the seismogram data achieved by each time integrator and several approximation degrees, for all the numerical experiments described in Section 5.1, using a time step size of $\Delta t = \frac{\Delta x}{8c_{\max}}$. Regardless of the order of the method, there is an inferior limit for the error due to spatial discretization step-size size and scheme.

Numerical experiment	Spatial error	Error tolerance
Corner Model	$2.92 \cdot 10^{-7}$	$4.38 \cdot 10^{-7}$
Santos Basin	$2.65 \cdot 10^{-6}$	$3.97 \cdot 10^{-6}$
Marmousi	$1.3 \cdot 10^{-6}$	$1.95 \cdot 10^{-6}$
SEG/EAGE	$4.2 \cdot 10^{-6}$	$6.3 \cdot 10^{-6}$

Table 3: Numerical error utilizing the seismogram data produced by the spatial discretization.

A.3.1 Computational efficiency and memory consumption

Figure 17 displays each time the integrator's computational cost and memory utilization for the numerical tests Corner Model, Santos Basin, and SEG/EAGE. Although there are some variations between the experiments, the general behavior remains consistent. High-order methods require significantly less memory; in some cases, they are competitive with low-order methods, such as the Leap-Frog scheme.

The relationship between the number of MVOs and the quantity of stored solution vectors concerning the polynomial degree is illustrated for the Corner Model (first line), Santos Basin (second line), and SEG/EAGE (third line) numerical tests. As the number of stages increases, there is a stabilization in the number of computations, and memory usage decreases.

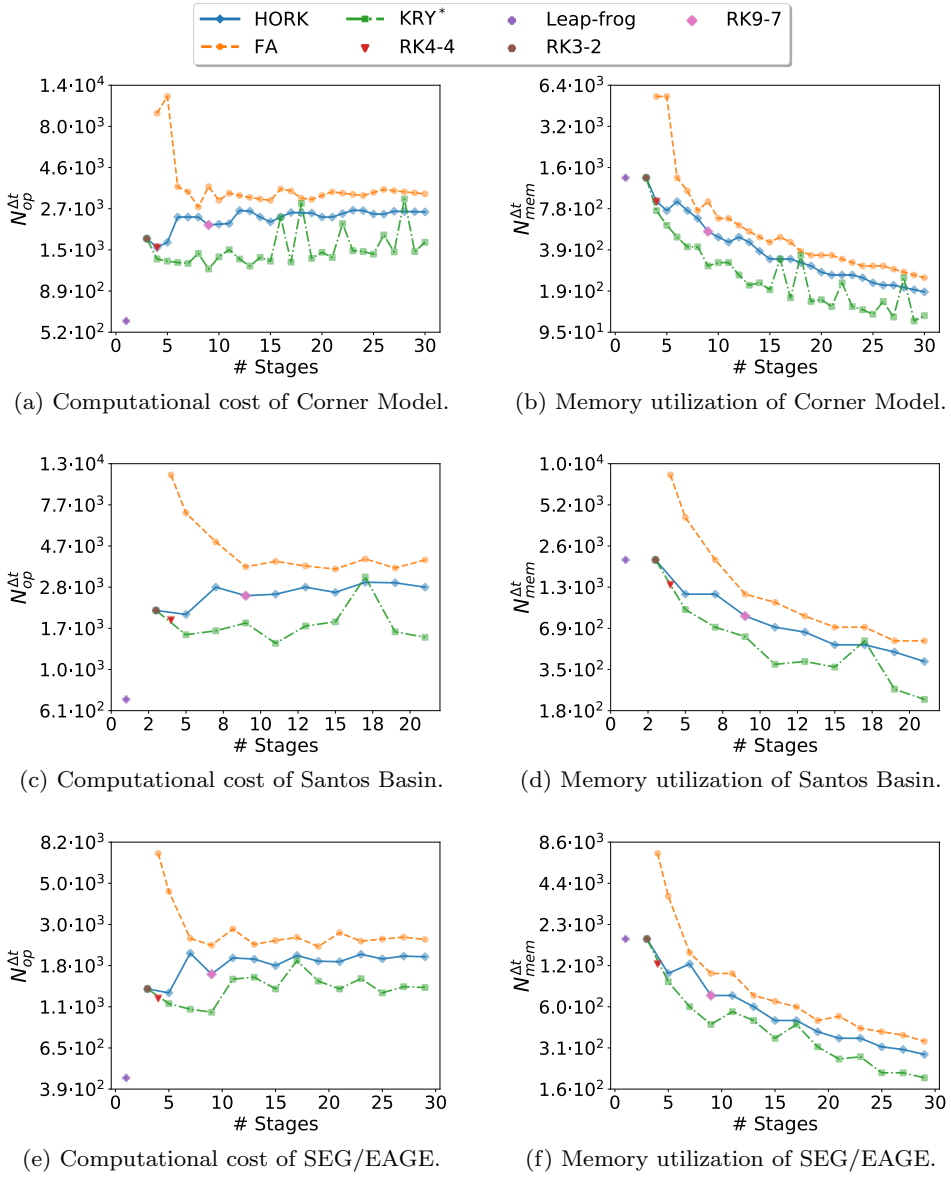

(a) Computational cost of Corner Model.

(b) Memory utilization of Corner Model.

(c) Computational cost of Santos Basin.

(d) Memory utilization of Santos Basin.

(e) Computational cost of SEG/EAGE.

(f) Memory utilization of SEG/EAGE.

Fig. 17: Dependence of the number of MVOs and amount of stored solution vectors on the polynomial degree, for the Corner Model (first line), Santos Basin (second line), and SEG/EAGE (third line) numerical tests. As the number of stages increases, the number of computations stabilizes, and memory usage decreases. * Here we neglect the computational complexity of creating the Krylov subspaces.

Chapter 4

A continuum model of a tumor growth for assessment of High-Energy Shock Waves therapy

As discussed in Chapter 1, wave propagation equations are present in a wide range of applications, and our focus has been on seismic imaging. However, exploring into a different direction, we introduce a novel biological application by developing a mechanical model of tumor growth subjected to High-Energy Shock Wave (HESW) therapy.

Given that HESW therapy involves the propagation of shock waves, the source term lacks smoothness, making it unsuitable for constructing an exponential integrator based on the derivatives over time of the source function. However, alternative strategies can be employed, such as utilizing a parallel approximation of the source function via an exponential integrator, similar to the approach outlined by (Tal-Ezer *et al.*, 1987; Kole, 2003; Tessmer, 2011).

The potential use of HESW as a treatment for growing tumors has been extensively investigated in biological experiments since the early 1990s. Despite its promising results in both *in vitro* and *in vivo* experiments, three decades later, HESW therapy is yet to be a standard clinical practice. We believe that this is partly due to the lack of a comprehensive understanding of the action of the therapy on tumors, which is crucial for optimising its efficiency while minimising intensity to prevent collateral damage to the surrounding tissues.

HESW therapy as an inherently mechanical in nature, as it consists of sharp pressure changes on the tissue. Thus, it is fundamental to investigate the impact of the pressure changes induced by HESW therapy on the volumetric stresses within the tumor and their subsequent effect on tumor growth. Addressing this question requires a mathematical model of a tumor rooted in continuum mechanics capable of simulating a mechanical therapy. Therefore, we developed a simple model within the framework of continuum mechanics, yet sophisticated enough to enhance our understanding the stress changes

within the tumor. Serving as a foundational step in the development of more complex models, with the aim of simulating more realistic treatment scenarios.

This chapter is intended for submission in the Journal of Applied Mathematical Modelling, co-authored with my advisor Pedro Peixoto and Reinaldo Rodrigues, an international collaborator. It is a self-contained unit, but has not been submitted yet due to the pending subsection that examines the comparison with experimental data.

RESEARCH ARTICLE - PRE-PRINT

A continuum model of tumor growth for assessment of High-Energy Shock Waves therapy

F. Valdés-Ravelo[a], R. Rodríguez-Ramos[b] and P. S. Peixoto[a]

[a]Instituto de Matemática e Estatística, Universidade de São Paulo, São Paulo, PC 05508-090, Brasil; [b]Facultad de Matemática y Computación, Universidad de La Habana, La Habana, PC 10400, Cuba.

ARTICLE HISTORY
Compiled April 1, 2024

ABSTRACT
The High Energy Shock Wave (HESW) therapy, commonly used in the treatment of fractured bones and disintegration of kidney stones, also plays an important role in tumor treatments in modern medicine. While experimental results reveal its effectiveness, the underlying mechanical properties still lack further understanding. Aiming to help in the comprehension and optimal use of the technique, we propose a mathematical model of the action of High Energy Shock Wave (HESW) therapy in a growing tumor surrounded by an external medium. The model is based on continuum mechanics, describing a simplified yet realistic modeling of the dynamic stresses encountered during tumor deformation. The goal is to assess the tumor response under the action of shock waves generated in the external medium. We conduct numerical experiments with different sets of parameters for the HESW therapy observing that shock waves indeed produce a change in the tumor growth, leading to some cases in a decrease of its size. Moreover, we identify parameters of the shock wave application that have considerable influence on the resulting tumor growth. Additionally, we conducted experiments using parameter values based on real experimental measures and validated the model with reported data from tumor growth *in vitro* experiments. We conclude that the model successfully incorporated the mechanical features of the HESW therapy, contributing to a deeper understanding of the therapy. This understanding could aid in further optimizing the application of HESW. Finally, the model is intended to serve as a basis for further developments with more complex combined therapies involving HESW therapy.

KEYWORDS
Mathematical model; continuum mechanics; cancer; linear elasticity; mechanical therapy; high-energy shock waves;

1. Introduction

In the field of cancer research, mathematical models serve as valuable tools for comprehending the intricate factors that govern tumor development [Watanabe et al. 2016; Deisboeck et al. 2009; Tabassum et al. 2019; Roose et al. 2007; Altrock et al. 2015]. These models aid in predicting potential disease outcomes by simulating scenarios in which alterations in specific elements lead to a reduction in tumor progression or, in some cases, even tumor regression. Such successful modifi-

CONTACT F. Valdés-Ravelo. Email: fernanvr@ime.usp.br

cations may lead to innovative anti-tumor therapies [Ribba et al. 2018; Yin et al. 2019].

High-Energy Shock Wave (HESW) therapy, also called Shock Wave Lithotripsy (SWL) [López-Marín et al. 2018], is an important technique in medicine, normally adopted for medical procedures in humans such as the disintegration of kidney stones and the treatment of fractured bones [Shrivastava and Kailash 2005]. In the final decades of the last century, *in vitro* and pre-clinics studies showed how the methodology can also be used for treatments of growing tumors [Russo et al. 1986; Hoshi et al. 1991; Nicolai et al. 1994; Wörle et al. 1994; Maruyama et al. 1995b]. Experimental findings have revealed a delay in tumor growth upon the application of HESW therapy, and when combined with chemotherapy, an even more significant delay in growth and even tumor regression have been observed [Gamarra et al. 1993a; Oosterhof et al. 1990a]. However, the precise mechanisms underlying this therapy remain not fully understood, and mathematical studies modelling and replicating its effects on tumors are scarce.

Various biological effects of shock wave therapy on tumor growth have been documented. For instance, it enhances cell membrane permeability [López-Marín et al. 2018; Li et al. 2018], improving the efficiency of chemotherapy [Wörle et al. 1994; Frairia et al. 2003; Serpe et al. 2011]. It also causes vascular destruction within the tumor, leading to necrosis in certain areas [Hoshi et al. 1991; Gamarra et al. 1993b]. Shock waves can also induce cellular damage, enhancing apoptosis [Russo et al. 1986], and lead to cellular death due to cavitation effects generated by the negative pressure following the positive shock front [Sansone et al. 2018]. Furthermore, pressure changes produced by the therapy can alter stresses within the tumor, potentially affecting cell proliferation [Steinhauser 2016]. These processes occur simultaneously, making it challenging to study each one individually. Therefore, mathematical models that encompass these factors are crucial for a comprehensive assessment of HESW therapy's effects. Ensuring a favorable cost-benefit trade-off is vital in practical HESW therapy applications to minimize collateral effects, such as damage to nearby tissues and organs, and to reduce the risk of metastasis [Nardi et al. 2004; Roerdink et al. 2017; Oosterhof et al. 1996]. This is particularly important for maintaining lower treatment intensities compared to other tumor therapies [Abdelhalim et al. 2018].

In its essence, HESW therapy is a change of pressure on the tissue. Therefore, it is essential to investigate the impact of pressure changes induced by HESW therapy on the volumetric stresses within the tumor and their effects on tumor growth. Addressing this question requires a mathematical model of a tumor rooted in continuum mechanics that can simulate the mechanical therapy involving shock waves. However, to the best of our knowledge, there has not been published researches on this specific subject. Nonetheless, related works, such as Ghasemi and Sivaloganathan [2020], have developed a mathematical model to simulate the effects of similar therapies involving high-intensity focused ultrasound (HIFU), consisting of compressions and rarefactions that propagates in the medium [Madersbacher and Marberger 2003]. However, the model is not mechanical, and so, it did not consider the stresses in the tumor. Nonetheless, the importance of the simulation of the stress-deformation relation in a growing tumor has been already highlighted in the review Steinhauser [2016] for assessing the HIFU therapy. HIFU therapy combines mechanical and thermal actions on tissue, and precise modeling requires the implementation of non-linear propagation laws [Canney et al. 2010]. In the framework of modeling HESW therapy

while taking into account the stress-deformation relations have been addressed by Fagnan et al. [2008]. They developed a computational model focused on investigating the stresses under the action of HESW in bones, considering complex geometries and fluid mechanics. In their research, although it is recognized that the propagation of shock waves lies in the theory of non-linear elasticity, for the case of the HESW treatment, the linear elasticity theory served as a valid approximation.

In this study, we simulate the application of High-Energy Shock Wave therapy on tumors. The mathematical model describes the effect of elastic shock wave propagation within an external medium surrounding an avascular tumor. Both the tumor and the external medium are treated as linear elastic materials, each governed by distinct systems of equations. The tumor is a material with the ability to alter its volume, displacing the external medium during its anisotropic growth. It is connected to the external medium by its boundary, with a perfect contact condition. The external medium is represented as a homogeneous and isotropic material, following Hooke's law in three dimensions. As a result, our model is grounded in linear elasticity theory. This arrangement creates a heterogeneous medium, allowing us to investigate the tumor material's response to HESW therapy.

Our objective is to explore the possible outcomes of the tumor evolution for different setups of the HESW treatment. Therefore, we conduct numerical experiments that involve varying the parameters of HESW therapy to assess their impact on tumor growth and volumetric stresses within the tumor. Although our model simplifies the realistic tumor treatment involving various techniques, it is sophisticated enough to enhance our understanding of one of the underlying mechanisms of HESW therapy: the stress changes within the tumor. It serves as a foundation for developing more complex, multi-technique models to emulate a more realistic treatment. One of the main challenges inherent to these mathematical models lies in acquiring the experimental data for the model parameters. In support of this endeavor, we also provide a concise summary of published data regarding the parameters necessary for a continuum mechanics-based tumor model, with standardized physical magnitudes, and the primary experimental layouts outlined in relevant references concerning HESW therapy in both *in vitro* and *in vivo* experiments.

In the following section, we describe the mathematical formulations of the tumor and HESW therapy models. Thereafter, we outline the proposed composite tumor-treatment model. Section 3 presents a sensitivity analysis concerning tumor growth and stress distribution, exploring the influence of various HESW parameters. We also use real data from an *in vitro* experiment, utilizing the insights from the previous section to simulate HESW therapy with parameter sets designed to induce diverse effects on tumor growth and volumetric stresses. Then, we discuss the practical viability of these sets of parameters and outline the subsequent steps to develop a more accurate and broad model.

2. Materials and Methods

The simulation of HESW therapy applied to a tumor involves the interaction of two models. One model represents the interplay of stresses and the anisotropic growth of an avascular tumor, while the other involves solving a wave equation with a source

term to simulate the therapy.

Several tumor models have been proposed in the literature within the framework of continuum mechanics Stylianopoulos [2017]; Unnikrishnan et al. [2010]; Jones and Chapman [2012], ranging from linear elastic constitutive laws Araujo and McElwain [2004, 2005]; Jones et al. [2000]; Ngwa and Agyingi [2012]; Roose et al. [2003] to non-linear elastic models Pillay et al. [2018]; Voutouri et al. [2014]; Stylianopoulos et al. [2013], considering more complex interactions and are expressed in both the Eulerian and Lagrangian coordinate reference systems. These models take into account the stresses resulting from the mass addition caused by the tumor growth, and also how these stresses affect the tumor growth itself. The model adopted in this research belongs to the category using linear elastic constitutive equations, and its principal hypotheses are as follows. The tumor model deals with the stresses within the tumor and how they influence the rate and direction of tumor growth. Additionally, the rates of proliferation and death of the tumor cells depend on these stresses. The model equations assumes an ample nutrient supply at the tumor boundary, which is essential for tumor growth. It also imposes spherical symmetry on all quantities within the tumor, employing a spherical coordinate system in its mathematical formulation.

The mechanical therapy model is based on linear wave equations for elastic and isotropic materials. However, its complexity increases due to the necessity of calculating numerical solutions within a finite domain, leading to wave reflections at the boundary, potentially compromising the results of numerical experiments involving shock waves. To mitigate wave reflections at the boundary, we utilize absorbing boundary conditions (ABC), specifically the Perfectly Matching Layer formulation [Assi and Cobbold 2016]. This results in a model of wave propagation consisting of 15 equations formulated in Cartesian coordinates, in contrast with the classical 3-equation system for wave motion. These equations include three second-order equations for 3D displacement and twelve first-order equations for auxiliary variables associated with the ABC.

The contact between both models is at the tumor boundary, in the direction normal to the boundary. The tumor model needs the value of the radial stresses at its boundary at each instant of time, and the wave propagation model needs the value of the displacement at the boundary of the tumor. This relationship is described in the diagram of Figure 1.

The point of contact between these two models occurs at the tumor boundary, in the direction perpendicular to the boundary. The tumor model requires the values of radial stresses at its boundary at each time step, while the wave propagation model necessitates the displacement values at the tumor's boundary. This interaction is illustrated in Figure 1.

Given that both models employ different coordinate systems, it is necessary to convert coordinates for the radial stress, denoted as σ_r, and the displacement vector (u_x, u_y, u_z). For example, σ_r is computed using the stresses T_{ij} of the external medium, which are expressed in Cartesian coordinates. Meanwhile, the vector (u_x, u_y, u_z) is derived from the tumor displacement u_r, which is specified in spherical coordinates.

Let σ_r represent the stress in the radial direction at the tumor boundary, and

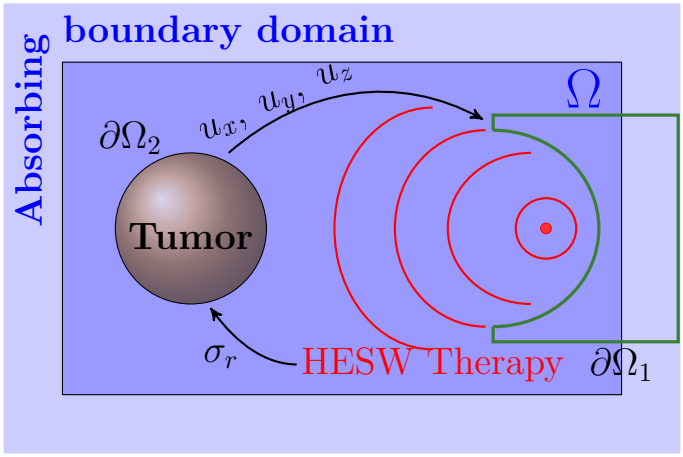

Figure 1. Plane projection diagram of the 3D mathematical model: The HESW therapy model determines the radial stress (σ_r) at the tumor boundary and, while simultaneously, the tumor model regulates the conditions for wave displacement (u_x, u_y, u_z) at its boundary. This coupling forms a well-defined model for mechanical therapy. The green contour in the diagram represents the device [Ogden et al. 2001] employed to generate HESW, which has different elasticity parameters compared to the external medium.

(u_x, u_y, u_z) denote the displacement components in Cartesian coordinates. We can establish the following relationships between these two coordinate systems:

$$\begin{aligned} \sigma_r &= T_{xx}\sin^2\theta\cos^2\phi + 2T_{xy}\sin^2\theta\sin\phi\cos\phi + 2T_{xz}\sin\theta\cos\theta\cos\phi + T_{yy}\sin^2\theta\sin^2\phi \\ &+ 2T_{yz}\sin\theta\cos\theta\sin\phi + T_{zz}\cos^2\theta, \qquad (1) \\ u_x &= u_r\sin\theta\cos\phi, \quad u_y = u_r\sin\theta\sin\phi, \quad u_z = u_r\cos\theta, \qquad (2) \end{aligned}$$

where θ, ϕ are the angle variables of the spherical coordinate system that can be mapped to the cartesian coordinate system as

$$x = r\sin\theta\cos\phi, \quad y = r\sin\theta\sin\phi, \quad z = r\cos\theta,$$

where r denotes the radial coordinate variable within the spherical coordinate system, with its origin at the center of the tumor. The stress in the radial direction, σ_r, is expressed in terms of the tensor stress components $(T_{xx}, T_{xy}, T_{xz}, T_{yy}, T_{yz}, T_{zz})$ in Cartesian coordinates (Eq. (1)), which are used in the mechanical therapy model. On another hand, the displacement vector (u_x, u_y, u_z) is formulated from within the spherical coordinate system (Eq. 2), as applied in the tumor model.

2.1. Tumor model

The tumor model we use in this study builds upon the mathematical framework introduced in Valdes-Ravelo et al. [2018], which focuses on the growth of avascular tumors. This model is grounded in continuum mechanics, crucial to understand the tumor mechanical responses to HESW therapy. Moreover, it has a balance between a simplified structure that permits in-depth analysis of the stress changes by the HESW therapy with minimal interference from other factors, yet remains representative of a realistic setting.

In this model, the tumor is treated as a homogeneous elastic material with a

well-defined solid shape. The geometry of the tumor will be assumed as spherical, maintaining its symmetry at all times. The tumor growth is stress-dependent, and its direction of growth depends anisotropically on the stresses. The external medium is considered elastic, isotropic, homogeneous, and infinite. Notably, our model differs from Valdes-Ravelo et al. [2018] in a fundamental way. Here, we explicitly model the external medium to assess the impact of HESW therapy on the tumor, while in the previous study, the influence of the external medium was implicitly embedded in the equations.

The proliferation and death of the tumor cells in the model are considered to be dependent on the stresses. This relation determines the anisotropy in the directions of growth, favoring those with less compressive stress. Moreover, this condition can even lead to inhibition of cellular growth in the presence of stresses, and, on a lower level, enhancement of cellular death.

The tumor model has two independent variables, denoted as t and r, where t represents time, and r indicates the distance of a particle point to the center of the tumor. These two variables suffice to describe the spatial position of any point within the tumor at any time, due to our assumption of spherical symmetry. Furthermore, there are five dependent variables, corresponding to a critical aspect of the mathematical model. Each of these variables is governed by its own equation, collectively forming a quasilinear system of first-order partial differential equations. The equations governing tumor growth and stress distribution in the system are structured as outlined in Valdes-Ravelo et al. [2018]:

$$\frac{dR}{dt}(t) = v_r(R,t), \tag{3}$$

$$\begin{aligned}\frac{\partial v_r}{\partial r}(r,t) &= \frac{R\sinh(r)}{r\sinh(R)}[1-\zeta_1\sqrt{\sigma_r^2(r,t)+2(\sigma_r(r,t)-\beta(r,t))^2}] \\ &- \epsilon[1+\zeta_2\sqrt{\sigma_r^2(r,t)+2(\sigma_r(r,t)-\beta(r,t))^2}] - 2\frac{v_r(r,t)}{r},\end{aligned} \tag{4}$$

$$\frac{\partial \sigma_r}{\partial r}(r,t) = -\frac{2\beta}{r}, \tag{5}$$

$$\begin{aligned}\frac{\partial g}{\partial t}(r,t) &= -v_r(r,t)\frac{\partial g}{\partial r}(r,t) + \frac{R\sinh(r)}{r\sinh(R)}\left(1-\zeta_1\sqrt{\sigma_r^2(r,t)+2(\sigma_r(r,t)-\beta(r,t))^2}\right) \\ &- \epsilon\left(1+\zeta_2\sqrt{\sigma_r^2(r,t)+2(\sigma_r(r,t)-\beta(r,t))^2}\right),\end{aligned} \tag{6}$$

$$\frac{\partial \beta}{\partial t}(r,t) = -v_r(r,t)\frac{\partial \beta}{\partial r}(r,t) + \varpi(r,t), \tag{7}$$

with

$$\begin{aligned}\varpi(r,t) &= \frac{1}{1+2ag\dfrac{e^{a\beta}}{(e^{a\beta}+2)^2}}\left[\frac{e^{a\beta}}{e^{a\beta}+2}\left(\frac{R\sinh(r)}{r\sinh(R)}\left[1-\zeta_1\sqrt{\sigma_r^2(r,t)+2(\sigma_r(r,t)-\beta(r,t))^2}\right]\right.\right. \\ &- \left.\left.\epsilon\left[1+\zeta_2\sqrt{\sigma_r^2(r,t)+2(\sigma_r(r,t)-\beta(r,t))^2}\right]\right) + \frac{\partial v_r}{\partial r}\right].\end{aligned}$$

subject to the initial and boundary conditions

$$R(0) = R_0, \tag{8}$$
$$v_r(0,t) = 0, \tag{9}$$
$$\sigma_r^-(R(t),t) = \sigma_r^+(R(t),t), \tag{10}$$
$$g(r,0) = 1, \tag{11}$$
$$\beta(r,0) = 0. \tag{12}$$

Equation (3) models the tumor radius, $R(t)$, at time t. Equation (4) represents the velocity of a particle within the tumor, $v_r(t,r)$. The third equation, (5), determines the radial stress, $\sigma_r(r,t)$. The mass growth, $g(r,t)$ (also referred to as volumetric growth), is modeled by equation (6). Equation (7) accounts for $\beta(r,t)$, the difference between transversal and radial stress. A description of the other terms used can be found in Table 1.

Term	Definition
R_0	Initial radius of the tumor
ζ_1	Represents the dependence of cell proliferation rate with respect to stresses
ζ_2	Represents the dependence of cell death rate with respect to stresses
ϵ	Ratio of the proliferation and death of cellular rates
a	Positive constant that regulates the anisotropy of the growth with respect to stresses
σ_r^+	Radial stress at tumor boundary calculated from the external medium
σ_r^-	Radial stress at tumor boundary calculated from the interior of the tumor

Table 1. Description of terms used in the tumor model.

For the boundary condition of σ_r in the tumor model equation, given by Eq. (10), σ_r^+ is provided by the external wave propagation model. However, since the tumor model has spherical symmetry, the boundary condition can only be set if the limit (calculated from outside the tumor) of radial stress at the tumor boundary remains constant across all points. This assumption is somewhat unrealistic. Therefore, the value used for σ_r^+ is determined as the average radial stress observed at the tumor boundary. Using the mean value of σ_r^+ at the boundary ensures not only the preservation of the tumor's spherical symmetry but also contributes as a measure of the stress profile at the tumor boundary.

2.2. HESW therapy model

The HESW therapy involves a device designed to generate shock waves, employing a reflector positioned within the external medium to concentrate the energy of the shock wave into a small, targeted treatment area [Ogden et al. 2001]. This reflector possesses an elliptical shape, with the source of the shock wave situated at one of its focal points, while the region of energy concentration is positioned at the second focus of the ellipse (for further details, see Ogden et al. [2001]). Within the model, the device is incorporated by specifying different values of the material parameters in the region occupied by the reflector.

The mechanical therapy aspect is represented by a time-dependent source term that generates elastic waves within the external medium. While considering the interaction

between the propagating waves and the tumor model, taking place at the boundary of the tumor. The external medium is characterized by its elastic, isotropic, and homogeneous (without considering the reflector) properties. The linear elastodynamic wave equations for such media with an additional source term can be expressed as follows:

$$\rho(\boldsymbol{x})\frac{\partial^2 u_i}{\partial t^2}(\boldsymbol{x},t) = \sum_{j=1}^{3}\sum_{k,l=1}^{3} C_{ijkl}(\boldsymbol{x})\frac{\partial^2 u_k}{\partial x_j \partial x_l} + F s_i(\boldsymbol{x},t), \quad i = 1,2,3, \tag{13}$$

where ρ is the density, C_{ijkl} are the material stiffness coefficients of the elastic medium, and u_i is the i-th component of the displacement vector.

The parameter F determines the wave amplitude, and the source term s_i is assumed to be direction-independent, meaning that $s_1 = s_2 = s_3$. These source terms only have non-zero values for small durations in time, and in a small region around the source position. In the simulations conducted in this work, we considered this region to be a sphere with a non-dimensional radius of $l = 0.2$. The signal shape of the source term is obtained from Ogden et al. [2001] and is illustrated in Figure 2.

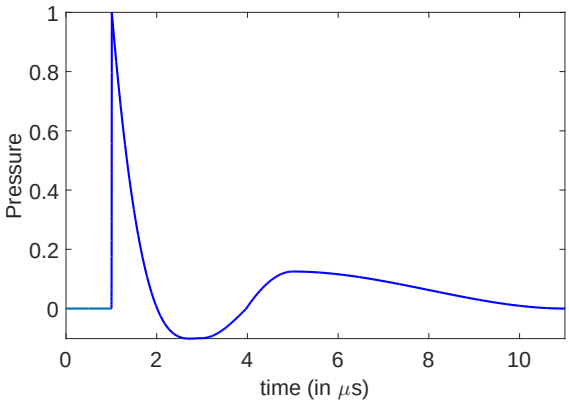

Figure 2. The pattern of the pressure variation of a typical shock wave used in HESW therapy. The shock wave is composed of a very fast increment in pressure followed by negative pressure and a damping lasting 7 μs.

The system of equations (13) is well-defined for an infinite medium, with a condition at the tumor boundary obtained from the tumor model. However, numerical solutions requires a finite domain Ω instead of an infinite one, which introduces challenges at the external boundaries, where unwanted reflections may appear.

To mitigate the reflections at the outer boundary of the external medium, we employ an absorbing boundary condition. Various absorbing conditions are documented in the literature [Randall 1988; Assi and Cobbold 2016; Nataf 2013]. While none of them is perfect, some exhibit better absorption characteristics than others. We have chosen the Perfectly Matching Layer (PML), known for its ability to exponentially attenuate plane waves, irrespective of their frequency and incident angle. A popular choice in recent publications on wave propagation in finite domains [Tago et al. 2012; Jing et al. 2019; Chern 2019]. Nonetheless, it comes at the cost of being one of the most compu-

tationally expensive absorbing boundary conditions, as it introduces twelve equations for auxiliary variables to the system (13). Furthermore, it requires an extension of the domain boundaries, to form a layer for wave attenuation (see Fig. 1). Following Assi and Cobbold [2016], it can be expressed through the following system of equations:

$$\rho\left(\frac{\partial^2 u_i}{\partial t^2}+a_1(\boldsymbol{x})\frac{\partial u_i}{\partial t}+a_2(\boldsymbol{x})u_i+a_3(\boldsymbol{x})U_i\right)=\sum_{j=1}^{3}\left(\sum_{k,l=1}^{3}C_{ijkl}\frac{\partial^2 u_k}{\partial x_j\partial x_l}+\frac{\partial w_{ij}}{\partial x_j}\right)+Fs_i(x,t), \tag{14}$$

$$\frac{\partial w_{ij}}{\partial t}+\gamma_j w_{ij}=\sum_{k,l=1}^{3}\left(\tilde{C}_{ijkl}\frac{\partial u_k}{\partial x_l}+\breve{C}_{ijkl}\frac{\partial U_k}{\partial x_l}\right),\quad \boldsymbol{x}=(x_1,x_2,x_3)\in\overline{\Omega}, \tag{15}$$

$$\frac{\partial U_i}{\partial t}=u_i, \tag{16}$$

where u_i is the displacement on the direction x_i and the variables w_{ij}, U_i are auxiliary variables of the PML condition, $a_1(\boldsymbol{x})=\gamma_1+\gamma_2+\gamma_3$, $a_2(\boldsymbol{x})=\gamma_1\gamma_2+\gamma_1\gamma_3+\gamma_2\gamma_3$, $a_3(\boldsymbol{x})=\gamma_1\gamma_2\gamma_3$, $\tilde{C}_{ijkl}=(a_1-\gamma_j-\gamma_l)C_{ijkl}$, $\breve{C}_{ijkl}=\frac{a_3}{\gamma_l}C_{ijkl}$, are the material coefficients of the elastic medium, Ω is the real computational domain, $\overline{\Omega}$ is the extended computational domain with the PML layer, and the γ_i are functions defined as

$$\gamma_i(x_i)=\begin{cases}0, & if x_j\in\Omega,\\ \gamma_0\left(\frac{d(x_j,\Omega)}{\delta}\right)^2, & if x_j\notin\Omega,\end{cases} \tag{17}$$

where $d(x_i,\Omega)$ is the distance from x_i to the set Ω, γ_0 is a fixed constant, and δ is the width of the PML layer. The functions γ_i determine how fast the waves amplitude are attenuated in the PML domain. Summarizing, the variables of the equations (14)-(16) are u_i, w_{ij}, U_i, and the parameters are the density ρ and the material parameters C_{ijkl}. Since we are using linear elasticity in an isotropic medium the coefficients C_{ijkl} are expressed as a linear combination of the Lamé parameters, λ and μ, of the external medium

$$C_{ijkl}=\lambda\delta_{ij}\delta_{kl}+\mu(\delta_{ik}\delta_{jl}+\delta_{il}\delta_{jk}), \tag{18}$$

where δ_{ij} is Dirac's delta.

Equations (14) and (15) are of hyperbolic nature. Therefore, for the displacement u_i, with $1\leq i\leq 3$, beside boundary conditions at $\partial\Omega$ (Ω is the region on Fig. 1 excluding the tumor), initial conditions must be given.

Let $\partial\Omega_1$ denote the boundary of $\overline{\Omega}$, which coincides with the limits of the rectangle in Fig. 1, and $\partial\Omega_2$ corresponding to the boundary that aligns with the spherical shape of the tumor in the same figure. As $\partial\Omega_1$ lies within the absorbing boundary of the PML domain, conditions can be arbitrarily set. For simplicity, we apply zero Dirichlet boundary conditions for u_i,

$$u_i|_{\partial\Omega_1}=0. \tag{19}$$

Regarding $\partial\Omega_2$, the condition pertains to the displacement of the external medium

from the growth of the tumor,

$$u_i|_{\partial\Omega_2} = u_r|_{\partial\Omega_2}. \tag{20}$$

However, due to the potential misalignment of the squared mesh grid with the actual tumor boundary, a first-order interpolation is employed.

The initial conditions for the wave equation concerning u_i are as follows,

$$u_i(\boldsymbol{x}, 0) = \begin{cases} (\|\boldsymbol{x}\| - R_0 - 1)^2 u_{i0}(\boldsymbol{x}), & if\ \|\boldsymbol{x}\| < R_0 + 1, \\ 0, & if\ \|\boldsymbol{x}\| \geq R_0 + 1, \end{cases} \qquad i = 1, 2, 3, \tag{21}$$

where R_0 is initial the tumor radius and $u_{i0}(\boldsymbol{x})$ is the evaluation of u_i at the nearest point in the tumor boundary of the coordinate $\boldsymbol{x}$. Condition (21) is only used to ensure a smooth initial condition, but it does not have any physical meaning. Additionally, the initial velocity is considered as zero.

The variables w_{ij} and U_i of equations (15) and (16) serve exclusively to attenuate waves at the boundary of the numerical domain. As such, their initial values can be set to zero, as expressed in the equation below.

$$w_{ij}(\boldsymbol{x}, 0) \equiv 0, \quad U_i \equiv 0, \quad i, j = 1, 2, 3. \tag{22}$$

The HESW therapy model, as defined by equations (14)-(16) with the proposed initial and boundary conditions, is well-posed. All the variables have their initial conditions, and the hyperbolic equations (14) also have their boundary conditions.

2.3. Solution of the joint model

In this section we discuss the algorithms employed to compute the numerical solution of the coupled model. The growth of the avascular tumor is governed by equations (3)-(7), together with initial and boundary conditions (8)-(12). The HESW application, on the other hand, is described by equations (14)-(16), with boundary and initial conditions (19)-(22).

To calculate the boundary condition (10) for σ_r^+ from the wave equations model, it becomes essential to identify the square mesh points delimiting the spherical contour of the tumor. Then, for each of these points, an interpolated value of the radial stress at the tumor boundary is determined, and the mean of these values is used to define σ_r^+.

Regarding the wave equations, we use second-order centered finite differences in space and a fourth-order Runge-Kutta method in time. The finite difference scheme is expressed in Cartesian coordinates with a square mesh grid. However, due to the tumor spherical shape, the precise representation of the tumor boundary is not attainable on the square mesh grid of the HESW model. Consequently, this leads to first-order approximations of the boundary condition in $\partial\Omega_2$, connecting both models.

At each time instant, we compute the solution of the tumor model and the wave equations with PML conditions, sequentially. The tumor model employs a method outlined in Valdes-Ravelo et al. [2018], which also relies on finite differences. It adopts

a Lax-Wendroff scheme with moving points for equations (6) and (7), based on the approximation

$$\begin{aligned}
\beta\left(r_i^{(j+1)}, t_{j+1}\right) &= \beta\left(r_i^{(j)} + (R(t_{j+1}) - R(t_j))i/i_{máx}, t_j + k\right) \\
&\approx \beta\left(r_i^{(j)}, t_j\right) + \frac{\partial\beta}{\partial r}(R(t_{j+1}) - R(t_j))\frac{i}{i_{máx}} + \frac{\partial\beta}{\partial t}\left(r_i^{(j)}, t_j\right)k \\
&+ \frac{\partial^2\beta}{\partial r^2}(R(t_{j+1}) - R(t_j))^2\frac{i^2}{2i_{máx}^2} + \frac{\partial^2\beta}{\partial r\partial t}(R(t_{j+1}) - R(t_j))\frac{i}{i_{máx}}k \\
&+ \frac{\partial^2\beta}{\partial t^2}\left(r_i^{(j)}, t_j\right)\frac{k^2}{2},
\end{aligned}$$

where the time derivatives are replaced by spatial derivatives using the original model equations, and $r_i^{(j+1)}$ is the position of the mesh point $r_i^{(j)}$ after the time step k. For equations (3), (4), and (5), an explicit Euler method is used, incorporating boundary values for σ_r^+ derived from the HESW model. Consequently, when computing the solution of the tumor model at the time instant t_{n+1}, the value of σ_r^+ from the previous time instant t_n is utilized.

The assumption that waves propagate within a homogeneous medium is very restrictive. This is particularly evident when considering internal tumors, where waves must traverse different materials. While shock waves can travel through water and soft tissues with minimal energy loss, at the interfaces between dissimilar materials could induce tissue damage through phenomena as cavitation and shearing stresses caused by wave reflections [Serpe et al. 2011]. Nevertheless, there exist certain specific scenarios in which our assumption accurately mirrors real-world experimental settings, such as those described in Gamarra et al. [1993a,b]. In these experiments, it was applied the HESW therapy to treat cutaneous tumors induced by a melanoma cancer cell line. Hence, there were no interfaces of soft tissue between the wave and the tumor. Additionally, the propagation medium was composed entirely of water, making it completely homogeneous.

2.4. Parameters of mechanical models

One of the main difficulties in validating and using mathematical models is a reliable estimation of the model parameters and the availability of experimental data to compare the model results. Usually, the most complicated issue is the first part, where sometimes it does not exist the technique to accurately measure the parameters of the model, or the parameters' measurement is so complicated and expensive to be done, or it is simply impossible. In addition, the parameters of models related to biological processes are very dependent on the test case, depending on the type of tissue, the type of damage, and the exact location in the body. This is particularly true for mechanical models, where accurate measures of the stresses should be done in the tumor at different instant times to accurately test the stress-deformation law, but we can only do one measure of the stresses, and it is when the tumor is cut. Moreover, it is known that the elasticity parameters depend on the type of tumor cell, but to date, less than twenty measures of different types of tumor have been reported in the literature. In addition, there are other sets of parameters that it is impossible to measure and reasonable guesses have to be taken into consideration.

To assist in this task, we present a concise summary of published data pertaining to the parameters essential for the continuum mechanics-based tumor model proposed in this article. This dataset encompasses measurements of physical and elastic constants for various cell types, with some conversions applied to ensure consistent physical units. Additionally, we provide references to tumor growth experiments, covering both *in vivo* and *in vitro* scenarios, involving treatments such as HESW therapy and chemotherapy, and include details on the underlying experimental setups. This information is systematically organized in Tables C1, C2, and C3 within Appendix C. The data in Table C1 comprises biological measures of parameters used in a mathematical tumor model, regardless of its basis in continuum mechanics. Many of these measurements were reported by Bryan et al. [2014]; McMurtrey [2016]; Palm et al. [2018]. Table C2 provides information on the elastic parameters of thirteen different types of tumors. Most of this data was extracted from the works of Stylianopoulos et al. [2012]; Voutouri et al. [2014], where a mechanical tumor model was also proposed. In Table C3 are referenced fifteen publications where real experiments on growing tumors were conducted, and tumor volume measurements were recorded. In thirteen out of these fifteen experiments, High-Energy Shock Wave (HESW) therapy was employed, with seven of these experiments involving combination therapies.

From this data, we extracted the parameter values for use in the following section.

3. Results

The primary objective of our numerical investigation is to assess the changes of volumetric stresses inside a tumor produced by the HESW therapy. Moreover, we are also interested to know whether the proposed model can qualitatively replicate the observed delay in tumor growth resulting from HESW therapy, as documented in the experiments described by Russo et al. [1986]; Wörle et al. [1994]; Hoshi et al. [1991]. Additionally, we conduct numerous simulations to identify the parameters within the HESW therapy that exhibit the most significant influence within our analytical framework.

In the simulations, we adopted non-dimensional variables for all physical quantities (please refer to Appendix A for details). Unless otherwise specified, we maintain fixed parameter values for all simulations, which are presented in Table 2 for reference. To ensure the reproducibility of our numerical experiments, we provide information on the spatial arrangement of objects in Fig. 1 in Appendix B.

The parameters ζ_1 and ζ_2 dictate how tumor proliferation is influenced by the stresses. The relation between these values is chosen based on *in vitro* experiments, which have shown that pressure induces apoptosis in tumor spheroids approximately 100 times less effectively than it inhibits proliferation [Montel et al. 2012]. The parameters a and ϵ depend on the tumor type. In this model, we assume slight anisotropy in tumor growth, with $a = 0.01$, and that tumor cells multiply four times faster than they die in the absence of stress, represented by $\epsilon = 0.25$.

The parameters ρ, μ_E, and λ_E in Table 2 are selected somewhat arbitrarily but maintain relative magnitudes consistent with physical properties of external media like gels (see Appendix C). Nonetheless, the most important aspect is that wave propagation velocities in the gel are much faster than in the shock wave device material,

Parameter	Value	Definition
R_0	1	Initial radius of the tumor
ζ_1	0.025	Represents the dependence of tumor cell proliferation rate from stresses
ζ_2	0.00025	Represents the dependence of tumor cell death rate from stresses
ϵ	0.25	Ratio of the proliferation and death of cellular rates
a	0.001	Positive constant that regulates the anisotropy of the tumor growth in relation with stresses
ρ	1.1	Density of the external medium
μ_E	0.9	Shear modulus of the external medium
λ_E	0.4	First Lamé parameter of external medium
γ_0	30	Attenuation of waves at the PML layer
δ	0.5	Thick of the PML layer
μ_D	0	Shear modulus of the device to generate shock waves
λ_D	0	First Lamé parameter of the device to generate shock waves
F	$1.5 \cdot 10^{11}$	Represents the peak amplitude of the generated waves

Table 2. Parameters used in the simulations. The relation of parameters of the tumor model is chosen accordingly to the work of Valdes-Ravelo et al. [2018], while the other values are set arbitrarily since we are interested only in the qualitative behavior.

μ_D and λ_D, which are both assumed to be zero to simulate a material reflecting all wave energy. The parameters γ_0 and δ do not possess physical interpretations, and their values are set to avoid spurious reflections at the boundary of the entire model domain, $\overline{\Omega}$.

3.1. Effect of HESW therapy on tumor growth

As an initial simulation, we compare a reference tumor growth model (without shock waves) and one with the application of 200 shock waves at a frequency of 50Hz. The results are presented in Figure 3.

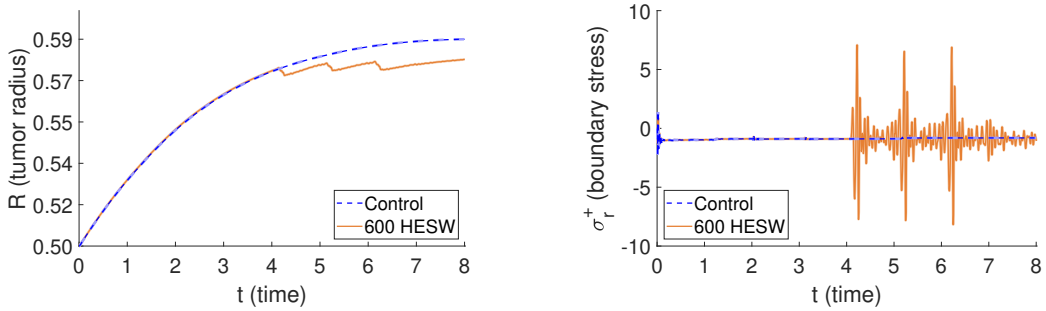

Figure 3. Comparison in time of tumor growths without HESW therapy (blue) and with the therapy (red). The left panel displays the tumor radius, while the right panel illustrates the radial stresses at the tumor boundary for both cases.

In both simulations, it is apparent an adjustment of the initial stresses. This is a result of an unbalanced initial condition, where we assume that the stresses are initially zero. As we can see for both simulations there is an initial adjustment of the stresses,

since we are assuming that the stresses are zero as initial conditions. The results between the reference and treated tumor growth are identical until time $t = 4$, just before the shock waves are triggered. As observed in the left panel of Figure 3, following the application of HESW therapy, there is a noticeable reduction in tumor growth, corresponding with findings in experiments [Russo et al. 1986; Wörle et al. 1994; Hoshi et al. 1991]. On the other hand, examining the right panel, which showcases radial stresses at the tumor boundary, reveals significant oscillations in the stresses of the HESW simulation. This phenomenon can be elucidated as follows: As the tumor size decreases, material response causes the radial stresses to become tensile, leading to increased velocity. In turn, this produces a compression of stresses due to external medium pressure. Consequently, the growth velocity decreases once more, leading to a repetitive cycle (as present in the left graph, which displays slight growth oscillations).

For this simulation, HESW therapy can be perceived as a perturbation of the equilibrium between tumor growth and stress. This perturbation is characterized by reduced tumor growth, with oscillations in growth velocity, and pronounced fluctuations in radial stresses at the tumor boundary. These insights were primarily focused on observations at the tumor boundary. Nonetheless, we can also study the internal tumor mechanisms, serving as validation and providing useful insights.

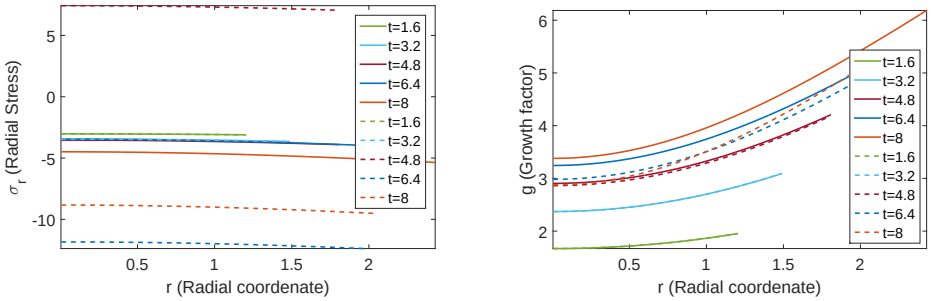

Figure 4. Comparison of stresses and the tumor growth factor (Eq. (6)), without HESW therapy (solid lines) and with the therapy (dashed lines), at five instants of time. On the left side, the radial stresses inside the tumor of both simulations are displayed, while on the right side, it is presented the volumetric growth factor of the tumor.

The radial stresses at five different time instants inside the tumor are presented in the left panel of Figure 4. The curves corresponding to the simulation with HESW (dashed lines) have a qualitatively different behavior when compared with the stresses without the therapy (solid lines). These differences are probably induced by the oscillations at the tumor boundary, as discussed earlier, and they have a significant impact on the growth factor (right panel). As depicted in the right panel, this has a direct effect on volumetric growth. At time instants $t = 4.8, ; 6.4, ; 8$, which corresponds to the period following therapy application, the tumor growth factor is significantly reduced with HESW therapy compared to the untreated scenario. This supports the previous observation that HESW therapy induces stress oscillations, which subsequently impact tumor growth.

Having comprehended the basic mechanism of how HESW influences tumor growth in our model, we can now explore the effects of the HESW therapy on tumor evolution. This will be done by varying some of its parameters, such as the number

of waves and their amplitudes.

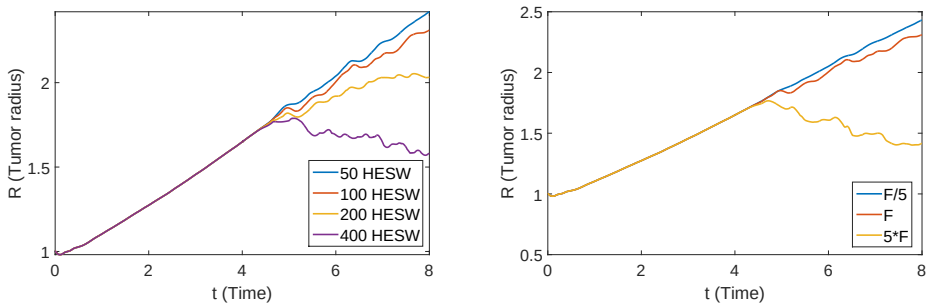

Figure 5. Comparison of tumor growth over time with HESW therapy for different numbers of shock waves (left side) and several peak amplitude (right side: using $F = 1.5 \cdot 10^{11}$, and 100 shock waves).

Increasing the number of shock waves initially decreases tumor growth, eventually leading to even a tumor size reduction (Figure 5, left panel). Similarly, elevating the wave peak amplitudes reduces tumor growth (Figure 5, right panel). These clear trends indicate that both the number of waves and their amplitudes play a crucial role in the HESW therapy effectiveness.

On another hand, the distance of the device from the tumor is also an important element to consider in HESW therapy. Consequently, we conducted simulations with varied distance units between the device and the tumor, acknowledging that these non-dimensional distances have a unit of measure comparable to a centimeter.

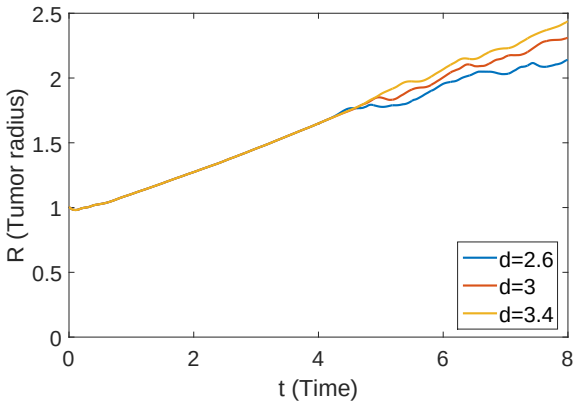

Figure 6. Comparison of tumor growth over time by varying the distance between the HESW source and the tumor center in: 2.6 units (blue curve), 3 units (red curve), and 3.4 units (orange curve).

Figure 6 illustrates that when the distance between the HESW source and the tumor is smaller, the effect of the therapy is greater. Suggesting that even for more complex geometries, considering the relative source-tumor position is a valuable factor when determining the position of the clinical device to produce the HESW. Although this is a very intuitive result, since the closer the source is, the more concentrated the energy in the tumor will be. It is very important to notice that our model is able to represent this.

Another parameter of the HESW therapy we can analyze is the frequency of the shock waves. However, in the numerical experiments spanning frequencies from 1Hz to 300Hz, we observed almost no discernible influence on tumor growth (results not shown). This could be because our model fails to consider some important mechanics depending on the HESW frequency that could influence the tumor growth, or that frequency is not a relevant parameter in this context.

It is important to note that these results are highly dependent on the mechanical properties of the external medium and the tumor itself. If, for instance, the material properties of the external medium or the tumor were to change, it could lead to different responses to HESW therapy.

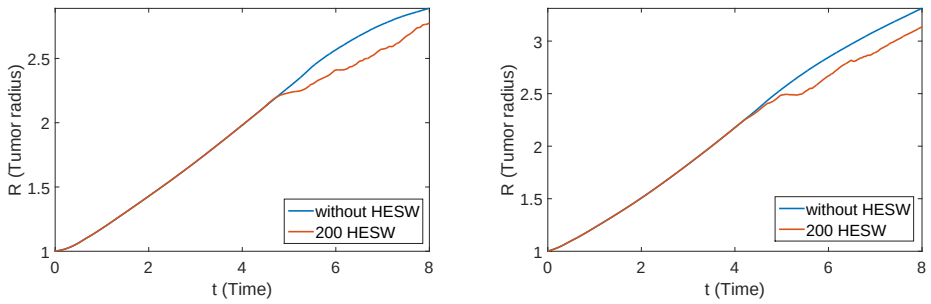

Figure 7. Comparison of tumor growth over time without HESW therapy (blue curve) and with the therapy (red curve). On the left, the simulation is the same as in Figure 3, with alterations made to the properties of the external medium ($\mu_E = 0.1$ and $\lambda_E = 0.45$). On the right, the change is in the stress-deformation relationship of the tumor, with values adjusted as follows: $\epsilon = 0.35$, $\zeta_1 = 0.035$, and $\zeta_2 = 0.00035$.

The influence of material parameters on tumor growth after therapy, as shown in Figures 7, agrees with the findings of Smits et al. [1991]. Their research suggests that the impact of HESW therapy is closely tied to the material properties of both the tumor and the external medium.

3.2. Comparison of the model with real data experiment

In the previous section, we studied the impact of HESW on tumor growth and the importance of the therapy parameters. It was demonstrated that the model can qualitatively replicate real-life experiment outcomes. However, these simulations employed hypothetical parameter values that do not correspond to real-world data. Consequently, our aim in this section is to replicate tumor growth as reported in one of the experiment references documented in Table C3, which also provides measurements for the tumor elasticity constants. Subsequently, we will simulate HESW therapy in this context, assessing its effects under typical therapy conditions.

Unfortunately, the tumor types for which we possess elastic parameter data do not coincide with those in the referenced HESW experiments. Nevertheless, we can still simulate the therapy in a realistic case scenario; however, we will not have the opportunity to compare our results with real data. Consequently, for the simulations we will use data from an experiment detailed in Roose et al. [2003], where is measured tumor growth in mice from the mesenchymal melanoma cell line MU89. The elasticity

constants for this tumor type can be found in Table C2, and other model parameters are drawn from Table C1.

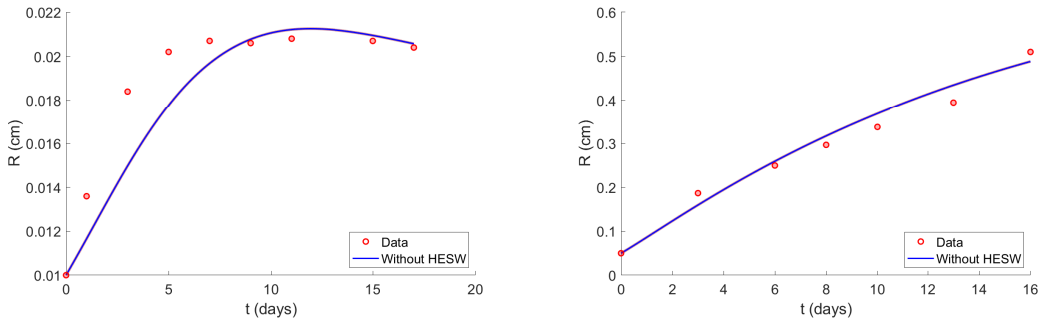

(a) Tumor cell line MU89.

(b) Tumor cell line MU89.

Figure 8. Comparisson of the tumor model (blue curve) to experimental data of tumor evolution in pre-clinical experiments in mice (red dots). The model presents a good adjustment to the experimental data.

Figure 8 shows that the model can replicate with a good accuracy the experimental data.

4. Discussion

We developed a coupled mathematical model of a tumor growth based on continuum mechanics, with a mathematical formulation to replicate a HESW therapy. The model is intended to be a prototype that allows a proof of concept towards reproducibility of HESW treatment. It proposes a different direction for mechanical models of tumor growth, different from the current existing models, which have not previously integrated HESW therapy. Moreover, our method is very straightforward to replicate. Not only can the linear equations (14)-(16) describing HESW be integrated into any continuum mechanics-based tumor model, but the same can be done for the non-linear wave propagation equations.

We studied various possible outcomes of tumor growth by using variations of the HESW therapy parameters. For the therapy parameters, we found that the shock wave number and the wave peak energy have a higher influence than the wave frequency on the tumor growth. The distance of the source to the tumor was also very relevant to the effectiveness of the treatment. Notably, the obtained numerical solutions are qualitatively similar to the experiments carried out in the works of Russo et al. [1986]; Wörle et al. [1994]; Hoshi et al. [1991], supporting the validity of these preliminary results. We also compared the model using data from a real experiment of tumor growth *in vitro*, and observed that if we restrict to peak frequencies used in practical applications, the HESW therapy does not produce any perceptible change in the tumor evolution. This results suggests that the stress changes within the tumor, produced by the pressure variation of the HESW, is not a determining element in the growth of a tumor.

We examined various potential tumor growth outcomes in the model through the manipulation of HESW therapy parameters. In our analysis, we discovered that the

shock wave number and the peak energy of the waves wielded a more significant influence on tumor growth compared to wave frequency. Moreover, the distance between the wave source and the tumor had a substantial impact on the efficacy of the treatment. It is worth noting that the numerical solutions we obtained exhibited qualitative similarities to experiments conducted in previous works, such as those by Russo et al. [1986]; Wörle et al. [1994]; Hoshi et al. [1991]. Supporting the validity of these preliminary results.

Furthermore, we conducted a comparison of our model using data from an *in vitro* tumor growth experiment. And it was revealed that, when we limit the analysis to peak frequencies relevant to practical applications, the HESW therapy did not induce any perceptible alterations in tumor progression. This outcome suggests that stress changes within the tumor, resulting from pressure fluctuations associated with HESW, may not be a decisive factor in tumor growth.

A fundamental limitation of our model is that it considers only the volumetric stresses, which constitute just one element of the mechanisms involved in HESW therapy. Nevertheless, the model provided valuable insights into how HESW influences stress dynamics within the tumor. This model can be expanded to encompass other important elements, making it a valuable tool in the understanding and application of HESW therapy. Furthermore, our model serves as a base for investigations where HESW therapy can be simulated in conjunction with other treatment modalities like chemotherapy, radiotherapy, or immunotherapy. This approach could provide new strategies for the creation of optimal treatment schemes.

Extensions of the model to consider chemotherapy and immunotherapy can be carried out with the introduction of a vascular network within the tumor. This network would facilitates the passage of the drugs to the interior of the tumor. A starting point for this extension is the work of Araujo and McElwain [2006], where a vascular tumor is considered while conserving spherical symmetry.In such a framework, stresses hold immense significance, given the inherent instability of tumor vessels, largely influenced by the volumetric stresses acting on the tumor [Stylianopoulos et al. 2013]. Furthermore, the incorporation of the non-linear wave propagation equations [Fagnan et al. 2014] can simulate effects such as cavitation and cell permeability accurately [Tanguay 2004]. Additionally, the inclusion of radiotherapy can be performed by the addition of the therapy term proposed by Liu et al. [2014] in the model equations. These paths represent compelling directions for the future development of our present study.

Disclosure statement

The authors declares that they have no relevant or material financial interests that relate to the research described in this paper.

Funding

This research was carried out in association with the ongoing R& D project registered as ANP 20714-2, “Software technologies for modelling and inversion, with applications in seismic imaging” (University of São Paulo / Shell Brasil / ANP) - Desenvolvi-

mento de técnicas numéricas e software para problemas de inversão com aplicações em processamento sísmico, sponsored by Shell Brasil under the ANP R& D levy as "Compromisso de Investimentos com Pesquisa e Desenvolvimento".

References

Abdelhalim NM, et al. (2018) Comparison of extracorporeal shock waves therapy versus intermittent pneumatic compression therapy in breast cancer-related lymphedema. International Journal of Cancer Research 14(2):77–85

Albro MB, Chahine NO, Li R, Yeager K, Hung CT, Ateshian GA (2008) Dynamic loading of deformable porous media can induce active solute transport. Journal of biomechanics 41(15):3152–3157

Altrock PM, Liu LL, Michor F (2015) The mathematics of cancer: integrating quantitative models. Nature Reviews Cancer 15(12):730–745

Ambrosi D, Mollica F (2004) The role of stress in the growth of a multicell spheroid. Journal of mathematical biology 48:477–499

Araujo R, McElwain D (2004) A linear-elastic model of anisotropic tumour growth. European Journal of Applied Mathematics 15(3):365–384

Araujo RP, McElwain DS (2005) The nature of the stresses induced during tissue growth. Applied mathematics letters 18(10):1081–1088

Araujo RP, McElwain DS (2006) The role of mechanical host–tumour interactions in the collapse of tumour blood vessels and tumour growth dynamics. Journal of theoretical biology 238(4):817–827

Assi H, Cobbold R (2016) A second-order, perfectly matched layer formulation to model 3d transient wave propagation in anisotropic elastic media. In: Proceedings of Meetings on Acoustics, AIP Publishing, vol 29

Bryan AK, Hecht VC, Shen W, Payer K, Grover WH, Manalis SR (2014) Measuring single cell mass, volume, and density with dual suspended microchannel resonators. Lab on a Chip 14(3):569–576

Canaparo R, Serpe L, Catalano MG, Bosco O, Zara GP, Berta L, Frairia R (2006) High energy shock waves (hesw) for sonodynamic therapy: effects on ht-29 human colon cancer cells. Anticancer research 26(5A):3337–3342

Canney MS, Khokhlova VA, Bessonova OV, Bailey MR, Crum LA (2010) Shock-induced heating and millisecond boiling in gels and tissue due to high intensity focused ultrasound. Ultrasound in medicine & biology 36(2):250–267

Chern A (2019) A reflectionless discrete perfectly matched layer. Journal of Computational Physics 381:91–109

Deisboeck TS, Zhang L, Yoon J, Costa J (2009) In silico cancer modeling: is it ready for prime time? Nature Clinical Practice Oncology 6(1):34–42

Delius M, Adams G (1999) Shock wave permeabilization with ribosome inactivating proteins: a new approach to tumor therapy. Cancer research 59(20):5227–5232

Fagnan K, LeVeque RJ, Matula TJ, MacConaghy B (2008) High-resolution finite volume methods for extracorporeal shock wave therapy. In: Hyperbolic Problems: Theory, Numerics, Applications, Springer, pp 503–510

Fagnan K, LeVeque R, Matula T (2014) Computational models of material interfaces for the study of extracorporeal shock wave therapy. Communications in Applied Mathematics and Computational Science 8(1):159–194

Frairia R, Catalano MG, Fortunati N, Fazzari A, Raineri M, Berta L (2003) High energy shock waves (hesw) enhance paclitaxel cytotoxicity in mcf-7 cells. Breast cancer research and treatment 81:11–19

Gamarra F, Spelsberg F, Dellian M, Goetz AE (1993a) Complete local tumor remission after therapy with extra-corporeally applied high-energy shock waves (hesw). International

journal of cancer 55(1):153–156
Gamarra F, Spelsberg F, Kuhnle GE, Goetz AE (1993b) High-energy shock waves induce blood flow reduction in tumors. Cancer research 53(7):1590–1595
Ghasemi M, Sivaloganathan S (2020) A computational study of combination hifu–chemotherapy as a potential means of overcoming cancer drug resistance. Mathematical Biosciences 329:108456
Grimes DR, Kelly C, Bloch K, Partridge M (2014) A method for estimating the oxygen consumption rate in multicellular tumour spheroids. Journal of The Royal Society Interface 11(92):20131124
Grote J, Süsskind R, Vaupel P (1977) Oxygen diffusivity in tumor tissue (ds-carcinosarcoma) under temperature conditions within the range of 20–40 c. Pflügers Archiv 372:37–42
Guba M, von Breitenbuch P, Steinbauer M, Koehl G, Flegel S, Hornung M, Bruns CJ, Zuelke C, Farkas S, Anthuber M, et al. (2002) Rapamycin inhibits primary and metastatic tumor growth by antiangiogenesis: involvement of vascular endothelial growth factor. Nature medicine 8(2):128–135
Hafner M, Niepel M, Chung M, Sorger PK (2016) Growth rate inhibition metrics correct for confounders in measuring sensitivity to cancer drugs. Nature methods 13(6):521–527
Helmlinger G, Netti PA, Lichtenbeld HC, Melder RJ, Jain RK (1997) Solid stress inhibits the growth of multicellular tumor spheroids. Nature biotechnology 15(8):778–783
Hoshi S, Orikasa S, Kuwahara MA, Suzuki K, Yoshikawa K, Saitoh S, Ohyama C, Satoh M, Kawamura S, Nose M (1991) High energy underwater shock wave treatment on implanted urinary bladder cancer in rabbits. The Journal of urology 146(2):439–443
Jing H, Chen Y, Wang J, Xue W (2019) A highly efficient time-space-domain optimized method with lax-wendroff type time discretization for the scalar wave equation. Journal of Computational Physics 393:1–28
Jones A, Byrne H, Gibson J, Dold J (2000) A mathematical model of the stress induced during avascular tumour growth. Journal of mathematical biology 40:473–499
Jones GW, Chapman SJ (2012) Modeling growth in biological materials. Siam review 54(1):52–118
Lee KE, Smith P, Cockett AT (1990) Influence of high-energy shock waves and cisplatin on antitumor effect in murine bladder cancer. Urology 36(5):440–444
Li D, Pellegrino A, Hallack A, Petrinic N, Jérusalem A, Cleveland RO (2018) Response of single cells to shock waves and numerically optimized waveforms for cancer therapy. Biophysical Journal 114(6):1433–1439
Liu Z, Yang C, et al. (2014) A mathematical model of cancer treatment by radiotherapy. Computational and mathematical methods in medicine 2014
López-Marín LM, Rivera AL, Fernández F, Loske AM (2018) Shock wave-induced permeabilization of mammalian cells. Physics of Life Reviews 26:1–38
Madersbacher S, Marberger M (2003) High-energy shockwaves and extracorporeal high-intensity focused ultrasound. Journal of endourology 17(8):667–672
Maruyama M, Asano T, Uematsu T, Nakagohri T, Hasegawa M, Miyauchi H, Iwashita C, Isono K (1995a) Enhancement of the antitumor effect by combined use of high-energy shock waves and atx-70. Japanese journal of cancer research 86(9):800–801
Maruyama M, Asano T, Uematsu T, Nakagohri T, Hasegawa M, Miyauchi H, Iwashita C, Tsuchiya Y, Isono K (1995b) The effect of high-energy shock wave therapy combined with cisplatin on mouse hepatoma. Surgery today 25:987–988
McMurtrey RJ (2016) Analytic models of oxygen and nutrient diffusion, metabolism dynamics, and architecture optimization in three-dimensional tissue constructs with applications and insights in cerebral organoids. Tissue Engineering Part C: Methods 22(3):221–249
Montel F, Delarue M, Elgeti J, Vignjevic D, Cappello G, Prost J (2012) Isotropic stress reduces cell proliferation in tumor spheroids. New Journal of Physics 14(5):055008
Nardi AC, Ferreira U, Claro JA, Stopiglia GM, Netto Jr NR (2004) Effects of high-energy shock wave on organs adjacent to the kidney in the growing rat. International braz j urol 30:142–147

Nataf F (2013) Absorbing boundary conditions and perfectly matched layers in wave propagation problems

Ngwa M, Agyingi E (2012) Effect of an external medium on tumor growth-induced stress. IAENG International Journal of Applied Mathematics 42(4):229–236

Nicolai H, Steinbach P, Knuechel-Clarke R, Grimm D, Roessler W, Wieland WF, Hofstaedter F (1994) Proliferation of tumor spheroids after shock-wave treatment. Journal of cancer research and clinical oncology 120:439–441

Ogden JA, Tóth-Kischkat A, Schultheiss R (2001) Principles of shock wave therapy. Clinical Orthopaedics and Related Research (1976-2007) 387:8–17

Oosterhof G, Smiths G, deRuyter J, Schalken J, Debruyne F (1990a) Effects of high-energy shock waves combined with biological response modifiers or adriamycin on a human kidney cancer xenograft. Urological Research 18:419–424

Oosterhof G, Cornel E, Smits G, Debruyne F, Schalken J (1996) The influence of high-energy shock waves on the development of metastases. Ultrasound in medicine & biology 22(3):339–344

Oosterhof GO, Smits GA, de Ruyter AE, Schalken JA, Debruyne FM (1990b) In vivo effects of high energy shock waves on urological tumors: an evaluation of treatment modalities. The Journal of urology 144(3):785–789

Palm MM, Elemans M, Beltman JB (2018) Heritable tumor cell division rate heterogeneity induces clonal dominance. PLoS Computational Biology 14(2):e1005954

Pillay S, Byrne HM, Maini PK (2018) The impact of exclusion processes on angiogenesis models. Journal of Mathematical Biology 77:1721–1759

Randall C (1988) Absorbing boundary condition for the elastic wave equation. Geophysics 53(5):611–624

Ribba B, Boetsch C, Nayak T, Grimm HP, Charo J, Evers S, Klein C, Tessier J, Charoin JE, Phipps A, et al. (2018) Prediction of the optimal dosing regimen using a mathematical model of tumor uptake for immunocytokine-based cancer immunotherapy. Clinical Cancer Research 24(14):3325–3333

Roerdink R, Dietvorst M, Van der Zwaard B, Van der Worp H, Zwerver J (2017) Complications of extracorporeal shockwave therapy in plantar fasciitis: Systematic review. International Journal of Surgery 46:133–145

Roose T, Netti PA, Munn LL, Boucher Y, Jain RK (2003) Solid stress generated by spheroid growth estimated using a linear poroelasticity model. Microvascular research 66(3):204–212

Roose T, Chapman SJ, Maini PK (2007) Mathematical models of avascular tumor growth. SIAM review 49(2):179–208

Russo P, Stephenson RA, Mies C, Huryk R, Heston WD, Melamed MR, Fair WR (1986) High energy shock waves suppress tumor growth in vitro and in vivo. The Journal of urology 135(3):626–628

Sansone V, Frairia R, Brañes M, Romeo P, Catalano MG, Applefield RC (2018) Current applications and future prospects of extracorporeal shockwave therapy. Shockwave Medicine 6:140–157

Serpe L, Canaparo R, Berta L, Bargoni A, Zara GP, Frairia R (2011) High energy shock waves and 5-aminolevulinic for sonodynamic therapy: effects in a syngeneic model of colon cancer. Technology in cancer research & treatment 10(1):85–93

Shrivastava S, Kailash (2005) Shock wave treatment in medicine. Journal of biosciences 30:269–275

Smits G, Oosterhof G, de Ruyter A, Schalken J, Debruyne F (1991) Antitumor effects of high-energy shock waves are potentiated by doxorubicin and biological response modifiers. In: Investigative Urology 4, Springer, pp 228–237

Steinhauser M (2016) On the destruction of cancer cells using laser-induced shock-waves: a review on experiments and multiscale computer simulations. Radiol Open J 1(2):60–75

Stylianopoulos T (2017) The solid mechanics of cancer and strategies for improved therapy. Journal of biomechanical engineering 139(2):021004

Stylianopoulos T, Martin JD, Chauhan VP, Jain SR, Diop-Frimpong B, Bardeesy N, Smith

BL, Ferrone CR, Hornicek FJ, Boucher Y, et al. (2012) Causes, consequences, and remedies for growth-induced solid stress in murine and human tumors. Proceedings of the National Academy of Sciences 109(38):15101–15108

Stylianopoulos T, Martin JD, Snuderl M, Mpekris F, Jain SR, Jain RK (2013) Coevolution of solid stress and interstitial fluid pressure in tumors during progression: implications for vascular collapse. Cancer research 73(13):3833–3841

Tabassum S, Rosli NB, Binti Mazalan MSA (2019) Mathematical modeling of cancer growth process: a review. In: Journal of Physics: Conference Series, IOP Publishing, vol 1366, p 012018

Tago J, Cruz-Atienza V, Chaljub E, Brossier R, Coutant O, Garambois S, Prieux V, Operto S, Mercerat D, Virieux J, et al. (2012) Modelling seismic wave propagation for geophysical imaging. In: Seismic waves-research and analysis, IntechOpen

Tanguay M (2004) Computation of bubbly cavitating flow in shock wave lithotripsy. California Institute of Technology

Unnikrishnan G, Unnikrishnan V, Reddy J, Lim C (2010) Review on the constitutive models of tumor tissue for computational analysis

Valdes-Ravelo F, Ramirez-Torres A, Rodriguez-Ramos R, Bravo-Castillero J, Guinovart-Diaz R, Merodio J, Penta R, Conci A, Sabina FJ, Garcia-Reimbert C (2018) Mathematical modeling of the interplay between stress and anisotropic growth of avascular tumors. Journal of Mechanics in Medicine and Biology 18(01):1850006

Voutouri C, Mpekris F, Papageorgis P, Odysseos AD, Stylianopoulos T (2014) Role of constitutive behavior and tumor-host mechanical interactions in the state of stress and growth of solid tumors. PloS one 9(8):e104717

Watanabe Y, Dahlman EL, Leder KZ, Hui SK (2016) A mathematical model of tumor growth and its response to single irradiation. Theoretical Biology and Medical Modelling 13:1–20

Wong AD, Searson PC (2017) Mitosis-mediated intravasation in a tissue-engineered tumor–microvessel platform. Cancer research 77(22):6453–6461

Wörle K, Steinbach P, Hofstädter F (1994) The combined effects of high-energy shock waves and cytostatic drugs or cytokines on human bladder cancer cells. British journal of cancer 69(1):58–65

Yin A, Moes DJA, van Hasselt JG, Swen JJ, Guchelaar HJ (2019) A review of mathematical models for tumor dynamics and treatment resistance evolution of solid tumors. CPT: pharmacometrics & systems pharmacology 8(10):720–737

Appendix A. Non-dimensionalization of the HESW therapy equations

To solve the coupled model, the quantities appearing in the equations governing the external medium must be non-dimensional, as in the case equations (3)-(7), corresponding to growing tumor model.

Using asterisks to identify the dimensionless variables

$$x_i^* = \frac{x_i}{L}, \quad t^* = \frac{t}{T}, \quad u_i^* = \frac{u_i^*}{L}, \quad U_i^* = \frac{U_i}{TL}, \quad w_{ij}^* = w_{ij}E, \quad \gamma_i^* = \gamma_i T, \tag{A1}$$

$$F^* = \frac{F}{E}, \quad s_i^* = Ls_i, \quad \rho^* = \frac{L^2}{ET^2}\rho, \tag{A2}$$

where the constants L, T and E has the physical magnitudes

$$L = [L], \quad T = [T], \quad E = \frac{[M]}{[L][T]^2},$$

with $[L]$, $[T]$ and $[M]$ representing *Longitude*, *Time* and *Mass*, respectively. Therefore, the new variables (Eq. (A1)-(A2)) are non-dimensional. Replacing the original variables of the system (14)-(16) with the expressions from (A1)-(A2), and removing the asterisks for simplicity, we obtain the exact same expression of system (14)-(16),with the only difference of being dimensionless.

Although the mathematical expression of the system (14)-(16) remains the same, the transformation of non-dimensionalization is critical when turning back to the original physical quantities of the system solution.

Appendix B. Spatial specifications of the combined model

Now we are going to describe the spatial location and specifications of the objects in Fig. 1 used in the simulations.

The domain is a cube of dimensions $8 \times 8 \times 8$, centred at the origin, with sides orthogonal to the axes. The tumor is centred at zero and begins with R_0 as initial radius. The source term is positioned at $(x_0, y_0, z_0) = (3, 0, 0)$, its zero for all points outside the ball centered at $(3, 0, 0)$ with radius 0.2, and inside the ball, its time variation term (see Fig. 2), which is multiplied, for spatial energy decay, by the factor $e^{\frac{\|\boldsymbol{x}\|}{0.2-\|\boldsymbol{x}\|}}$. The device to generate de shock waves (see Fig. 1) is positioned on the right of the domain and oriented toward the tumor been symmetric in relation the axis x. We define the device height as 1.2 (beginning in $x = 3.6$ and ending in $x = 2.4$), and its shape is defined so the focus where the waves are accumulated is at center of the tumor, $(0, 0, 0)$. The ellipse with focus at the source generation point and at the centere of the tumor was defined with a semi-major axis length of 2 and a linear eccentricity of 1.5.

Appendix C. Datasets for tumor models based in continuum mechanics

[1]We converted the original measure $(mol/(cell \cdot s))$ on the physical units $cm^3/(Kg \cdot s)$, using that

$$mol(O_2) = N_A{\cdot}2{\cdot}16{\cdot}u{\cdot}\frac{1}{1.429g/L} = 6.02214076{\cdot}10^{23}{\cdot}32{\cdot}1.6605390666{\cdot}10^{-27}Kg{\cdot}\frac{10^6cm^3/Kg}{1.249} = 0.256204963883{\cdot}10^5cm^3.$$

Substituting the cell density of cancer cells from Bryan et al. [2014] results

$$\frac{mol(O_2)}{cell} = \frac{0.256204963883 \cdot 10^5cm^3}{0.1 \cdot 10^{-11}Kg} = 0.256204963883 \cdot 10^{17}cm^3/Kg$$

[2]We repeat the same calculation of the above footnote, but using instead the density of the normal cell from Bryan et al. [2014]. Thus,

$$\frac{mol(O_2)}{cell} = \frac{0.256204963883 \cdot 10^5cm^3}{0.32 \cdot 10^{-11}Kg} = 0.800640512 \cdot 10^{16}cm^3/Kg.$$

Model parameters				
Parameter	Description	Value	Material	Reference
D_c	diffusion coefficient	$(1 \cdot 10^{-6}, 2.5 \cdot 10^{-5})\ cm^2/s$	soft tissue and hydrogel	McMurtrey [2016]
		$(1.2, 1.97) \cdot 10^{-5}\ cm^2/s$	DS-Cacinosarcoma	Grote et al. [1977]
A_c/ρ	nutrient consumption	$(0.729)\ \ (0.609, 0.889)\ cm^3/(Kg \cdot s)$	DLD1 human colorectal cancer	Grimes et al. [2014]
		$(3.7 \cdot 10^{-18}, 5.5 \cdot 10^{-15})\ mol/(cell \cdot s)$	varius cancer cell types	McMurtrey [2016]
		$(9.5 \cdot 10^{-2}, 1.4 \cdot 10^{2})\ cm^3/(Kg \cdot s)\ (1)$		
		$(8.3 \cdot 10^{-19}, 10^{-15})\ mol/(cell \cdot s)$	normal cells of different tissues	
		$(6.6 \cdot 10^{-3}, 8)\ cm^3/(Kg \cdot s)\ (2)$		
		$\sim 1\ cm^3/(Kg \cdot s)\ (3)$	(author assumption of typical values)	Ambrosi and Mollica [2004]
ρ	cell density	$(1.05, 1.07) \cdot 10^{-3}\ Kg/cm^3$	L1210 mouse lymphocytic leukemia	Bryan et al. [2014]
		$(1.038, 1.064) \cdot 10^{-3} Kg/cm^3$	normal human lung tissue	
–	cell volume	$(0.9)\ (0.55, 1.65) \cdot 10^{-9} cm^3$	L1210 mouse lymphocytic leukemia	
		$(2.6)\ (1.4, 7) \cdot 10^{-9} cm^3$	normal human lung tissue	
–	cell weight	$(1)(0.65, 2.95) 10^{-12} Kg$	L1210 mouse lymphocytic leukemia	
		$(3.2)(1.5, 7.6) 10^{-12} Kg$	normal human lung tissue	
α	rate of cell proliferation	$4.17 \cdot 10^{-2}/h$	K562 human leukemia stem cells	Palm et al. [2018]
		$5.26 \cdot 10^{-2}/h$	K562 human leukemia differentiated cells	
		$(0.903 - 1.87) \cdot 10^{-2}/h$	MDA-MP-231 human breast adenocarcinoma	Wong and Searson [2017]
		$(1.736)(1.1574, 2.3148) \cdot 10^{-2}/h$	breast cancer cell lines	Hafner et al. [2016]
ρ_g	density of agarose gel	$1.04 \cdot 10^{-3}\ Kg/cm^3$	-	Albro et al. [2008]

Table C1. Parameters values required for the tumor model in our study, obtained from experimental data reported in the literature.

[3]Calculated dividing its consumption rate by the density $10^{-3} cm^3/Kg$. Assuming that the consumption term is proportional to the nutrient concentration.

Elastic parameters			
Type of tumor	Bulk modulus κ	Shear modulus μ	Reference
epithelial breast MCaIV, 4T1, E0771	6.7 kPa	5 kPa	Stylianopoulos et al. [2012]
epithelial colon LS147T	4 kPa	3 kPa	
mesenchymal melanoma MU89, B16F10	2.5 kPa	1.9 kPa	
mesenchymal glioma U89	26.7 kPa	20 kPa	
breast MCF10CA1a	8.6 kPa	6.5 kPa	Voutouri et al. [2014]
colon SW620	8.1 kPa	6.1 kPa	
human sarcoma HSTS26T	40 kPa	30 kPa	Roose et al. [2003]
human glioblastoma U87	26.7 kPa	20 kPa	
human colon carcinoma LS174T	4 kPa	3 kPa	
mouse mamary carcinoma McaIV	6.7 kPa	5 kPa	
0.5% type VII agarose gel	0.12 kPa	0.1 kPa	
1% type VII agarose gel	0.33 kPa	0.15 kPa	

Table C2. Parameters essential for mathematical models based on continuum mechanics: the bulk and shear moduli of various tumor cell lines, and agarose gel utilized in *in vitro* experiments.

Tumor growth examples						
Tumor cell line	*Vivo*/*Vitro*	Animal	Treatment	Quimio	HESW	Reference
hepatoma MH134	*in vivo*	mouse	control, HESW, quimio, HESW+Quimio	1mg/kg cisplatin (CDDP) injected 6h after HESW	2000 shots, with 10 shost/s, and $9 \cdot 10^7\ Pa$ peak pressure	Maruyama et al. [1995b]
bladder cancer MBT-2	*in vivo* / *in vitro*	mouse	control, HESW, quimio, HESW+Quimio	9mg/kg cisplatin (DDP) injected before, during, or after HESW	200, 500, 600, 1000 shots, with 100 shost/min, peak preasure is missing, we assume it is $10^8\ Pa$	Lee et al. [1990]
human renal adenocarcinoma Nu-1	*in vivo*	mouse	control, HESW, $\text{quimio}_{1,2,3}$, $\text{quimio}_{1,2,3}$+HESW	5 ng/kg IFN alpha 500 ng/g TNF alpha Adryamicin 5mg/kg	800 shots with 2, 3, 4 sesions, with 80 shost/min, $5 \cdot 10^7\ Pa$ peak pressure	Oosterhof et al. [1990a]
human renal adenocarcinoma Nu-1, rat prostate cancer R3327 PAT-2, rat renal kidney tumor, human renal adenocarcinoma NC-65	*in vitro* / *in vivo*	mouse	control, HESW, $\text{quimio}_{1,2}$, $\text{quimio}_{1,2}$+HESW	5 mg/kg Adriamycin 0.25 mg/kg Vinblastine	800, 1500, 2000 shots in several sesions, with 80 shost/min, $5 \cdot 10^7\ Pa$ peak pressure	Oosterhof et al. [1990b]
fibrosarcoma SSK2	*in vitro*	mouse	control, HESW, $\text{quimio}_{1,2}$, $\text{quimio}_{1,2}$+HESW	25 mg/Kg of gelonin, and $2.5mg/Kg$ of saporing	500 shots in three sessions, with 100 shots/min, and $8.3 \cdot 10^7\ Pa$ peak pressure	Delius and Adams [1999]
mouse hepatocellular carcinoma MH134	*in vivo* / *in vitro*	mouse	control, HESW, quimio, quimio+HESW	$(1-40)mg/ml$ gallium -porphyrim complex ATX-70	250, 500, 1000, and 2000 shots, with 600 and 1200 shots/min, and $5 \cdot 10^7\ Pa$, and $9 \cdot 10^7\ Pa$ of peak pressure	Maruyama et al. [1995a]
Human colorectal cancer HT-29	*in vitro*	-	control, HESW, quimio, quimio+HESW	$50\mu g/ml$ 5-aminolevulinic acid (ALA)	500 and 1000 shots, with 240 shots/min, and $3.1 \cdot 10^7\ Pa$, and $9 \cdot 10^7\ Pa$ of peak pressure	Canaparo et al. [2006]
amelanotic hamster melanoma A-Mel-3	*in vivo*	hamster	control, HESW, surgery	-	200 shots with 138 shots/min, peak pressure is missing, we assume it is $5 \cdot 10^7\ Pa$	Gamarra et al. [1993a]
bladder cancer VX2	*in vivo*	rabbit	control, HESW	-	7000 shots, with 5 shots/s and $1.3 \cdot 10^8\ Pa$ peak preasure	Hoshi et al. [1991]
bladder cancer RT112 prostate PCA	*in vitro*	-	control, HESW	-	200 and 800 shots with 1 shots/s, peak pressure is missing, we assume it is $10^8\ Pa$	Nicolai et al. [1994]
rat prostatic carcinoma R3327AT-3, human melanoma SK-Mel-28	*in vivo* / *in vitro*	mouse	control, HESW	-	800 and 1500 shots, with 100 shots/s peak pressure is missing, we assume $10^8\ Pa$	Russo et al. [1986]
human colon cancer LS174T	*in vitro*	-	-	-	-	Helmlinger et al. [1997]
mesenchymal melanoma MU89	*in vivo*	mouse	-	-	-	Roose et al. [2003]
breast cancer MCF10CA1a	*in vivo*	mouse	-	-	-	Voutouri et al. [2014]
adenocarcinoma CT-26	*in vivo*	mouse	-	-	-	Guba et al. [2002]

Table C3. References of growing tumor experiments, covering both *in vitro* and *in vitro* scenarios, involving treatments such as HESW therapy and chemotherapy. Details of the main features of the experiments are summarized.

Chapter 5

Conclusions

The primary objective of this thesis is to explore the capabilities and limitations of explicit exponential integrators in addressing linear wave equations with ABC. To achieve this, we have studied one of the most well-known exponential integrators, the Chebyshev polynomials. More specifically, its generalisation, the Faber polynomials, to overcome the limitations encountered when considering ABC.

In the second chapter, we addapted an explicit exponential integrator based on Faber polynomials, described in Bergamaschi, Caliari, *et al.* (2003), to solve the wave propagation equations. Using the method state-of-the-art as starting point, we explored its key features for optimal application into our specific equations. First, analyzing how to implement an adaptative scheme into Faber method, we improved a previous reported error bound of its approximation. Moreover, through numerical examples, we illustrated that the ellipse with minimum capacity enclosing the eigenvalues of the matrix operator is not always the optimal conic for ensuring the fastest convergence of Faber series, different to what was suggested in Bergamaschi, Caliari, *et al.* (2003). We also highlighted the importance of a good estimation of the convex envelope of the operator spectrum, for the convergence of the method. In this direction, we proposed a strategy to estimate the convex envelope by computing the spectrum in operators of a much smaller size, significantly reducing the required computations. Additionally, we examined the dispersion and dissipation properties of Faber polynomials using a Von Neumann analysis, and studied convergence and computational efficiency through various numerical experiments. We observed that increasing the order of the approximation implies a larger CFL number, and solutions calculated for larger time steps maintain high accuracy. From the computational efficiency results, we also concluded that, at least for Faber polynomials applied to seismic waves, higher polynomial degrees are computationally more efficient than lower-order polynomials.

Next, to determine the real potential of Faber polynomials for practical applications, we compared it with other explicit exponential integrators and classical numerical methods. This is the subject of Chapter 3, where numerical tests were conducted, using four distinct velocity fields, including both realistic and sharp interface fields. We also, studied the main numerical features: stability, dispersion, convergence, computational cost, and memory

consumption. Remarkably, our results proved to be consistent and robust across both types of errors and all four numerical experiments. Furthermore, the Krylov method had the largest time step size in all tests, and for all high-order methods, higher approximation degrees allowed for larger time steps, significantly impacting the number of saved vectors needed for solving the inverse problem. Nevertheless, in terms of computational efficiency, the Leap-frog method proved to be the most efficient.

On the other hand, the need for computing efficient solutions to wave propagation equations is not exclusive to seismic imaging problems. To this end, we developed a coupled mathematical model of tumor growth based on continuum mechanics, that incorporates a mathematical formulation to replicate shock wave therapy, proposing a different direction for mechanical models of tumor growth (see Chapter 4). In this therapy, the high frequency of wave applications and the specific shape of the wave signal induces the use of very small time steps, significantly inreasing the cost to compute the solution. With this model, we explored various possible outcomes of tumor growth by varying HESW therapy parameters. And the obtained numerical solutions are qualitatively similar to experiments conducted in the works of Russo *et al.*, 1986; Wörle *et al.*, 1994; Hoshi *et al.*, 1991, supporting the validity of these preliminary results. The mathematical model is intended to be a prototype that allows a proof of concept towards reproducibility of HESW treatment.

Through this research, we studied the properties of exponential integrators when applied to solve linear wave propagation equations with absorbing boundary conditions. This research aims to fill a gap in the scientific literature where several works mention the capabilities of exponential integrators to solve this kind of problem (Kole, 2003; Hochbruck and Ostermann, 2010; Moler and Van Loan, 2003; Mossaiby *et al.*, 2015), but none analyze in detail their performance and real potential in this kind of problem. In conclusion, we observed that increasing the order of the approximations not only serves to reduce the approximation error but also increases the Courant number in the CFL condition, allowing larger time steps while maintaining good accuracy. This could lead to other strategies to solve the inverse problem in seismic imaging, and it may be useful in other applications.

Regarding to the simulation of HESW therapy in a growing tumor. It represents a novel application of the wave propagation equations, incorporating the mechanical effects of therapy on soft tissue, where efficient algorithms to compute the wave equations while accurately representing shock waves are needed.

This research should not be seen as the definitive answer to the use of explicit exponential integrators in solving linear wave equations with ABC, but rather as a first approach to the subject. The methodology used can be refined, leading to more comprehensive and accurate results. With this in mind, we aim to highlight the main limitations of this study and suggest possible ways to overcome them.

Future work

1. As illustrated in Section 2.2.2 of Chapter 2, it is unclear whether the optimal conic shape is indeed the ellipse of minimum capacity, as suggested by Bergamaschi,

Caliari, *et al.*, 2003. Consequently, a study to determine the optimal conic shape, aiming to enhance accuracy and broaden the convergence region, is necessary. Achieving results in this direction would significantly enhance the efficiency of the Faber method.

2. From the work of Moler and Van Loan (2003), it is clear that algorithms approximating the exponential of non-normal matrices must exercise extreme caution when dealing with the "hump" phenomenon of the matrix exponential norm. This feature indicates that an adaptive time-step strategy is the most suitable approach for high-order exponential integrators. Such a strategy has already been implemented for exponential integrators like the Krylov subspace method (Gaudreault *et al.*, 2021), the Leja interpolation points scheme (Pranab J Deka *et al.*, 2023), and Padé rational approximations (Higham, 2005). However, as mentioned in Pranab Jyoti Deka and Einkemmer (2022), and supported by the works of Gaudreault *et al.* (2021), Pranab J Deka *et al.* (2023), and Higham (2005), implementing adaptive steps requires a precise estimation of the approximation error. Unfortunately, as discussed in Section 2.2.1 of Chapter 2, estimating the Faber series error for non-normal matrix operators remains an open problem.

   Nevertheless, if a theoretical error estimation is not feasible, it does not negate the possibility of an empirical estimate. We could exhaustively apply an adaptive time-step through trial and error, seeking correlations with quantities used in previous research on exponential integrators to bound the approximation error. This brute force approach will not only tell us about the feasibility of an adaptive time-step algorithm for Faber polynomials, but also hints at a potential relationship between the optimal time-step and other metrics, such as the matrix norm. Moreover, it could be used in assessing whether the adaptive time-step algorithms reported for other exponential integrators are optimal and to suggest paths for improvement.

3. We can also expand the repertoire of methods for comparison, providing a broader perspective on the results achieved with exponential integrators.

4. In the numerical experiments, in order to consider the source term, we used an approximation in Taylor series of the signal, and computed the matrix exponential in a sligthly large matrix. However, this is not the only approach for incorporating the source term with the exponential integrator. As demonstrated in Kole (2003), we can expand the source function in the basis used by the exponential integrator and simultaneously computing the two matrix exponentials. This approach could reveal new features of the methods.

5. In relation to the mathematical model of applying HESW therapy to a growing tumor, we could gradually expand the model to simulate other action mechanisms reported in the literature for the therapy. In addition, to enhance the accuracy of the numerical experiments and formulate more reliable complex processes, we could employ better geometries than a square finite difference grid to precisely represent the shape of the tumor and the device generating the HESW.

Bibliography

[Assi and Cobbold 2017] Hisham Assi and Richard S Cobbold. "Compact second-order time-domain perfectly matched layer formulation for elastic wave propagation in two dimensions". In: *Mathematics and Mechanics of Solids* 22.1 (2017), pp. 20–37 (cit. on p. 4).

[Bergamaschi, Caliari, *et al.* 2003] Luca Bergamaschi, Marco Caliari, and Marco Vianello. "Efficient approximation of the exponential operator for discrete 2d advection–diffusion problems". In: *Numerical linear algebra with applications* 10.3 (2003), pp. 271–289 (cit. on pp. 3, 127, 128).

[Bergamaschi and Vianello 2000] Luca Bergamaschi and Marco Vianello. "Efficient computation of the exponential operator for large, sparse, symmetric matrices". In: *Numerical linear algebra with applications* 7.1 (2000), pp. 27–45 (cit. on pp. 3, 4).

[Pranab J Deka *et al.* 2023] Pranab J Deka, Lukas Einkemmer, and Mayya Tokman. "Lexint: package for exponential integrators employing leja interpolation". In: *SoftwareX* 21 (2023), p. 101302 (cit. on pp. 2, 129).

[Pranab Jyoti Deka and Einkemmer 2022] Pranab Jyoti Deka and Lukas Einkemmer. "Efficient adaptive step size control for exponential integrators". In: *Computers & Mathematics with Applications* 123 (2022), pp. 59–74 (cit. on p. 129).

[Eiken 2019] Ola Eiken. "Twenty years of monitoring co2 injection". In: *Geophysics and geosequestration* (2019), p. 209 (cit. on p. 1).

[Gamarra *et al.* 1993] Fernando Gamarra, Fritz Spelsberg, Marc Dellian, and Alwin E Goetz. "Complete local tumor remission after therapy with extra-corporeally applied high-energy shock waves (hesw)". In: *International journal of cancer* 55.1 (1993), pp. 153–156 (cit. on p. 4).

[Gaudreault *et al.* 2021] Stephane Gaudreault, Greg Rainwater, and Mayya Tokman. "Kiops: a fast adaptive krylov subspace solver for exponential integrators (vol 372, pg 236, 2018)". In: *JOURNAL OF COMPUTATIONAL PHYSICS* 441 (2021) (cit. on p. 129).

[Graimann *et al.* 2010] Bernhard Graimann, Brendan Allison, and Gert Pfurtscheller. "Brain–computer interfaces: a gentle introduction". In: *Brain-computer interfaces: Revolutionizing human-computer interaction* (2010), pp. 1–27 (cit. on p. 1).

[Hendry 2007] Martin Hendry. "An introduction to general relativity, gravitational waves and detection principles". In: *Second VESF School on Gravitational Waves, Cascina, Italy, May 28th–June 1st* (2007) (cit. on p. 1).

[Higham 2005] Nicholas J Higham. "The scaling and squaring method for the matrix exponential revisited". In: *SIAM Journal on Matrix Analysis and Applications* 26.4 (2005), pp. 1179–1193 (cit. on p. 129).

[Hochbruck and Ostermann 2010] Marlis Hochbruck and Alexander Ostermann. "Exponential integrators". In: *Acta Numerica* 19 (2010), pp. 209–286 (cit. on pp. 3, 128).

[Hoshi *et al.* 1991] Senji Hoshi *et al.* "High energy underwater shock wave treatment on implanted urinary bladder cancer in rabbits". In: *The Journal of urology* 146.2 (1991), pp. 439–443 (cit. on pp. 4, 128).

[Huenges *et al.* 2013] Ernst Huenges *et al.* "Geothermal energy systems: research perspective for domestic energy provision". In: *Environmental Earth Sciences* 70 (2013), pp. 3927–3933 (cit. on p. 1).

[Ikelle and Amundsen 2018] Luc T Ikelle and Lasse Amundsen. *Introduction to petroleum seismology*. Society of Exploration Geophysicists, 2018 (cit. on p. 1).

[Jing *et al.* 2019] Hao Jing, Yushu Chen, Jian Wang, and Wei Xue. "A highly efficient time-space-domain optimized method with lax-wendroff type time discretization for the scalar wave equation". In: *Journal of Computational Physics* 393 (2019), pp. 1–28 (cit. on p. 2).

[Kole 2003] JS Kole. "Solving seismic wave propagation in elastic media using the matrix exponential approach". In: *Wave Motion* 38.4 (2003), pp. 279–293 (cit. on pp. 3, 99, 128, 129).

[Kosloff *et al.* 1989] Dan Kosloff, ANIBAL QUEIROZ FILHO, EKKEHART TESSMER, and ALFRED BEHLE. "Numerical solution of the acoustic and elastic wave equations by a new rapid expansion method 1". In: *Geophysical prospecting* 37.4 (1989), pp. 383–394 (cit. on p. 3).

[Loffeld and Tokman 2013] John Loffeld and Mayya Tokman. "Comparative performance of exponential, implicit, and explicit integrators for stiff systems of odes". In: *Journal of Computational and Applied Mathematics* 241 (2013), pp. 45–67 (cit. on p. 3).

[López-Marin *et al.* 2018] Luz M López-Marin, Ana Leonor Rivera, Francisco Fernández, and Achim M Loske. "Shock wave-induced permeabilization of mammalian cells". In: *Physics of Life Reviews* 26 (2018), pp. 1–38 (cit. on p. 4).

[Lowrie and Fichtner 2020] William Lowrie and Andreas Fichtner. *Fundamentals of geophysics*. Cambridge university press, 2020 (cit. on p. 1).

[Martinez *et al.* 2009] Angeles Martinez, Luca Bergamaschi, Marco Caliari, and Marco Vianello. "A massively parallel exponential integrator for advection-diffusion models". In: *Journal of Computational and Applied Mathematics* 231.1 (2009), pp. 82–91 (cit. on p. 2).

[Maruyama *et al.* 1995] Michihiro Maruyama *et al.* "The effect of high-energy shock wave therapy combined with cisplatin on mouse hepatoma". In: *Surgery today* 25 (1995), pp. 987–988 (cit. on p. 4).

[Moler and Van Loan 2003] Cleve Moler and Charles Van Loan. "Nineteen dubious ways to compute the exponential of a matrix, twenty-five years later". In: *SIAM review* 45.1 (2003), pp. 3–49 (cit. on pp. 128, 129).

[Mossaiby *et al.* 2015] F. Mossaiby, M Ghaderian, and R. Rossi. "Implementation of a generalized exponential basis functions method for linear and non-linear problems". In: *International Journal for Numerical Methods in Engineering* 105 (2015), pp. 221–240 (cit. on p. 128).

[Niederleithinger *et al.* 2016] Ernst Niederleithinger, Odile Abraham, and Mike Mooney. *Geophysical methods in civil engineering: overview and new concepts*. Bundesanstalt für Materialforschung und-prüfung (BAM), 2016 (cit. on p. 1).

[Oosterhof *et al.* 1990] GON Oosterhof, GAHJ Smiths, JE deRuyter, JA Schalken, and FMJ Debruyne. "Effects of high-energy shock waves combined with biological response modifiers or adriamycin on a human kidney cancer xenograft". In: *Urological Research* 18 (1990), pp. 419–424 (cit. on p. 4).

[Peixoto and Schreiber 2019] Pedro S Peixoto and Martin Schreiber. "Semi-lagrangian exponential integration with application to the rotating shallow water equations". In: *SIAM Journal on Scientific Computing* 41.5 (2019), B903–B928 (cit. on p. 3).

[Pototschnig *et al.* 2009] Martin Pototschnig, Jens Niegemann, Lasha Tkeshelashvili, and Kurt Busch. "Time-domain simulations of the nonlinear maxwell equations using operator-exponential methods". In: *IEEE Transactions on Antennas and Propagation* 57.2 (2009), pp. 475–483 (cit. on p. 3).

[Radi and Rasmussen 2013] Hafez A Radi and John O Rasmussen. "Principles of physics". In: *Springer, Berlin Heidelberg, New Delhi, DOI* 10 (2013), pp. 978–3 (cit. on p. 1).

[Ravelo F 2023] Schreiber M Ravelo F Peixoto P. "An explicit exponential integrator based on faber polynomials and its application to seismic wave modeling". In: *Journal of Scientific Computing* -.- (2023), (accepted) (cit. on p. 9).

[Russo *et al.* 1986] Paul Russo *et al.* "High energy shock waves suppress tumor growth in vitro and in vivo". In: *The Journal of urology* 135.3 (1986), pp. 626–628 (cit. on pp. 4, 128).

[Schreiber *et al.* 2019] Martin Schreiber, Nathanaël Schaeffer, and Richard Loft. "Exponential integrators with parallel-in-time rational approximations for the shallow-water equations on the rotating sphere". In: *Parallel Computing* 85 (2019), pp. 56–65 (cit. on p. 3).

[Shrivastava and Kailash 2005] SK Shrivastava and Kailash. "Shock wave treatment in medicine". In: *Journal of biosciences* 30 (2005), pp. 269–275 (cit. on p. 4).

[Tal-Ezer *et al.* 1987] H Tal-Ezer, D Kosloff, and Z Koren. "An accurate scheme for seismic forward modelling". In: *Geophysical Prospecting* 35.5 (1987), pp. 479–490 (cit. on pp. 3, 99).

[Tessmer 2011] Ekkehart Tessmer. "Using the rapid expansion method for accurate time-stepping in modeling and reverse-time migration". In: *Geophysics* 76.4 (2011), S177–S185 (cit. on pp. 3, 99).

[Theis and Bonomi 2023] Daniela Theis and Ernesto Bonomi. "Seismic imaging of medical ultrasound data: towards in vivo applications". In: *Europhysics Letters* 142.5 (2023), p. 52001 (cit. on p. 1).

[Virieux *et al.* 2017] Jean Virieux *et al.* "An introduction to full waveform inversion". In: *Encyclopedia of exploration geophysics*. Society of Exploration Geophysicists, 2017, R1–1 (cit. on p. 1).

[Wilcox *et al.* 2010] Lucas C Wilcox, Georg Stadler, Carsten Burstedde, and Omar Ghattas. "A high-order discontinuous galerkin method for wave propagation through coupled elastic–acoustic media". In: *Journal of Computational Physics* 229.24 (2010), pp. 9373–9396 (cit. on p. 2).

[Woelz and Rabbel 2005] Susanne Woelz and Wolfgang Rabbel. "Seismic prospecting in archaeology: a 3d shear-wave study of the ancient harbour of miletus (turkey)". In: *Near Surface Geophysics* 3.4 (2005), pp. 245–257 (cit. on p. 1).

[Wörle *et al.* 1994] K Wörle, P Steinbach, and Ferdinand Hofstädter. "The combined effects of high-energy shock waves and cytostatic drugs or cytokines on human bladder cancer cells". In: *British journal of cancer* 69.1 (1994), pp. 58–65 (cit. on p. 128).

[Yomosa 1987] Sigeo Yomosa. "Solitary waves in large blood vessels". In: *Journal of the Physical society of Japan* 56.2 (1987), pp. 506–520 (cit. on p. 1).

[Zhang *et al.* 2014] Xiao Zhang, Dinghui Yang, and Guojie Song. "A nearly analytic exponential time difference method for solving 2d seismic wave equations". In: *Earthquake Science* 27.1 (2014), pp. 57–77 (cit. on p. 3).